**Dissertation submitted to the Combined
Faculties for the Natural Sciences and for
Mathematics of the Ruperto-Carola University of
Heidelberg, Germany, for the Degree of Doctor
of Natural Sciences**

presented by

Dipl.-Phys. Peter Franz

born in Dieburg, Germany

Oral Examination: February 16, 2005

The Isotopic Composition of Water Vapor in the Upper Troposphere/Lower Stratosphere Region: Modeling, Analysis and Sampling

Referees:

Prof. Dr. Ulrich Platt

P.D. Dr. Thomas Röckmann

Abstract

Die isotopische Zusammensetzung von Wasserdampf in der oberen Troposphäre/unteren Stratosphäre: Genaue Kenntnis über die isotopische Zusammensetzung von Wasserdampf in der Tropopausenregion und der Stratosphäre liefert wichtige Informationen zum Verständnis von atmosphärischem Transport und Photochemie. Diese Arbeit beschreibt zunächst anhand von Modellen, wodurch die isotopische Zusammensetzung des Wasserdampfes bestimmt wird. Dabei wird sowohl auf die stabilen Isotopologe HDO, $H_2^{17}O$ und $H_2^{18}O$, als auch auf das radioaktive Isotopolog HTO eingegangen. Danach wird ein Instrumentensatz vorgestellt, mit dem präzise Messungen der genannten Isotopologe möglich sind. Für die stabilen Isotopologe besteht der Instrumentensatz aus drei Geräten: einem Continuous-Flow System zur chemischen Umwandlung von H_2O in H_2 und O_2 zur anschliessenden massenspektrometrischen Analyse, einer Kalibriereinheit zur Herstellung Wasserdampfs mit bekannten Isotopenverhältnissen, und einer kryogenen Sammeleinheit zum Einsatz auf Flugzeugen und Ballons. Die dabei benötigten Probenmengen konnten auf eine Grössenordnung von $100 ng$ reduziert werden. Weiterhin wurden Experimente mit einer Sammeleinheit für tritierten Wasserdampf durchgeführt. Mit Hilfe der genannten Apparaturen wurden auf insgesamt 6 Flügen zwischen Neuseeland und der Antarktis Proben atmosphärischen Wasserdampfs genommen und analysiert.

The isotopic composition of water vapor in the upper troposphere/lower stratosphere: Exact knowledge about the isotopic composition of water vapor in the tropopause region and the stratosphere provides important information for the understanding of atmospheric transport and photochemistry. The presented thesis describes with the help of models the processes governing the isotopic composition of atmospheric water vapor. The stable isotopologues - HDO, $H_2^{17}O$ and $H_2^{18}O$ - and the radioactive isotopologue HTO are discussed. A complete analytical procedure has been developed for the purpose of precise measurements of the mentioned water isotopologues. For the stable isotopologues, it consists of three instruments: a continuous-flow system for the chemical decomposition of H_2O to H_2 and O_2 for subsequent mass-spectrometrical analysis, a calibration

unit for the production of water vapor with known isotopic composition, and a cryogenic sampling unit for operation aboard airplanes and balloons. The required sample amount could be reduced to about $100ng$. Further, experiments with a sampling unit for tritiated water vapor have been performed. With these apparatus, samples of atmospheric water vapor have been taken on 6 flights between New Zealand and Antarctica, and have later been analyzed in the laboratory.

I've been a wild scientist for many a year,
and I spent so much money on mass specs and gear.
But now I'm returning with samples in great store,
and I'll promise to play the wild scientist no more!

And it's no, nay, never... no nay never, no more,
that I'll do water vapor samples,
no nay never, no more!

a wee bit adapted, "The Wild Rover"

Contents

Chapter 1

Introduction

Water in its three phases solid, liquid and gaseous, plays an important role in the energy budget of the earth and in atmospheric chemistry. It strongly effects the albedo by reflecting solar energy from ice and snow surfaces in the polar regions, from the surface of the oceans and from the surface of cloud particles. It is the most important greenhouse gas, absorbing infrared radiation in the troposphere and thus warming the planet. Of the total $\approx 33K$ natural greenhouse effect, water vapor is responsible for $\approx 20.6K$ of warming!

In the tropics, warm air parcels with a high water vapor content rise and cool by adiabatic expansion. In the condensation process, the water vapor releases its latent heat. Thus these air parcels remain warmer and thus less dense than the surrounding air, leading to rapid ascent. This enhances large-scale global circulation patterns like the Brewer-Dobson and the Hadley cells.

Alarming news appeared in the 1980s with the discovery of the Antarctic Ozone Hole, in which up to 70% of the total ozone column vanished in a matter of days. As ozone shields life on earth from UV radiation, much attention was drawn to this phenomenon. It was discovered that inside the polar vortex, where very deep temperatures of less than $190K$ are encountered, inactive chlorine compounds are transfered into active chlorine (Cl_2) by heterogeneous reactions on the surface of polar stratospheric cloud (PSC) particles. Upon arrival of solar light in Antarctic spring, these compounds are photolyzed to Cl, which immediately begins its catalytic ozone destruction cycle.

While most of the following efforts concentrated on how to reduce the atmospheric halogen burden, another problem showed up: Oltmans et al. [2000] and Rosenlof et al. [2001] concluded from longtime measurements of stratospheric water vapor that its concentration might have risen from $\approx 4ppm$ in the 1950s to $\approx 6ppm$ at present. This substantial rise in vapor concentrations leads to global

warming and stratospheric cooling [Forster and Shine, 2002]. Stratospheric cooling and increased water vapor pressure leads to the increased occurrence of PSC particles and thus increased ozone destruction in the polar regions [Stenke and Grewe, 2004].

Up to date, the sources of this increase in stratospheric water vapor are not fully understood. Rosenlof et al. [2001] estimate that at most $1.1ppm$ of the additional water vapor stems from the anthropogenic increase in CH_4. While the CH_4 oxidation mechanism can not account for the whole amount of additional water vapor, a second possibility is the change in magnitude of circulation patterns that are responsible for the transport of water vapor into the stratosphere. Another process could be the increased amount of atmospheric SO_2, which could lead to more cloud condensation nuclei, smaller cloud droplets and thus less efficient sedimentation in the tropical tropopause layer [Notholt et al., 2004]. In the upper stratosphere, Röckmann et al. [2003] estimate that the increased chlorine, the reduced ozone column and the increased OH due to increased H_2O itself can explain up to 50% of additional conversion of CH_4 to H_2O.

Thus, despite the importance of water vapor for our climate, its stratospheric cycle is still poorly understood. It is known that isotope measurements can shine more light into this issue than concentration measurements alone. During phase changes and chemical reactions, water molecules that have one of their atoms substituted by a rare isotope have different vapor pressures and reaction rates. Therefore, each of these processes leaves a mark or "isotopic fingerprint" on the vapor. This gives additional constraints, as models not only have to explain the concentrations encountered but also the isotope composition of the water vapor.

This thesis deals with the development of a system for sampling and analysis of atmospheric water vapor in the upper troposphere and lower stratosphere, as well as modeling the photochemistry of water in the middle atmosphere.

Chapter 2 gives a brief summary of the physics and mathematics necessary to describe the four major isotopologues of water - the stable species H_2O, HDO, $H_2^{17}O$ and $H_2^{18}O$, and the minor radioactive species HTO.

Chapter 3 discusses the present understanding how water vapor enters the stratosphere in dehydration processes, and how it is transported in the largescale global circulation.

In chapter 4, a one-dimensional model is presented that includes the photochemistry of water vapor, methane and molecular hydrogen in the middle atmosphere. Both hydrogen and oxygen isotopes are included, and the sources and sinks of the most important species are described in detail. A simpler and more limited model is developed in order to describe the production, decay and transport of tritium in the stratosphere.

For the stable isotopologues HDO, $H_2^{17}O$ and $H_2^{18}O$, a continuous-flow system for isotope ratio mass spectrometry has been developed. This system is described in chapter 5. In order to use this system with sample containers for atmospheric water vapor, an airborne sampling unit and a calibration line have been built, which are explained in chapters 6 and 7, respectively. Parts of chapter 5 have been previously published [Franz and Röckmann, 2004].

Measurements of the radioactive tracer tritium was carried out using a system described by Franz [2002]. It makes use of molecular sieves as a trap for atmospheric water vapor. Due to its limited precision, it is only applicable to the analysis of HTO. This system has been improved further in order to collect more samples; details can be found in chapter 8.

The highlights of this thesis are the measurements of the isotopologues HTO, $H_2^{17}O$ and $H_2^{18}O$ at and above the tropopause height on six measurement flights in 2003 and 2004. The measurements of the oxygen isotopes are believed to be the most precise measurements up to date. Analysis of this data is found in chapter 9, followed by a short summary.

Chapter 2

Isotope Physics and Water Isotopologues

2.1 Properties of H_2O

The amount of water vapor in an air parcel is limited by the saturation vapor pressure E over liquid water (E_l, $T \geq 0C$) or ice (E_s, $T \leq 0C$, though conditions for supercooled liquid water can exist):[1]

$$
\begin{aligned}
E_l(T) &= 1.1749 \cdot 10^{11} Pa \cdot \exp\left(-\frac{43318 J/mol}{R \cdot T}\right) & (2.1) \\
E_s(T) &= 3.5927 \cdot 10^{12} Pa \cdot \exp\left(-\frac{51087 J/mol}{R \cdot T}\right) & (2.2)
\end{aligned}
$$

An important feature of water vapor is its high enthalpy of vaporization, $L_l = 43990 J/mol$ and $L_s = 51084 J/mol$ for liquid water and ice, respectively [Lide, 1996]. Due to this high enthalpy, water vapor is responsible for the redistribution of energy in the atmosphere via transport of latent heat.

The relative humidity is defined as the ratio of the actual vapor pressure e in the air parcel and the saturation vapor pressure E:

$$
f = e/E \cdot 100\% \qquad (2.3)
$$

---

[1] E_s fitted onto data from Hobbs [1974] and Lide [1996], E_l as in Zahn [1995] and references therein

The mixing ratio υ is defined as the ratio of the number of water molecules to all other molecules in gas phase of an air parcel, and can be approximated by the ratio of the actual vapor pressure e and the total pressure p:

$$\upsilon = \frac{N_{H_2O}}{N_{air}} \approx \frac{e}{p} \qquad (2.4)$$

υ is often expressed in ppm, where $1ppm = 10^{-6}$.

2.2 Isotopologues of H_2O and Measurement Standards

Both hydrogen and oxygen possess, besides their main isotope, stable and radioactive isotopes. These isotopes provide important information in geophysics, as distinct processes leave an isotopic "fingerprint" on the ratios encountered in a sample.

Of the radioactive species, oxygen isotopes are too short-lived ($\tau \leq 2min$ for all radioactive isotopes) to play an important role as tracers for atmospheric transport or chemistry. Hydrogen, on the other hand, possesses the isotope ^3H, denoted as *tritium (T)*. It has a sufficiently long half-life of $\tau_{1/2} = 12.33a$, so that it can provide insight into atmospheric transport phenomena.

Hydrogen also has the rare stable isotope ^2H, denoted as *deuterium (D)*. Oxygen possesses two rare stable isotopes, ^{17}O and ^{18}O (in models often denoted as P and Q). To enable comparison between laboratories, the abundance of these stable isotopes is measured versus a standard material. For water, this is *Vienna Standard Mean Ocean Water (VSMOW or SMOW)*. It has the absolute isotope ratios of

isotope	isotope ratio	reference
$^2H/^1H$	$(155.76 \pm 0.05) \cdot 10^{-6}$	Hagemann et al. [1970]
$^{17}O/^{16}O$	$(379.9 \pm 0.8) \cdot 10^{-6}$	Li et al. [1988b]
$^{18}O/^{16}O$	$(2005.20 \pm 0.45) \cdot 10^{-6}$	Baertschi [1976]

In principle, the absolute isotope ratio of the sample can be calculated from the signal of an analytical instrument. Due to uncertainties in the amplification of the instruments used, the errors in such absolute ratios are quite high. Therefore, a sample is measured versus a reference material with known isotope ratios (e.g. O_2 gas from a cylinder). The advantage of this method is that the signal

amplification factors of the analytical instrument cancel out, and high precisions are obtained. The isotopic composition of a sample is expressed as the deviation from a standard material (δ-*notation*):

$$\delta X = \left(\frac{^X R_{sample}}{^X R_{standard}} - 1 \right) \cdot 1000\text{‰} \tag{2.5}$$

where R denotes the ratio of the rare isotope to the more abundant isotope (e.g. $^{17}R = [^{17}O]/[^{16}O]$).

As the isotope ratio deviations from the standard material are usually quite small, the result is expressed in per mill (‰). To allow for a compact notation, all equations in this thesis expect δ-values to be entered correctly, i.e. $1\text{‰} = 0.001$, if not stated otherwise. This is in some contrast to many authors, who carry division by 1000 through their formulas.

With these rare isotopes at hand, different H_2O molecules can be constructed by replacing a main isotope by a rare isotope. In this fashion, the single substituted *isotopologues* HTO, HDO, $H_2^{17}O$ and $H_2^{18}O$ can be formed. Substituting more than one main by a rare isotope leads to isotopologues such as DDO, $HD^{17}O$ and so on. However, their abundances are too low to be measured in geophysical applications so far.

In some publications, especially optical measurements of water vapor, the ratio $[HDO]/[H_2O]$ is measured rather than $[D]/[H]$. As there are two hydrogen atoms in a water molecule, the expression for δD has to be changed into

$$\delta D = \left(\frac{[HDO]/(2 \cdot [H_2O])}{^2 R_{VSMOW}} - 1 \right) \cdot 1000\text{‰} \tag{2.6}$$

The natural abundance of tritium is so small that it more convenient to express to express the ratio

$$^T R = \frac{[T]}{[H]} = \frac{[HTO]}{2 \cdot [H_2O]} \tag{2.7}$$

in *tritium units (TU)*, where $1TU = 10^{-18}$.

Though the abundance of HTO is much smaller than the stable isotopes, the tritium amount present can be measured via radioactive decay, and the ratio HTO/H_2O can be calculated from the bulk mass of a water sample.

2.2.1   Isotope Mass Balance

When mixing substances from two different reservoirs (N_1, R_1, N_2, R_2), the resulting mixture ($N = N_1 + N_2$, R) must obey the relation

$$\frac{R \cdot N}{1 + R} = \frac{R_1 \cdot N_1}{1 + R_1} + \frac{R_2 \cdot N_2}{1 + R_2} \tag{2.8}$$

For ratios $R \ll 1$, this formula can be approximated by

$$R = f_1 \cdot R_1 + f_2 \cdot R_2 \tag{2.9}$$

where $f_1 = N_1/N$ and $f_2 = N_2/N$ are the fractions of the two different reservoirs. A similar approximation is valid for the δ-notation:

$$\delta X = f_1 \cdot \delta X_1 + f_2 \cdot \delta X_2 \tag{2.10}$$

In the numerical ranges of interest in this paper, the deviations from the exact values by applying these approximations are less than $0.06\text{\textperthousand}$ for oxygen (range $-300...0\text{\textperthousand}$) and $0.14\text{\textperthousand}$ for hydrogen (range $-1000...0\text{\textperthousand}$) isotopes.

2.3   Fractionation Processes

2.3.1   Equilibrium Fractionation

Due to the different masses of the isotopes, the zero-point energy of a water molecule is shifted by replacing a main by a rare isotope. This influences the vapor pressure, so that the lighter isotopologue is preferred in evaporation and the heavier in condensation. In equilibrium, the vapor is depleted in heavy isotopologues with respect to the condensate:

$$R_c = \alpha(T) \cdot R_v \tag{2.11}$$

where R_v denotes the vapor phase and R_c the condensate (either liquid, R_l, or solid, R_s). $\alpha > 1$ is the temperature-dependent equilibrium fractionation factor and is given by [Merlivat and Nief, 1967, van Hook, 1968, Majoube, 1968, 1971, Jancso and van Hook, 1974]:

vapor $\longleftrightarrow$ liquid:

$$\ln^2 \alpha_{vl} = \frac{15013 K^2}{T^2} - 0.1 \tag{2.12}$$

$$\ln^{18} \alpha_{vl} = \frac{1137 K^2}{T^2} - \frac{0.4156 K}{T} - 0.0020667$$

$$\ln^3 \alpha_{vl} \approx \frac{46480 K^2}{T^2} - \frac{103.87 K}{T}$$

vapor $\longleftrightarrow$ solid:

$$\ln^2 \alpha_{vs} = \frac{16289 K^2}{T^2} - 0.0945 \tag{2.13}$$

$$\ln^{18} \alpha_{vs} = \frac{11.839 K}{T} - 0.028224$$

However, it has to be noted that the functions given above are best-fits for data in the range of $-40...100C$ only. As the temperature-dependence increases at lower temperatures, more adequate data ranges would be desirable for atmospheric applications where temperatures $< -80C$ can be encountered.

For easier use in connection with δ-values, the fractionation constant $^x\epsilon = (^x\alpha - 1) \cdot 1000‰$ is often used instead of α when discussing isotopic behavior.

2.3.2   Kinetic Fractionation - Diffusion

During non-equilibrium conditions (e.g. evaporation), kinetic fractionation may occur. The diffusion constant D is dependent on mass. It can be approximated by [Roedel, 2000]

$$D \approx \frac{1}{3} \cdot v \cdot l \tag{2.14}$$

where l is the mean free path length and v the mean thermal velocity, $v = \sqrt{\frac{8kT}{\pi m}}$. Therefore, the diffusion constant is smaller for heavier molecules, and vapor removed during evaporation is more depleted in heavy isotopes than vapor in equilibrium.

The kinetic fractionation factor can be approximated by [Roedel, 2000]

$$^x\alpha = 1 + n \cdot {}^x\varepsilon \cdot (1 - f_{H_2O}) \tag{2.15}$$

where $^x\varepsilon$ is related to the difference in the diffusion constants (e.g. for HDO)

$$^2\varepsilon \approx \frac{D_{H_2O}}{D_{HDO}} - 1 \tag{2.16}$$

$n \approx 0.6$ is an empirical factor and can be described with transfer resistance theory [Merlivat, 1978, Ehhalt and Knott, 1965]. Typical values at $21C$ and 50% humidity are

	α	ε
HDO	1.0075	0.0251
$H_2^{18}O$	1.0085	0.0285

The kinetic fractionation for $H_2^{17}O$ can be expected to be the same as for HDO, as both share the same $m = 19$.

2.3.3   Kinetic Fractionation - Rate Constants

Through the mass-dependency of the collision frequency (this is also a kinetic effect) and the energy levels, the rate constants for the formation and destruction of molecules differ slightly between isotopologues [Bigeleisen, 1949]. A reaction of the form

$$A + B \longrightarrow C + D \tag{2.17}$$

will have the reaction rates

$$\frac{d[A]}{dt} = \frac{d[B]}{dt} = -\frac{d[C]}{dt} = -\frac{d[D]}{dt} = -k \cdot [A] \cdot [B] \tag{2.18}$$

The reaction coefficient k can usually be written as

$$k = A \exp\left(-\frac{E}{RT}\right) \tag{2.19}$$

with the activation energy E. By substituting an isotopologue in 2.17, one will obtain a reaction constant ^xk, where $^xk =^x \alpha \cdot k$. $^x\alpha$ is generally ≤ 1 as the collision frequency is higher for lighter molecules, and can also depend on temperature if the zero-point energies of the isotopically substituted molecules differ.

2.3.4   Isotope Exchange

An interesting feature of isotope systems is that molecules of different chemical species can exchange isotopes without changing their chemical nature [Urey, 1947, Bigeleisen and Mayer, 1947]:

$$XA + YB \longleftrightarrow XB + YA \tag{2.20}$$

where A and B represent isotopes of the same element and X, Y the remainder of the molecules involved. As indicated, isotope exchange is a two-way process, therefore forward and backward reactions have to be considered. The mathematical description of this process is analogue to chemical fractionation processes.

2.3.5   Mass Independent Fractionation (MIF)

It is generally believed that in systems with more than one rare isotope, e.g. the triple isotope system ^{16}O, ^{17}O and ^{18}O, the abundance of a rare isotope is related to the other by the *mass dependent fractionation (MDF) law* (for a detailed description of MDF see Young et al. [2002]). Both equilibrium and kinetic fractionation follow a relationship of the form

$$1 + \delta^{17}O = (1 + \delta^{18}O)^{\lambda} \tag{2.21}$$

which is often approximated by

$$\delta^{17}O = \lambda \cdot \delta^{18}O \tag{2.22}$$

However, this approximation is only applicable for small δ-values. In the context of this thesis, large deviations will be discussed, so that the power law must be applied.

The exponent λ differs slightly for equilibrium and kinetic fractionation. In equilibrium fractionation, it can be written as [Young et al., 2002]

$$\lambda = \frac{1/m_1 - 1/m_2}{1/m_1 - 1/m_3} \tag{2.23}$$

where (m_1, m_2, m_3) represent the masses of the isotopes involved, e.g. (16, 17, 18) for the triple oxygen system ($\lambda = 0.529$ for oxygen).

In kinetic fractionation processes, λ is given by [Young et al., 2002]

$$\lambda = \frac{\ln\left(\dfrac{M_1}{M_2}\right)}{\ln\left(\dfrac{M_1}{M_3}\right)} \tag{2.24}$$

where $(M_1,\ M_2,\ M_3)$ are the atomic, molecular or reduced masses of the isotopologues in motion. For water, $\lambda = 0.513$ in kinetic fractionation.

Meijer and Li [1998] have confirmed the MDF law on a wide range $(\delta^{18}O = -50... + 10‰)$ of natural water samples. Their best fit yields the equation

$$1 + \delta^{17}O = (1 + \delta^{18}O)^{0.528} \tag{2.25}$$

The exponent 0.528 agrees with $\lambda = 0.529$ for equilibrium fractionation within the errors stated by Meijer and Li [1998] (0.5281 ± 0.0015).

In contrast to the mass dependent fractionations described above, another fractionation process has been discovered in the production of ozone. Mauersberger [1981] observed a very high $\delta^{18}O$-enrichment in ozone by in situ mass spectrometry. Laboratory production of ozone by Thiemens and Heidenreich [1983] revealed a deviation from the MDF law, with $\delta^{17}O \approx \delta^{18}O$ instead of $\delta^{17}O \approx 0.5 \cdot \delta^{18}O$. Deviations from MDF were later confirmed by ozone measurements in the stratosphere [Schueler et al., 1990] and the troposphere [Krankowsky et al., 1995]. It was concluded that in addition to the known mass dependent fractionation of isotopes a new, *mass independent fractionation (MIF)* had been discovered. Up to date, the nature of this process is still under discussion [Gao and Marcus, 2001]. A review about the isotopic composition of ozone is given by Mauersberger et al. [2001].

In the meantime, measurements on other oxygen bearing species like CO_2, N_2O and CO have also shown deviations from the MDF law. It is believed that in many cases these anomalies are transfered into these species from ozone either directly or indirectly. For CO_2, a transfer process via $O(^1D)$ was first proposed by Yung et al. [1991]. The MIF in tropospheric N_2O can be explained to result from the MIF transfer from O_3 to NO and subsequent reactions [Röckmann et al., 2001, Kaiser, 2003]. However, this MIF effect is not limited to ozone photochemistry alone. CO is believed to gain some of its MIF signature in the preferential removal of ^{18}O in the sink reaction $CO + OH$ [Röckmann, 1998].

The magnitude of this anomaleous isotope effect is often described as the deviation from the MDF-line:

$$\Delta^{17} \approx \delta^{17}O - \lambda \cdot \delta^{18}O \tag{2.26}$$

It must be noted, however, that authors differ in the choice of λ. Typical choices are 0.5, 0.52 or 0.516. This is due to three reasons: (a) equation 2.26 results from a linearization of a power law (see above), (b) the choice of λ depends on the range of δ-values on which the reference material has been measured, and (c) λ is not independent of the isotopic composition of the reference material. More on this issue has been written by Miller [2002], who suggests the more robust notation

$$\Delta^{17} = \left(\ln(1 + \delta^{17}O) - \lambda \cdot \ln(1 + \delta^{18}O) \right) \cdot 1000\text{‰} \tag{2.27}$$

where $\lambda = 0.528$ for H_2O as measured by Meijer and Li [1998]. This notation will be adapted in this thesis from now on, though some values cited from other authors may still be with reference to equation 2.26.

Emphasis should be given to the aspect that the above notation 2.27 expects water to be equilibrium-fractionationed. In case of a sample that has undergone kinetic fractionation instead, 2.27 will indicate an isotope anomaly although kinetic fractionation is mass dependent, but with a different value for λ. Consider a sample that has undergone kinetic fractionation to $\delta^{18}O = -300.0\text{‰}$. Applying 2.21 with $\lambda = 0.513$, one obtains $\delta^{17}O = -167.2\text{‰}$. Inserting these values in 2.27 results in $\Delta^{17} = 5.4\text{‰}$. It is therefore very important to distinguish the different processes involved and acknowledge the existence of different values for λ before claiming a sample to have an isotope anomaly.

Due to the high errors in $\delta^{17}O$ and $\delta^{18}O$ measurements, no MIF has been observed in atmospheric water vapor so far. However, it is thought that MIF can be transfered to H_2O via HO_x, NO_x and odd oxygen chemistry in the stratosphere. Lyons [2001] calculates the Δ^{17} of OH in the midlatitudinal stratosphere to be $2...45\text{‰}$. By $H-$ abstraction from species like CH_4, this signature can be implemented into water produced inside the stratosphere and give valuable insight into the amount of water produced versus the flux of water from the troposphere. A more detailed analysis of the photochemistry of water vapor is found in chapter 4.

2.3.6   Rayleigh Processes

In order to understand the isotopic change of a substance during destruction or phase change, a simple model can be derived. Given an initial amount N_0

and initial isotope ratio R_0 of a substance and considering a single sink which fractionates with a constant factor α, one is interested in the isotope ratio R of the remaining fraction after some of the substance has been destroyed by the sink process. Using the mass balance 2.9 for infinitely small changes dN and dR, one obtains

$$R \cdot N = (R + dR) \cdot (N + dN) - \alpha \cdot R \cdot dN \tag{2.28}$$

which can be integrated to

$$R = R_0 \cdot \left(\frac{N}{N_0} \right)^{\alpha - 1} \tag{2.29}$$

or, in δ-notation

$$\delta X = (1 + \delta X_0) \cdot \left(\frac{N}{N_0} \right)^{\alpha - 1} - 1 \tag{2.30}$$

This equation can be rearranged to yield

$$\ln(\delta X + 1) = \ln(\delta X_0 + 1) + (\alpha - 1) \cdot \ln \left(\frac{N}{N_0} \right) \tag{2.31}$$

This form of the equation is often used when plotting δ-values versus the amount of a trace gas, as δX_0 and α can be obtained from the slope and intercept of the linear regression line.

Processes obeying this equation are called *Rayleigh-Processes*. However, atmospheric water vapor does not strictly follow simple Rayleigh fractionation, as the atmospheric water cycle is far more complex. During ascent and cloud formation, the temperature of the air parcels can change from about $+35C$ in the tropics to about $-80C$ in the tropical tropopause region, leading to huge changes in the temperature dependent fractionation factor α. For example, $^2\alpha$ changes in the mentioned temperature range from 1.060 ($+35C$ over liquid water) to 1.409 ($-80C$ over ice). These changes have to be included in models, so that at any point only the differential equation 2.28 is valid and has to be evaluated numerically. Further, turbulent vertical mixing transports depleted water vapor from above to lower altitudes and vice versa, therefore attenuating the Rayleigh process. More detail on dehydration processes is given in section 3.2.2.

Chapter 3

Water Isotopologues in the Atmosphere

3.1 The Layers of the Atmosphere

The atmosphere is commonly divided into different layers according to its temperature profile. In the lowest layer, the *troposphere*, a temperature gradient of $-0.5...1K/100m$ is encountered. The heat source at the ground beneath the cold sink (IR cooling of water vapor in the upper troposphere (UT)) leads to instable or neutral conditions, therefore enhancing vertical mixing.

The next layer is the *stratosphere*. Driven by absorption of solar radiation in the UV, temperature rises again with altitude. This leads to a stable stratification, whereby IR radiation of water vapor in the troposphere below acts as a heat sink. A vertically displaced air parcel will try to obtain its original vertical position, thus vertical exchange is much slower than in the troposphere.

Nested between troposphere and stratosphere is the *tropopause*. It's vertical position varies according to latitude from about $7km$ in the polar regions up to $18km$ in the tropics. There exist several commonly used definitions for the tropopause:

- **thermal tropopause:** According to the World Meteorological Organization, the tropopause is the lowest height of an approximately $2km$ thick layer. Inside this layer, the temperature gradient is always higher than $-0.2K/100m$ (increase in static stability with altitude).

- **dynamical tropopause:** The *potential vorticity* (PV) of the dynamical tropopause has a constant value of $\mid PV_{tropopause} \mid = 1.6PVU$.

The potential vorticity is constant for adiabatic, isentropic transport and is defined as

$$PV = -g \cdot \frac{\partial \theta}{\partial p} \cdot (rot_z \vec{v} + 2 \cdot \Omega_z) \qquad (3.1)$$

with

g = gravitational acceleration, $9.81 \frac{m}{s^2}$
θ = potential temperature (see below)
p = pressure
$\vec{v}$ = aerial velocity
Ω_z = vertical component of rotational velocity of earth

Potential vorticity is usually given in units of $1 PVU = 10^{-6} \frac{K \cdot m^2}{kg \cdot s}$.

The *potential temperature* θ is the temperature a given air sample would have if adiabatically brought to standard pressure $p = 1013 hPa$. Surfaces of constant potential temperature are called *isentropes*, because constant potential temperature is equivalent to constant enthropy:

$$\theta = T \cdot \left(\frac{p_0}{p} \right)^{\frac{\kappa - 1}{\kappa}} = T \cdot \left(\frac{1013 hPa}{p} \right)^{0.286} \qquad (3.2)$$

The position of the thermal and dynamical tropopause may differ, especially during vertical transport. During an adiabatic, isentropic, vertical transport process, the PV is conserved. This does not necessarily hold for static stability [Roedel, 2000].

To complete the picture of a layered atmosphere, one has to mention the *mesosphere* and the *thermosphere*. The mesosphere is a layer above the stratosphere and extends from $\approx 50...80 km$, characterized by a negative temperature gradient. In the thermosphere ($\approx 80 km$ and above), temperature rises again and reaches over $1000 C$. Mesosphere and thermosphere are separated from stratosphere and mesosphere by the stratopause and the mesopause, respectively.

3.2   Global Circulation

3.2.1   Stratosphere-Troposphere Exchange (STE)

The photochemical behavior of many trace gases differs vastly in the stratosphere and the troposphere. Vertical exchange acts on time scales of hours to days in the

troposphere, which is in contrast to the years an air parcel needs to rise to the top of the stratosphere. Thus simple atmospheric models often treat the stratosphere and the troposphere as two separate boxes. Stratosphere-troposphere exchange in such a two-box model is usually assumed to have a characteristic time scale of $\approx 1.4 - 2a$.

A more detailed view has to take into account the sensitivity of an atmospheric species to altitude and latitude. The key to understanding STE is therefore detailed knowledge about the pathways over which atmospheric mass enters and leaves the stratosphere. Here, a brief overview will be given, with emphasis on the transport of water vapor.

First, the position of the tropopause has to be defined. As already mentioned above, there are several definitions of the tropopause. In order to define the tropopause as the separation layer between the stratosphere and the troposphere, one has to use two definitions at different latitudes. Figure 3.1 depicts the dynamical aspects of STE. In the tropics, the tropopause coincides roughly with the $\theta = 380K$ isentrope, which is the lower boundary of the stratospheric "overworld". At mid and high latitudes, the tropopause is more accurately described as the $1.6PVU$ surface. Between this $1.6PVU$ surface and the $380K$ isentropic surface lies the "lowermost" stratosphere, whose exchange processes differ from the ones encountered in the tropics.

In the high reaching convective towers of the tropics, the tropopause can reach altitudes of up to $18km$. Air detraining at this altitudes ascends into the stratosphere via heating by solar radiation. Due to the high location of the tropopause, this air mass is strongly dehydrated; details are given below in section 3.2.2.

Once in the stratosphere, the air is transported polewards by the wave-driven extratropical "pump" [Holton et al., 1995]. As here the solar irradiation is less intense than in the tropics, the air masses diabatically cool and sink again below the $380K$ surface into the lowermost stratosphere. Since the tropopause intersects the isentropes, adiabatic transport processes can occur between the lowermost stratosphere and the troposphere, such as tropical tropospheric troughs and their cutoff cyclones, and tropopause folds at mid latitudes (see figure 3.2). Here, large displacements of the tropopause are generally associated with growing upper tropospheric cyclones. The tropopause can form distorted tongues, stretching out in long filaments. Eddy mixing at the surface of these filaments can mix both stratospheric air into the troposphere and vice versa (see Holton et al. [1995] for more details).

Another interesting aspect of STE of water vapor is the dehydration of the arctic vortex during winter by sedimentation of polar stratospheric cloud particles, which is described in section 3.2.4.
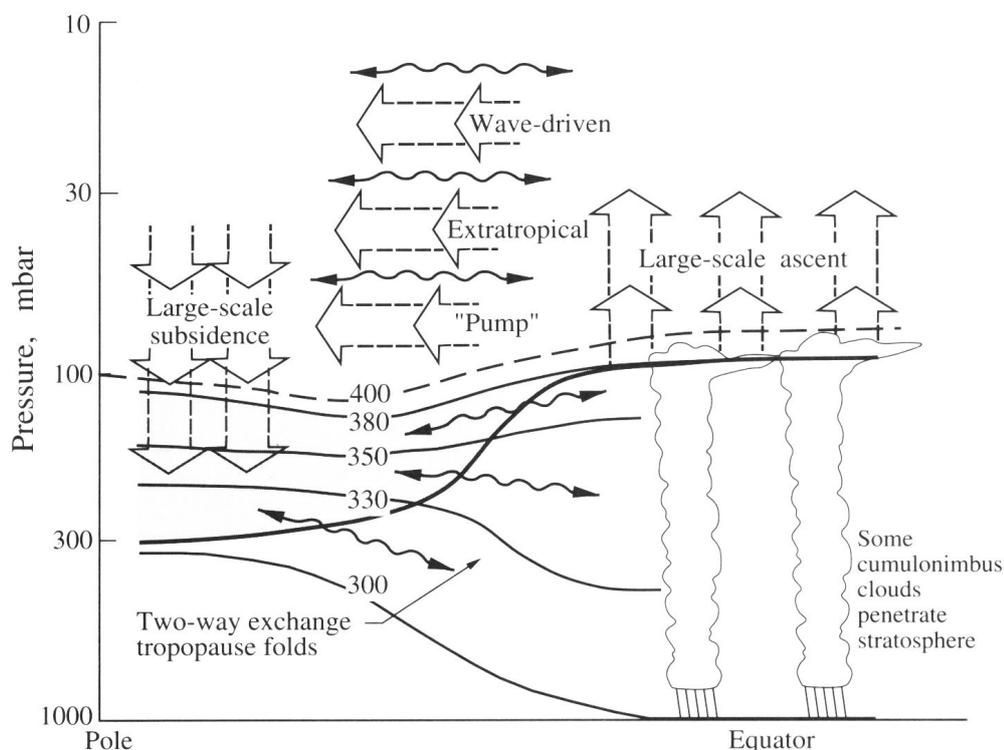
Figure 3.1 : *Stratosphere-troposphere exchange as described by Holton et al. [1995]. Air rises in the hot towers in the tropics. Air detraining at their top enters the stratospheric "overworld", denoted by the $\theta = 380K$ surface, via diabatic heating. The wave-driven extratropical "pump" transports the air polewards, where diabatic cooling brings it below the $380K$ surface. Here, two-way transport along isentropes is possible via adiabatic small-scale processes.*

3.2.2 Dehydration Models

There is consent that water vapor primely enters the stratosphere via the tropical tropopause [Brewer, 1949]. However, the mechanisms that dehydrate air prior to its entry into the stratosphere are not well understood up to date. As recent studies by Oltmans et al. [2000] and Rosenlof et al. [2001] have shown, water vapor concentrations in the stratosphere have risen by approximately 50% during the last 50 years. Given the importance of water vapor for the radiation balance and chemical processes in the stratosphere, deeper insight into the stratospheric water cycle is desired.

It has been observed that the water vapor content of air entering the LS to
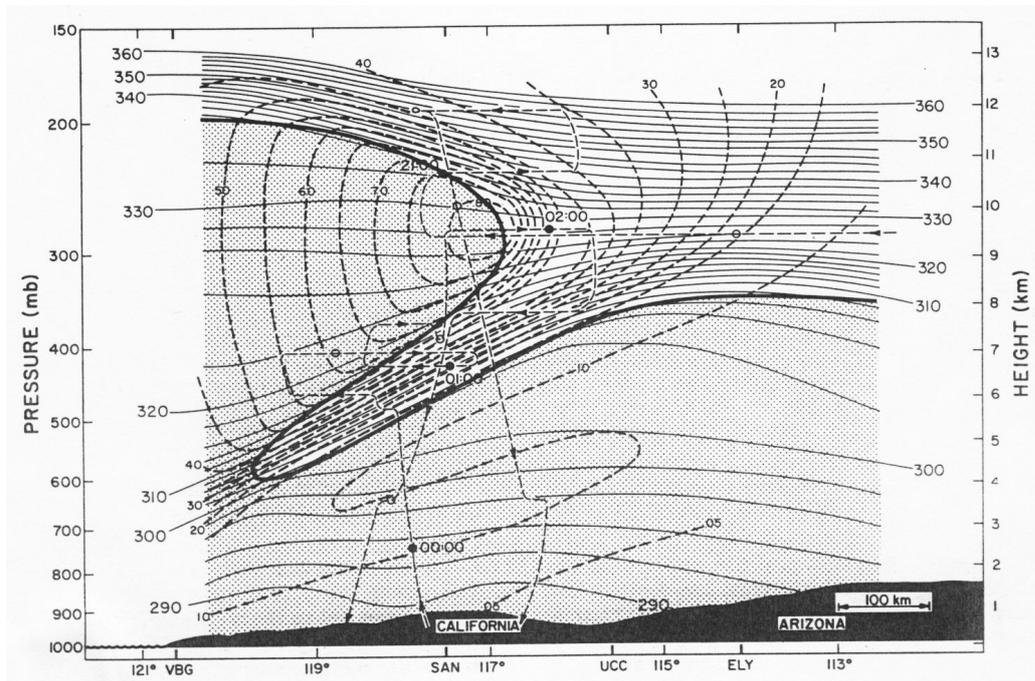
Figure 3.2 : *Cross section through a tropopause fold [Shapiro, 1980]. Shown is the potential vorticity tropopause (thick solid line), potential temperature (thin solid lines), and wind speed (in m/s, dashed contours).*

$4.1ppm$ is lower than the saturation vapor pressure of the global mean tropopause temperature ($\approx 4.5ppm$) [WMO, 2000]. Newell and Gould-Stewart [1981] developed the "Stratospheric Fountain" hypothesis, in which air mainly crosses the tropopause in regions with a very low tropopause temperature. This fountain should occur over the western tropical Pacific, northern Australia, Indonesia and Malaysia in northern hemisphere winter. But later observations by Mote et al. [1996] showed that air crosses the tropopause throughout the year and is not limited to the cold spots, hence contradicting the stratospheric fountain hypothesis.

It is now believed that the dehydration of air entering the stratosphere is a two-step process. In the first step, air is dehydrated to mixing ratios much below stratospheric vapor concentrations by a mechanism producing very low temperatures. It then mixes with moister air in the tropopause region before diabatically ascending into the stratosphere.

Two competing mechanisms have been proposed that could dehydrate water vapor in the *tropical tropopause layer (TTL)* to its observed values: *convective*

dehydration and *gradual dehydration*. Though there has been quite some discussion about which of these two processes actually occurs, a recent publication by Webster and Heymsfield [2003] shows that a mixture of both processes seems to be responsible for the dehydration of air entering the stratosphere through the TTL.

Models that correctly describe this dehydration process have to get a high number of parameters right. Temperature is controlled by adiabatic uplift, latent heat release by condensation processes and radiative balance of mainly IR-cooling and UV-heating. Vertical waves mainly influence temperature via adiabatic processes, but during condensation also latent heat transfer becomes important. Condensation is controlled by the temperature dependent water vapor pressure (equations 2.1 and 2.2) over ice or liquid particles, whereby supersaturations are also possible. Small particles can be uplifted, whereas large particles sedimentate towards the ground. The particles can reevaporate and hence hydrate dryer air parcels.

Thus, models describing the dehydration process of air entering the stratosphere are of very complex nature. As modeling of condensation processes is not a central part of this thesis, the interested reader should consult other literature (e.g. Jensen and Pfister [2004] and references therein). However, distinct processes during dehydration leave an "isotopic fingerprint" on the vapor of a dehydrated air parcel, which will be briefly investigated here.

Convective Dehydration

Sherwood and Dessler [2000] hypothized the existence of a "mixing layer" near the tropical tropopause. This layer spans from the zero net balance heating level $\theta \approx 350K$ ($\approx 150hPa$, $14km$) to the highest level that convection reaches, $\theta \approx 420 - 450K$ ($\approx 50 - 70hPa$, $18 - 20km$). The bottom of the TTL is close to the level of neutral buoyancy (LNB) of tropical convection.

Air detraining near the bottom of the TTL with $\approx 10 - 15ppm$ will be moist as compared to lower stratospheric mixing ratios of $\approx 4ppm$. Drier air is produced in freeze-drying in convective overshoots detraining at levels higher than their LNB. This dry air mixes with high-θ stratospheric air and starts descending to its LNB, which now is higher than the LNB of the original convective air parcel, as the stratospheric air mixed into it increases its potential temperature. Over time, it mixes with air which has detrained below and has slowly risen to this altitude by radiative heating. This mixture rises further by radiative heating and enters the stratosphere dehydrated to lower stratospheric mixing ratios (see figure 3.3).
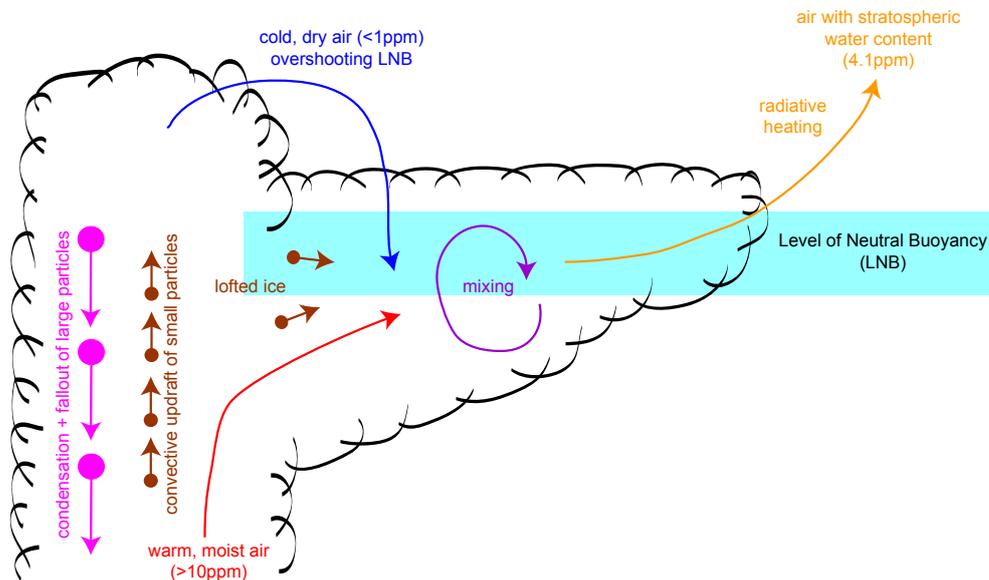
Figure 3.3 : *Convective Dehydration. Air overshooting its LNB dehydrates to vapor concentrations much below stratospheric values. Descending towards its new LNB, it mixes with moist air which has detrained below its LNB. It then enters the stratosphere dehydrated to stratospheric entry concentrations via radiative heating.*

The amount of mass detraining above its LNB has to be sufficiently high in order to account for the low mixing ratios observed. Based on measurements of H_2O and CO, Dessler [2002] estimates that nearly 60% of air crossing the $380K$ surface detrained between $370K$ and $380K$, a level much higher than the LNB of typical tropical convection. Compared to slow ascent, which requires roughly 1 to 2 months to elevate air from the typical detrainment height to the tropopause, this layer could be completely replaced with tropospheric overshooting air in the same time if only 5% of midtropospheric updrafts mixed into it [Sherwood and Dessler, 2001].

It is also not quite clear whether the overshooting air in the hot towers really loses all its surplus moisture. The air has to remain at low temperatures long enough to allow for the sedimentation of the formed particles. If this is not the case, at least some of these cloud tops could actually add moisture to the stratosphere. Recent simulations by Gettelman et al. [2004] using the MOZART model indicate that the Asian monsoon circulation may contribute 75% of the total net upward water vapor flux in the tropics at tropopause levels during the monsoon season, some of which may cross the tropopause in convective events.
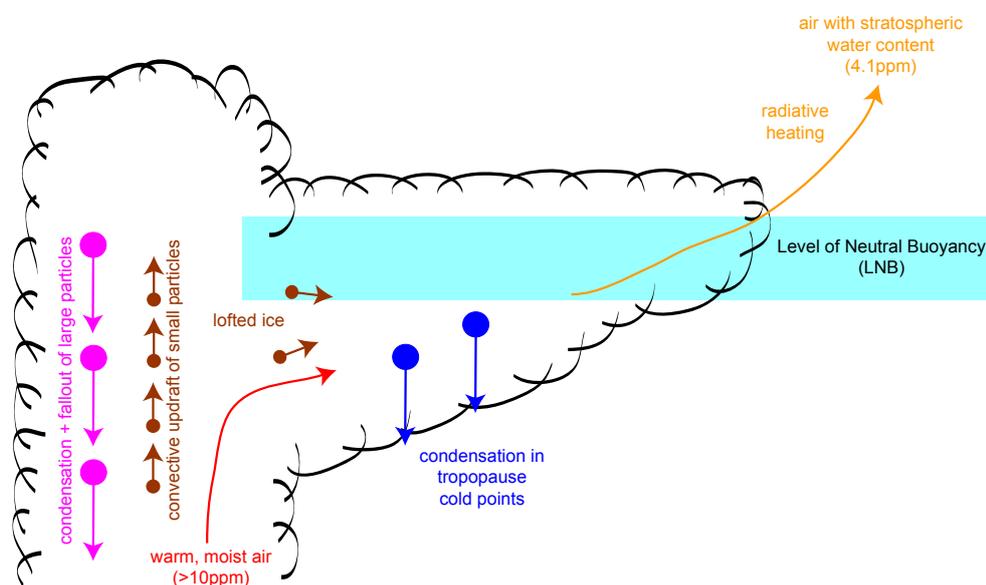
Figure 3.4 : *Gradual Dehydration. Air detrains below its LNB. During slow ascend, high vertical velocity transports it to regions with a very low tropopause temperature. Here it dehydrates below stratospheric concentrations before mixing again with moister air. It then enters the stratosphere dehydrated to stratospheric entry concentrations via radiative heating.*

Gradual Dehydration

In a gradual dehydration model, air detrains from convective updraft beneath its LNB. Dehydration occurs during slow ascent to its LNB, followed by diabatic transport into the stratosphere across the tropical tropopause. This mechanism alone could not explain the undersaturated air entering the stratosphere.

Holton and Gettelmann [2001] argue that horizontal motion in the tropopause region with a velocity $\approx 5m \cdot s^{-1}$ is much faster than vertical motion with $\approx 0.5mm \cdot s^{-1}$. Therefore, an air parcel travels several thousand kilometers while only rising some hundred meters. During this large scale horizontal motion, the air visits some "cold spots", e.g. the cold spots over the western Pacific mentioned above. Here it freeze-dries to much below stratospheric conditions. Mixing with moister air from the tropopause downstream of this cold trap, air reaches stratospheric water vapor concentrations and is diabatically lifted into the stratosphere (see figure 3.4).

3.2.3 Isotopic Fingerprints of the Dehydration Models

The influence of the two proposed mechanisms for the isotopic composition of water vapor in the TTL has been modeled by Dessler and Sherwood [2003]. They rely heavily on data published by Kuang et al. [2003] which show - with the effects of methane oxidation removed - a constant δD-value of $-650‰$ throughout the TTL. However, the resolution of this data is quite coarse ($2km$ vertical, $200km$ horizontal). Data with a better resolution was published by Webster and Heymsfield [2003], showing a large variation of δD-values throughout the TTL. The conclusions to be drawn from this will be explained below.

The models discussed here only include hydrogen isotopes. Oxygen isotopes are believed to follow the same behavior though the effects are smaller, as the temperature dependent fraction factor for condensation is smaller. It is further believed that water vapor enters the stratosphere without a Δ^{17} anomaly, as condensation is a pure mass-dependent process.

Gradual Dehydration

Figure 3.5 shows the effects of Rayleigh-distillation upon air rising in convective towers. During ascend, air expands and cools, and condensate is formed. The isotopic composition of the condensate depends on the isotope ratio of the vapor at a given height and the temperature dependent fractionation factor α. The temperature of the air parcel depends on its adiabatic expansion, the amount of condensate formed (transfer of latent heat) and, at higher altitudes, its radiation balance.

The blue line shows a pure Rayleigh-distillation process where all condensate is removed immediately from the air parcel. Such a process would lead to a high deuterium depletion with values less than $-900‰$ in the TTL. However, such high depletions are usually not observed in the TTL. Moyer et al. [1996] concluded that ice particles could be lofted in convective updrafts and reevaporate in the TTL. As these ice particles have formed at lower levels, they are enriched in deuterium relative to the vapor and therefore attenuate the Rayleigh effect. Another possibility for the higher deuterium values observed could be nonequilibrium effects found in supersaturated air parcels. However, this possibility was dismissed by Keith [2000], showing that the δD-$\delta^{18}O$ relationship in the TTL could not be explained by kinetic effects.

To account for the lofted ice particles, Dessler and Sherwood [2003] used the mean value of δD at the bottom of the TTL as found by Kuang et al. [2003] and modeled in-situ condensation in the TTL (red line in figure 3.5). As some air
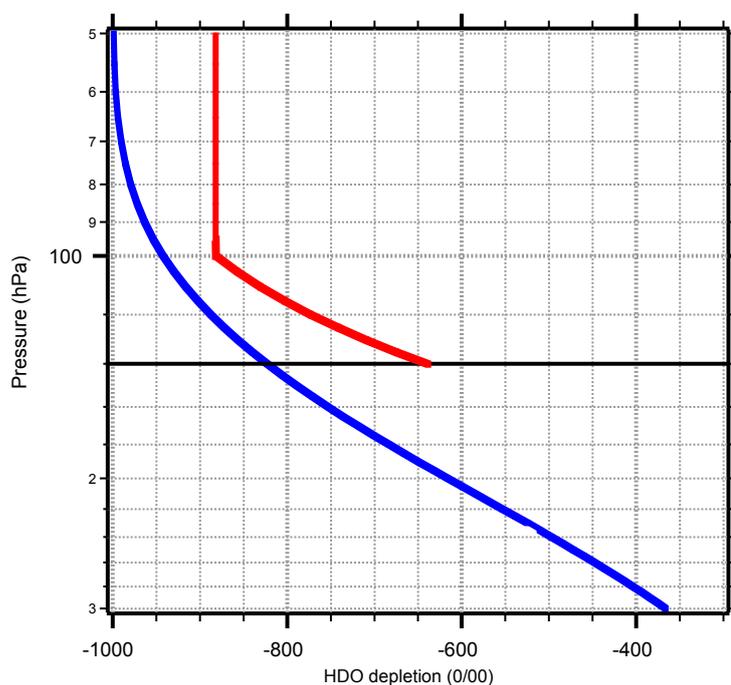
Figure 3.5 : *Isotopic composition of gradual dehydration in the model of Dessler and Sherwood [2003]. The bottom of the TTL is shown as horizontal line at $120hPa$. The blue line shows the isotopic composition of a pure Rayleigh distillation process. The red line shows a process where ice particles are lofted to the bottom of the TTL and reevaporate, followed by Rayleigh distillation inside the TTL.*

could also follow a pure Rayleigh process, one would expect δD-values somewhere between these two lines in the TTL.

Convective Dehydration

In principle, convective Dehydration will show the same behavior of Rayleigh fractionation throughout its convective updraft as in gradual dehydration. But as some air overshoots its LNB, it will become very dry and very depleted in δD. Mixing air from this high level with air from below results in a near constant δD profile throughout the TTL. This is due to the higher mixing ratio of the lower altitude air parcel. In figure 3.6 such a mixing line is shown. The sharp bend occurs where about 95% of the air parcel consists of air from the higher level.
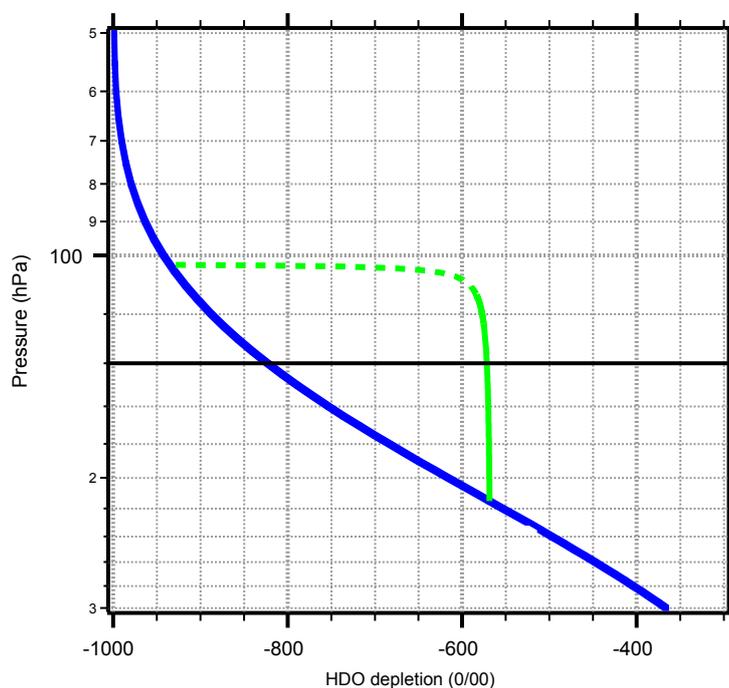
Figure 3.6 : *Convective dehydration in the model of Dessler and Sherwood [2003].
The bottom of the TTL is shown as solid line at $120hPa$. Air parcels follow a process
close to Rayleigh distillation (blue line) during dehydration. Mixing of air parcels from
a high level with air from below results in a steep mixing line (green line) until most
of the air comes from the higher level. The dashed line shows where more than 95%
of air is from the higher level.*

Dessler and Sherwood [2003] tested this model on the HDO profile obtained
by Kuang et al. [2003] from the ATMOS spacecraft. They concluded that the
retained ice/vapor ratio had to be roughly $1:4$ and the isotopic composition of
the lofted ice had to be $-565‰$ in order to explain the observed water vapor
mixing ratios and the stratospheric δD-entry level. However, the most distinct
feature of this model - the constant δD-profile - did neither depend on the
ice/vapor ratio nor the isotopic composition of the ice.

The Complete Picture - a Mixture of both Processes?

Webster and Heymsfield [2003] published the first high resolution dataset of the
isotopic composition of water vapor in the UT/LS zone, comprising more than
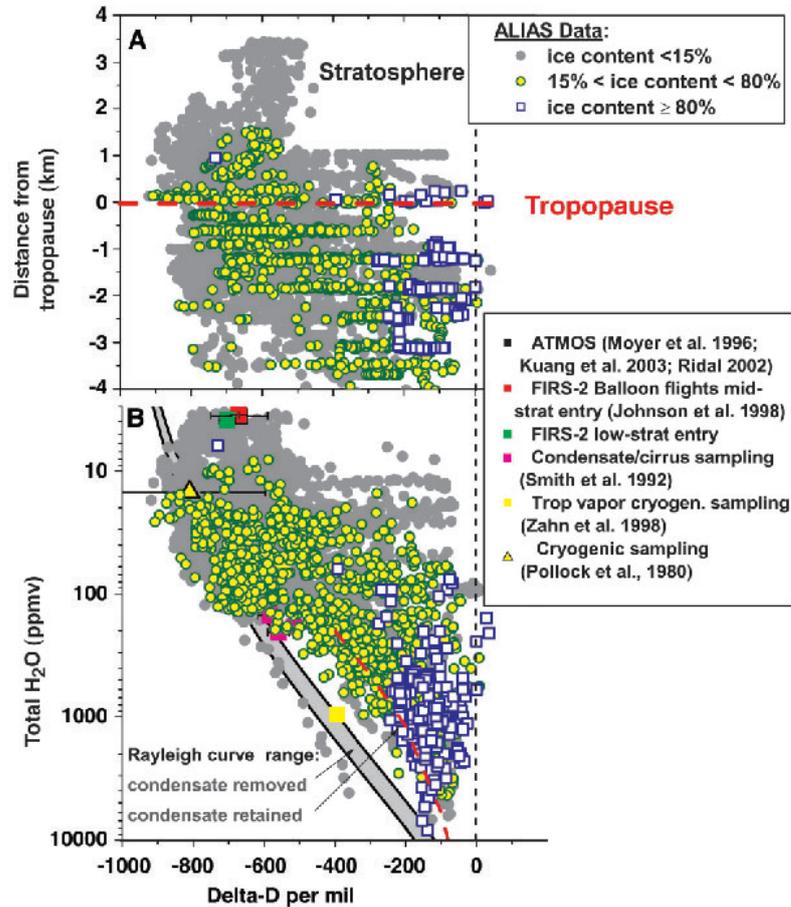
Figure 3.7 : δD *intercomparison by Webster and Heymsfield [2003]. Samples are divided into vapor ($\leq 15\%$ ice), ice ($\geq 80\%$ ice) and intermediate samples.*

3000 datapoints of vapor and more than 150 of ice. They show that δD in vapor shows a large variation ($0.. -950\%$) in this zone, while the composition of samples largely consisting of ice is around -130% (see figure 3.7), thus seemingly contradicting both gradual and convective dehydration models.

In a sub-dataset of samples in the TTL (figure 3.8), Webster and Heymsfield [2003] pointed out that the high variability in the vapor samples could not be explained by either gradual or convective dehydration alone, but that both processes must occur. Whereas each of these two processes leaves an isotopic mark on an air parcel, horizontal mixing fills the gap between the two marks. During further ascend, the air mixes until it reaches a homogeneous state at the top of the TTL and enters the stratosphere with an isotopic entry level representing a
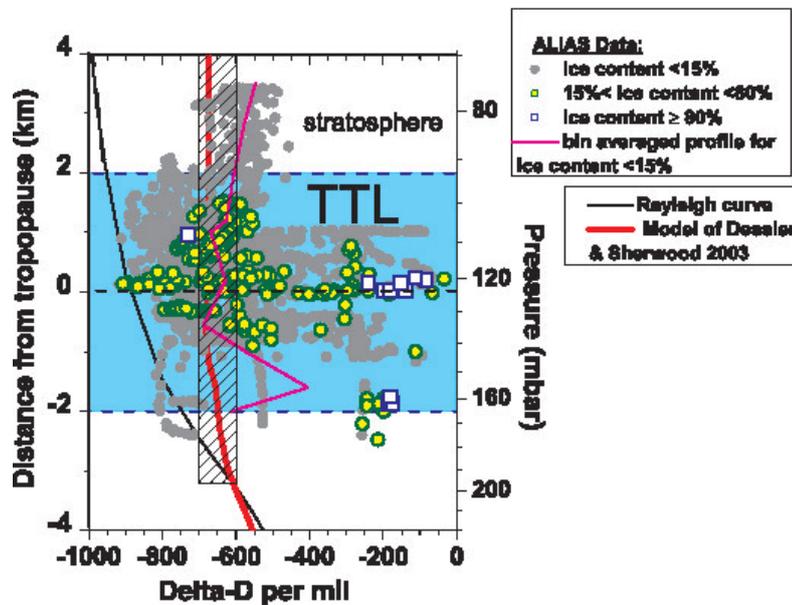
Figure 3.8 : *Samples of Webster and Heymsfield [2003] taken in the TTL. Note the high variability in the vapor composition, which is thought to stem from mixing of air parcels that have undergone both gradual and convective dehydration.*

mixing point of the two processes.

3.2.4 The Sedimentation of Polar Stratospheric Cloud Particles

During the Antarctic winter, very cold temperatures of less than $195K$ are encountered in the Antarctic polar vortex. At these temperatures, particles can form from HNO_3 and H_2O (nitric acid trihydrate, NAT), below $188K$ even from pure water. These particles are called polar stratospheric cloud (PSC) particles, and classified as PSC-I and PSC-II, respectively. On their surfaces, inactive chlorine reservoir gases like HCl and $ClONO_2$ can heterogeneously form active chlorine substances. At the same time, inactive nitrogen compounds can be transformed into active substances. Both processes combined lead to massive ozone destruction in the polar spring, when the first sunlight starts the catalytic ozone destruction cycle caused by the active chlorine compounds (see Toon and Turco [1991] for details).

As the PSCs can grow to diameters in the μm range, they can sediment and leave the stratosphere [Drdla and Turco, 1991]. The polar vortex becomes dehydrated and denitrified, and the reformation of inactive chlorine compounds is hindered in spring, leading to a prolongation of the ozone destruction cycle. The ozone "hole" disappears later in spring, when warmer temperatures lead to a break-up of the polar vortex, and its air mixes with the surrounding stratosphere.

As was shown by Zahn et al. [1998], measurements of HTO are potentially able to detect the sedimented particles even close to the tropopause. As will be shown in section 4.6.1, the tritium ratio of background HTO increases from tropopause level to the middle stratosphere, where PSC formation is likely, by a factor of ≈ 50. Water incorporated into a PSC particle is therefore very rich in tritium. If it sediments downward into the tropopause region and evaporates, it releases its high tritium content and increases the local tritium ratio. Zahn et al. [1998] developed a simple model describing this process, which - with some minor modifications - is briefly described here.

Consider two layers of the atmosphere, one from tropopause level to $\approx 3km$ above, and one from $17 - 22km$, where PSC formation is likely to happen. The lower level has a water vapor mixing ratio of $30ppm$, the upper $5ppm$ and $T = 193K$. The HTO background in the tropopause region is not yet well quantified, but Zahn et al. [1998] measured it to be $\approx 10\,atoms/mg\,air$. In the upper level, the model presented in section 4.6.1 estimates it to be $\approx 100\,atoms/mg\,air$. If now 10% of the upper layer's water vapor content is transfered to the lower layer via PSC sedimentation, it increases its water vapor content by only $0.5ppm$. However, its HTO mixing ratio doubles! Thus the HTO mixing ratio of the lower layer is very sensitive to already modest dehydration of the middle stratosphere. Measurements of the stable water isotopologues are believed to show a much smaller sensitivity, as the absolute isotope ratio is thought to change only by $\approx 10...20\%$ between the two layers.

Interest in HTO measurements has declined since the 1970s, since tritium released by nuclear bomb tests has stopped. The most recent measurements are the ones presented by Zahn et al. [1998]. In order to quantify PSC sedimentation, it is very crucial to measure its background profile. Therefore, a part of this work has been dedicated to the measurement of tritium in the tropopause region.

Chapter 4

Modeling the Isotopic Composition of Water Vapor

Water in the stratosphere and mesosphere exists - with few exceptions (e.g. PSC particles, leewave condensation) - in the gas phase only. Therefore, the processes necessary to describe its isotopic composition are gas-phase chemistry, photochemistry, isotopic exchange and transport. As water vapor and its derivates (e.g. HO_x) play a very important role in many chemical reactions, models describing the isotopic composition of water vapor are very complex.

The model presented here was originally published as a Master thesis at the University of Heidelberg [Bechtel, 1999]. A revised version was later published for peer review [Bechtel and Zahn, 2003]. However, in the publication process some important questions were raised which needed to be addressed. As further work on the model is is no longer Christian Bechtel's main interest, he gave me access to the source code, so I could write a revised version. I therefore wish to emphasize that I have done the necessary improvements of the code, like including further reactions and detailed analysis of the different reaction pathways, while the main body has been designed by Christian Bechtel.

The original model consists of two source codes - one for hydrogen, one for oxygen isotopes. The revised model described here only uses one source code for both hydrogen and oxygen isotopes. Reactions have been added to provide the full methane decomposition chain. The reaction rates have been revised to be up to date. Some isotopic reaction rates have been simplified, while other isotopic species have been replaced by more accurate species (e.g. HOP and HPO instead of a combined species). Further, detailed analysis of CH_4 and H_2 has been added.

4.1 General Description of the Model

The computer language of the model is *FACSIMILE*, a language especially designed for models using chemistry and transport. The model is one-dimensional, consisting of 65 boxes each $1km$ high from $15-80km$. Pressure and temperature of each box are set according to the *U.S. Standard Atmosphere 1976*. The model is allowed to run for $2 \cdot 10^9 s$ (approximately 64 years), after which equilibrium conditions are ensured.

Transport of the long-lived traces gases H_2O, CH_4 and H_2 is implemented using the vertical eddy diffusion constants from Massie and Hunten [1981]:

$$F_x(z) = -K(z) \cdot M(z) \cdot \frac{df_x(z)}{dz} \qquad (4.1)$$

with

$$
\begin{aligned}
F_x(z) &= \quad \text{flux of species x } [cm^{-2}s^{-1}] \\
K(z) &= \quad \text{eddy constant } [cm^2 s^{-1}] \\
M(z) &= \quad \text{total number density of molecules } [cm^{-3}] \\
f_x(z) &= \quad \text{mixing ratio of species } x \; [1]
\end{aligned}
$$

In order to preserve the concentrations in the lowest box, the derivative of the main species is set to zero. The boundary condition of the uppermost box is set to zero outflow. As stratospheric entry values, the numbers listed below are chosen [Dlugokencky et al., 1994, Quay et al., 1999, Rahn et al., 2003, Röckmann et al., 2003, Moyer et al., 1996, Johnson et al., 2001b, Kuang et al., 2003]:

species	mixing ratio [ppm]	δD ‰	$\delta^{17}O$ ‰	$\delta^{18}O$ ‰
H_2O	3.70	-660.00	-128.00	-69.76
CH_4	1.70	-86.00		
H_2	0.55	130.00		

4.2 Parameter Profiles

The chemical species O_2, O_3, $O(^1D)$, $O(^3P)$, NO, NO_2, CO and Cl are not included as variables in the model; their mixing ratios and isotopic compositions are kept as fixed parameters in each box. In the present version of the model, most of the parameter profiles are the same as used by Bechtel and Zahn [2003].

However, the isotopic composition of the parameter profiles has been changed in some cases where more information has become available.

The mixing ratios of O_3, $O(^1D)$, NO and Cl are as retrieved by the *ECHAM 3* model (2-D)[1]. The $O(^3P)$ profile was measured by *CHRISTA* onboard the Space Shuttle in November 1994[2]. CO was measured by *ISAMS* aboard the *UARS* satellite [Lopez-Valverde et al., 1996]. A NO_2 profile was taken from Brasseur and Solomon [1986]. The parameter profiles are globally, seasonally and diurnally averaged.

The mixing ratio of O_2 is kept at 0.20946, with an isotopic composition $\delta^{17}O = 11.78‰$, $\delta^{18}O = 22.96‰$. $O(^3P)$ is isotopically linked to O_2 via rapid exchange. The fractionation used in the model for $O(^3P)$ is as calculated by Johnston et al. [2000], so that it has $(\delta^{17}O, \delta^{18}O) = (-27.58, -55.30)$.

The isotopic composition of O_3 is set under the assumption that it is solely temperature-dependent [Mauersberger et al., 2001] and that 80% of the enrichment are in the asymmetric QOO molecule. Details are given by Mauersberger et al. [2001], Anderson et al. [1989], Janssen et al. [1999], Mauersberger et al. [1999]. $O(^1D)$ isotopic composition was derived by Bechtel and Zahn [2003] under the assumption that it stems solely from the asymmetric O_3, and that mass-dependent quenching with N_2 and O_2 leads to additional fractionation of $19‰$ and $36‰$ for $\delta^{17}O$ and $\delta^{18}O$, respectively.

For the calculation of the isotopic composition of NO_x, a smaller submodel has been written, and its results are used as parameters in the actual model. It keeps the isotopic composition of O_2, O_3 and $O(^3P)$ fixed as described above. NO, NP, NQ, NO_2, NOP and NOQ are modeled using the reactions

$$
\begin{aligned}
NO + O_3 &\longrightarrow NO_2 + O_2 \\
NO_2 + O(^3P) &\longrightarrow NO + O_2
\end{aligned}
$$

and the isotopic exchange reactions

$$
\begin{aligned}
Q(^3P) + NO &\longleftrightarrow O(^3P) + NQ \\
NQ + NO_2 &\longleftrightarrow NO + NOQ
\end{aligned}
$$

---
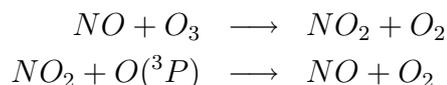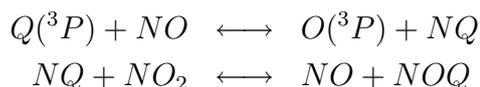
[1] C. Brühl, Max-Plank-Institute for Chemistry, Mainz. The data was given to C. Bechtel, and is reused in this model

[2] Data was given from M. Kaufmann, University of Wuppertal to C. Bechtel

No.	Reaction	A_x	E_x	reference
R60	$NO + O_3 \longrightarrow NO_2 + O_2$	$3.00(-12)$	1500	JPL [2003]
R61	$NO_2 + O(^3P) \longrightarrow NO + O_2$	$5.60(-12)$	-180	JPL [2003]
R70	$Q(^3P) + NO \longleftrightarrow O(^3P) + NQ$	$3.70(-11)$	0	Anderson et al. [1985]
R71	$NQ + NO_2 \longleftrightarrow NO + NOQ$	$3.60(-14)$	0	Klein [1963]

Table 4.1 : *Parameters of the HO_x reactions used in the submodel.*

Details of the reaction coefficients are given in table 4.1. As the concentrations of NO and NO_2 would be changed by reactions R60 and R61, they are resized to their original value every $10^6 s$ during the $10^9 s$ run. Tests have been performed to ensure that these times are sufficient for the determination of equilibrium conditions.

The results of the submodel are shown in figures 4.1 and 4.2; also the isotopic composition of OH and HO_2 from the main model are shown. Comparison of Δ^{17} with the model of Lyons [2001] agrees in the shape of the profile of the anomaly. However, Lyons assumes the anomaly in the asymmetric O_3 to be larger by a factor of ≈ 2 than in the total O_3. His $\Delta^{17}(O_{3,asym})$ has a maximum of $\approx 82‰$, whereas only $50...53‰$ are likely to be encountered in the stratosphere [3]. Therefore, the anomaly modeled by Lyons [2001] for the oxygen containing trace gases is higher than in the model presented here.

4.3 Modeling Isotopic Species

Of all isotopically substituted species, only the ones bearing no more than one rare isotope are implemented into the model (e.g. HDO, but not DDO or HDP). The isotopic substitutes react along the same pathways, but their reaction constants are altered by a fractionation factor. Isotope fractionation factors have not been determined experimentally for all individual reactions and reaction steps, so plausible assumptions have to be made.

For some of the CH_4, CH_2O and H_2 chemical sink reactions fractionation factors are known for deuterium isotopologues. They can be expressed in the form

$$\alpha_x = (A_{\alpha,x} \cdot exp(E_{\alpha,x}/T))^{-1} \qquad (4.2)$$

where $\alpha_x = k_x(D)/k_x(H)$ is the ratio of the isotopically substituted rate constant to the unsubstituted rate constant. Most authors do not quote their fractionation

---

[3]C. Janssen, personal communication
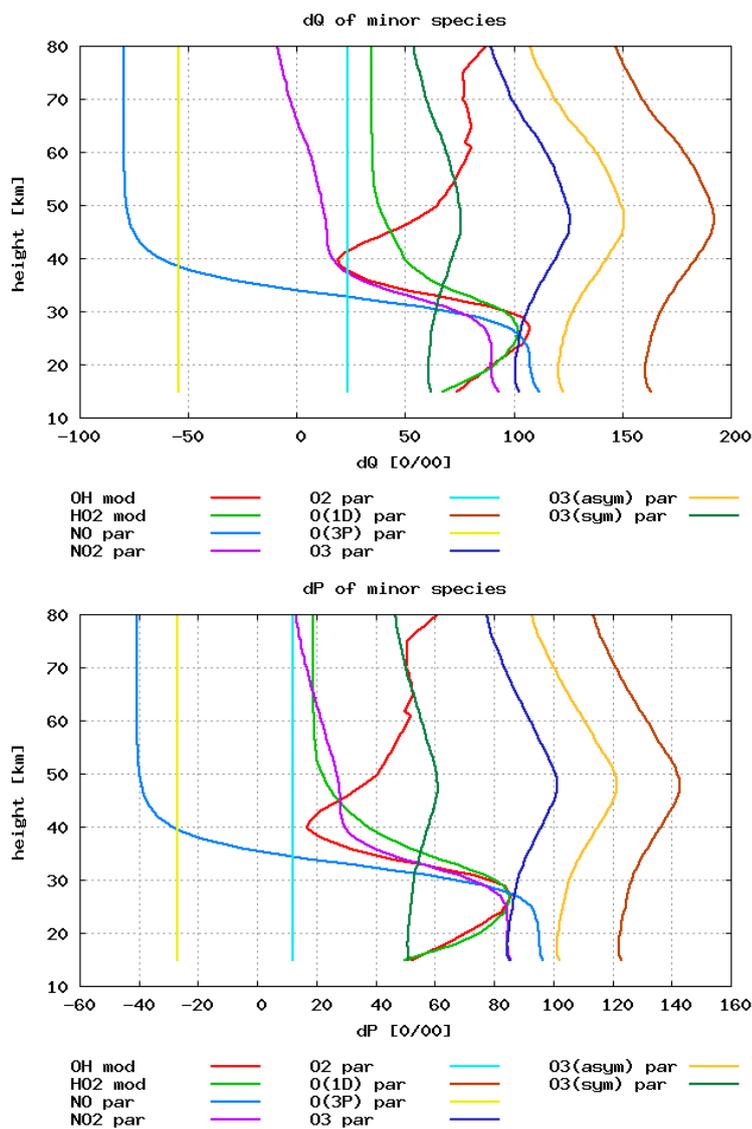
Figure 4.1 : *Oxygen isotopic composition of the minor trace gases involved in the model. OH and HO_2 isotopic compositions are model results, the rest are parameter profiles.*
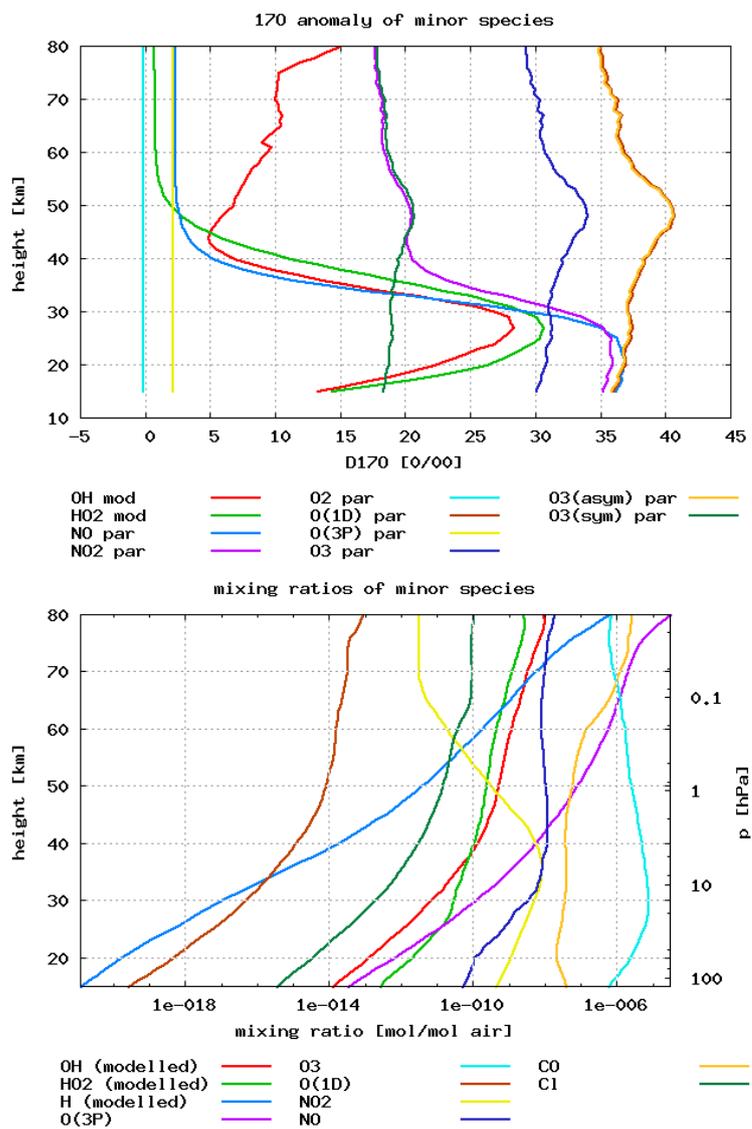
Figure 4.2 : Δ^{17} *(top panel) and the mixing ratios (bottom panel) of the minor trace gases. Note that* Δ^{17} *is calculated with* $\lambda = 0.528$*. This indicates that* $O(^3P)$ *would be MIF, though indeed it is MDF.*
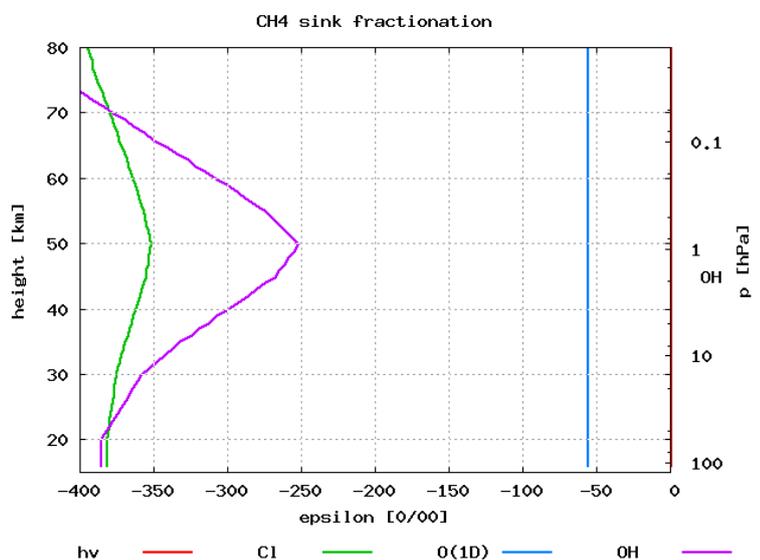
Figure 4.3 : CH_4 *sink fractionations (enhancements in ‰) used in the model. Only for the OH and Cl sinks the temperature-dependence is known. Photodissociation is assumed to proceed without fractionation.*

factors in this form, but give rather absolute values for both substituted and unsubstituted species. However, $A_{\alpha,x}$ and $E_{\alpha,x}$ can be easily calculated.

The following table shows the parameters for the calculation of the fractionation factors and their values at $300K$. An energy $E_{\alpha,x} = 0$ usually indicates that no temperature dependence has been measured so far. Figure 4.3 shows the methane fractionation factors over the range covered by the model.

No.	Reaction	$A_{\alpha,x}$	$E_{\alpha,x}$	$\alpha_x(300K)$	reference
R1	$CH_3D + OH$	0.605	215.00	0.8072	Gierczak et al. [1997]
R1	$CH_4 + OD$	1.120	-55.00	1.0725	Gierczak et al. [1997]
R23	$CH_3D + O(^1D)$	1.060	0.00	0.9434	Saueressig et al. [2001]
R24	$CH_3D + Cl$	1.278	51.31	0.6595	Saueressig et al. [1996]
R4	$HD + OH$	1.100	130.00	0.5894	JPL [2003]
R2	$CHDO + OH$	0.7812	0.00	0.7812	Feinberg et al. [2004]
R2	$CH2Q + OH$	1.0341	0.00	1.0341	Feinberg et al. [2004]
R27	$CHDO + Cl$	0.8326	0.00	0.8326	Feinberg et al. [2004]
R27	$CH2Q + Cl$	0.9259	0.00	0.9259	Feinberg et al. [2004]

In the absence of experimental information about numerous fractionation factors of the photochemical reactions, it is assumed that these reactions add only a mass dependent fractionation to the process, which can be quantified by the

collision frequency. The heavier molecules have a lower collision frequency, and the resulting fractionation factor can be calculated from the reduced masses

$$\alpha = \left(\frac{m_1 \cdot m_2/(m_1 + m_2)}{(m_1 + n_1) \cdot (m_2 + n_2)/(m_1 + n_1 + m_2 + n_2)} \right)^{\frac{1}{2}} \qquad (4.3)$$

where m_1, m_2 are the masses of the reacting molecules, and n_1, n_2 denote the increase in mass when one main isotope is replaced by a rare isotope in the corresponding molecule.

In some cases, isotopic substitutions of both reacting molecules have to be considered. Consider the reaction $OH + O(^3P)$. This reaction can take place with the molecules OH, OD, PH, QH and O, P, Q. Reactions of OD with P and Q are not considered to avoid doubly subsituted products; the same is true for PH, QH and P, Q. However, one is left with reactions of the type $OH + P$ and $PH + O$. The fractionation factors calculated from equation 4.3 are different for these two reactions, which is taken care of by assigning individual fractionation factors for reactions involving hydrogen or oxygen isotopes in both educts.

In the absence of further information, it is assumed that all isotopes react with the same velocity in all photodissociation reactions, so that there is no fractionation in this process.

Another issue is the position dependency in some molecules. For example, in the reaction $H + O_3 \longrightarrow OH + O_2$ it is assumed that only an oxygen atom from the O_3's terminal position can end up in OH. Therefore, the isotopologues OOO, OPO, OQO, OOP and OOQ have different isotopic reaction pathways.

In the cases where there is no position dependency in the molecule, it is assumed that molecules are transferred statistically, if not noted otherwise. Take for example the reaction $CH_4 + O(^1D) \longrightarrow OH + CH_3$, where each hydrogen atom has a probability of $\frac{1}{4}$ to end up in the OH molecule. Therefore, the substitute CH_3D has a probability of $\frac{1}{4}$ to form $OD + CH_3$, and a probability of $\frac{3}{4}$ to form $OH + CH_2D$. However, there are strong indicators that especially in the methane oxidation chain huge deviations from the statistically expected branching ratios can occur (see page 50).

In isotope exchange reactions, both forward and backward reactions have to be calculated. However, authors measuring the rate coefficients for isotope exchange reactions usually only quote one rate constant, assuming $k_x = k_{x,f} = k_{x,b}$. When actually modeling isotopes, such an assumption would lead to no fractionation during the exchange process. Consider the exchange process $QH + NO \longleftrightarrow OH + NQ$. The reaction on the left-hand side should be slower than the one on the right-hand side, as substituting NO by NQ will not change the collision

frequency as much as the substitution OH by QH. Therefore, the case in which Q is in the heavier molecule has been assigned the rate constant k_x in the model, while the other reaction has been given $k_x \cdot \alpha$. α is calculated by applying equation 4.3, changing the bases masses m_1 and m_2 by $n1 = +2$ and $n2 = -2$ simultaneously. As no measured rate constants for P-molecules are available so far, the same scheme has to be applied to that case.

4.4 Photochemical Reactions of the model

The reactions considered in the model are given in table 4.2 (CH_4-decomposition chain), 4.4 (isotope exchange reactions) and 4.3 (all other reactions). Numbering of the reaction rates (RXX) is arbitrary. If not listed otherwise, the reaction rates are taken from JPL [2003].

Most of the reaction constants are given in Arrhenius notation:

$$k_x = A_x \cdot exp\left(-\frac{E_x}{T}\right) \tag{4.4}$$

The termolekular reactions are calculated involving the number density M of the box. Calculation of the reaction constant k_x is performed with the help of the auxiliary variables $k_{0,t}$, $k_{\infty,t}$, y and z [JPL, 2003]:

$$
\begin{aligned}
k_{0,t} &= k_{0,x} \cdot exp(n_x \cdot log_{10}(300/T)) \\
k_{\infty,t} &= k_{\infty,x} \cdot exp(m_x \cdot log_{10}(300/T)) \\
y &= M \cdot k_{0,t}/(1 + (k_{0,t} \cdot M/k_{\infty,t})) \\
z &= 1 + log_{10}(k_{0,t} \cdot M/k_{\infty,t}) \cdot log_{10}(k_{0,t} \cdot M/k_{\infty,t})
\end{aligned}
$$

where $k_{0,x}$, $k_{\infty,x}$, n_x and m_x are rate specific constants. k_x is then calculated as

$$k_x = y \cdot exp(log_{10}(0.6)/z) \tag{4.5}$$

k_x of reactions using the Lindemann-Hinshelwood notation can be calculated using the auxiliary variables a, b and c:

$$
\begin{aligned}
a &= A_{0,x} \cdot exp(E_{0,x}/T) \\
b &= A_{2,x} \cdot exp(E_{2,x}/T) \\
c &= A_{3,x} \cdot exp(E_{3,x}/T)
\end{aligned}
$$

No.	Reaction	A_x	E_x	br
R1	$CH_4 + OH \longrightarrow H_2O + CH_3$	2.45(−12)	1775	
R23(OH)	$CH_4 + O(^1D) \longrightarrow OH + CH_3$	1.50(−10)	0	0.70
R23(H2)	$CH_4 + O(^1D) \longrightarrow CH_2O + H_2$			0.05
R23(H)	$CH_4 + O(^1D) \longrightarrow CH_3O + H$			0.20
R24	$CH_4 + Cl \longrightarrow HCl + CH_3$	9.60(−12)	1360	
R25	$CH_4 + h\nu \longrightarrow H + CH_3$	5.50(−06)	4.40(−19)	
	($h\nu = 121.6nm$, $n_{25} = 0.917$)			
R32	$CH_3 + O_2 + M \longrightarrow CH_3O_2 + M$	see table 4.5		
R50	$CH_3O_2 + NO \longrightarrow CH_3O + NO_2$	2.80(−12)	−300	
R51	$CH_3O + O_2 \longrightarrow CH_2O + HO_2$	3.90(−14)	900	
R2	$CH_2O + OH \longrightarrow H_2O + HCO$	9.00(−12)	0	
R28	$CH_2O + h\nu \longrightarrow H + HCO$	see Jaenicke [1987]		
R52	$CH_2O + h\nu \longrightarrow H_2 + CO$	see Jaenicke [1987]		
R26	$CH_2O + O(^3P) \longrightarrow OH + HCO$	3.40(−11)	1600	
R27	$CH_2O + Cl \longrightarrow HCl + HCO$	8.10(−11)	30	
R29	$HCO + O_2 \longrightarrow HO_2 + CO$	5.20(−12)	0	
R18	$CO + OH \longrightarrow CO_2 + H$	1.50(−13)	0	

Table 4.2 : *Reactions of the CH_4-decomposition chain. Rate R18 has an additional pressure dependency factor $(1 + 0.6 \cdot p/101300Pa)$ in reaction rate coefficient, see JPL [2003]*

$$k_x = a + (c \cdot M)/(1 + c \cdot M/b) \qquad (4.6)$$

where $A_{i,x}$ and $E_{i,x}$ are rate specific.

For photodissociation coefficients not listed otherwise, the standard form to calculate j_x is

$$j_x = A_x \cdot exp(-E_x \cdot exp(n_x \cdot ln(c(z)))) \qquad (4.7)$$

where A_x, E_x and n_x are rate specific, and $c(z)$ is the altitude-dependent air column above the box.

No.	Reaction	A_x	E_x	br
R7	$H_2O + O(^1D) \longrightarrow 2 \cdot OH$	2.20(−10)	0	
R30	$H_2O + h\nu \longrightarrow OH + H$	5.25(−06)	4.40(−19)	
	($h\nu = 121.6nm$, $n_{30} = 0.917$)			
R31	$H_2O + h\nu \longrightarrow OH + H$	1.20(−06)	1.00(−07)	
	(Schumann-Runge, $n_{31} = 0.35$)			
R4	$H_2 + OH \longrightarrow H2O + H$	5.50(−12)	2000	
R41	$H_2 + O(^1D) \longrightarrow OH + H$	1.10(−10)	0	
R42	$H_2 + Cl \longrightarrow HCl + H$	2.60(−12)	350	
R10	$H + O_3 \longrightarrow OH + 2 \cdot O_2$	1.40(−10)	470	
R15	$H + O_2 + M \longrightarrow HO_2 + M$	see table 4.5		
R34(OH)	$H + HO_2 \longrightarrow 2 \cdot OH$	8.10(−11)	0	0.87
R34(H2O)	$H + HO_2 \longrightarrow 2 \cdot H_2O + O(^3P)$			0.02
R34(H2)	$H + HO_2 \longrightarrow 2 \cdot H_2 + O_2$			0.09
R3	$OH + HO_2 \longrightarrow H_2O + O_2$	4.80(−11)	−250	
R5	$OH + OH \longrightarrow H_2O + O(^3P)$	4.20(−12)	240	
R14	$OH + O_3 \longrightarrow HO_2 + O_2$	1.70(−12)	940	
R18	$OH + CO \longrightarrow CO_2 + H$	1.50(−13)	0	
R19	$OH + O(^3P) \longrightarrow O_2 + H$	2.20(−11)	−120	
R20	$OH + NO_2 + M \longrightarrow HNO_3 + M$	see table 4.5		
R40	$OH + HNO_3 \longrightarrow H_2O + NO_3$	$A_0 = 2.40(−14)$	$E_0 = 460$	
	(Lindemann-Hinshelwood)	$A_2 = 2.70(−17)$	$E_2 = 2199$	
		$A_3 = 6.50(−34)$	$E_3 = 1335$	
R43	$OH + HCl \longrightarrow H_2O + Cl$	2.60(−12)	350	
R6	$HO_2 + NO \longrightarrow NO_2 + OH$	3.50(−12)	−250	
R8	$HO_2 + O(^3P) \longrightarrow OH + O_2$	2.20(−10)	0	
R9	$HO_2 + O_3 \longrightarrow OH + 2 \cdot O_2$	1.00(−14)	490	

Table 4.3 : *Other reactions involving oxygen and hydrogen molecules.*

4.5 Model Results

4.5.1 Mixing Ratios

In figure 4.4 the modeled mixing ratios are plotted versus altitude. For comparison, measurements of Zoeger et al. [1999] and Michelsen et al. [2002] are included in the plot. Agreement between measured and modeled data is very good at heights below $70km$. Above $70km$, where photodissociation of H_2O increases sharply, Michelsen et al. [2002] measure a sharp decrease in the H_2O-mixing ratio in southern mid-latitudes. However, in their measurements at northern mid-latitudes, Michelsen et al. [2002] find a lesser decrease. Modeling the

No.	Reaction	A_x	E_x	reference
R21	$QH + NO \longleftrightarrow OH + NQ$	$1.80(-11)$	0	Dubey et al. [1997]
R22	$QH + H_2O \longleftrightarrow OH + H_2Q$	$2.30(-13)$	2100	Dubey et al. [1997]
R37	$QH + O_2 \longleftrightarrow OH + OQ$	$< 1.00(-17)$	0	Greenblatt and Howard [1989]
R38	$HOQ + O_2 \longleftrightarrow HO_2 + OQ$	$< 3.00(-17)$	0	Sinha et al. [1987]
R39	$HOQ + OH \longleftrightarrow HO_2 + QH$	$1.70(-11)$	-400	Dransfeld and Wagner [1987]
R54	$QH + NO_2 \longleftrightarrow OH + NOQ$	$1.00(-11)$	0	Greenblatt and Howard [1989]
R55	$NOQ + H_2O \longleftrightarrow NO_2 + H_2Q$	$2.30(-13)$	2100	Jaffe and Klein [1966]

Table 4.4 : *Oxygen isotope exchange reactions considered in the model. Rates R38, R39 and R55 are analyzed separately in the model, as the rate coefficients are only an estimated upper limit. R55 is estimated from R22.*

No.	Reaction	k_0	k_∞	n	m
R15	$H + O_2 + M \longrightarrow HO_2 + M$	$5.70(-32)$	$7.50(-11)$	1.6	0
R20	$OH + NO_2 + M \longrightarrow HNO_3 + M$	$2.00(-30)$	$2.50(-11)$	3.0	0
R32	$CH_3 + O_2 + M \longrightarrow CH_3O_2 + M$	$4.50(-31)$	$1.80(-12)$	3.0	1.7

Table 4.5 : *Parameters of the termolecular rates.*

photodissociation of the various species will therefore remain a complicated task. For the stratosphere, where most of the chemistry involving H_2O happens, photodissociation is only relevant for CH_2O.

The mixing ratio of CH_4 decreases from $1.7ppm$ in the lowermost box to $\approx 0.17ppm$ in the mesosphere. The H-atoms are transferred to H_2O; H_2 is known to remain nearly constant at $0.50...0.55ppm$ in the stratosphere. This does not mean that H_2 does not participate in the chemistry of the stratosphere, but rather that its sources and sinks balance. In the top $10km$ of the model, the photodissociation of water vapor increases the amount of H_2 molecules.

As a test for the numerical stability of the model, the total potential hydrogen $S = H_2O + H_2 + 2 \cdot CH_4$ is calculated for all boxes; it changes only slightly from $7.650ppm$ in the lowermost box to $7.644ppm$ in the top box. This ensures no hydrogen is lost in the model, keeping in mind that a small amount is transferred to other hydrogen bearing molecules.

4.5.2 Photochemical Lifetimes

Figure 4.5 shows the photochemical lifetimes τ of H_2O, CH_4, H_2 and CH_2O. τ can be calculated in equilibrium by division of the molecule's concentration by the sum of its sources (P_i) or sinks (L_i):
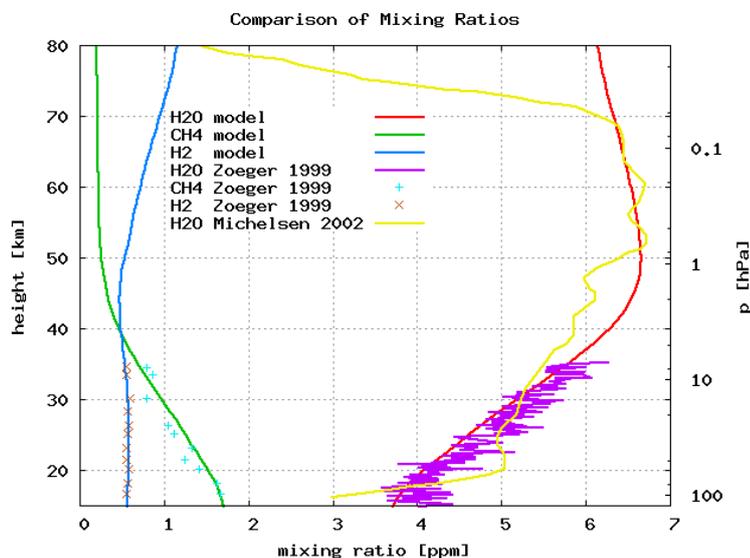
Figure 4.4 : *Modeled and measured mixing ratios. The modeled mixing ratios agree quite well with the measured ones; only the sharp decrease in H_2O at heights above $70km$ as measured by Michelsen et al. [2002] in the southern hemisphere is not reproduced by the model.*

$$\tau_X = \frac{[X]}{P_1 + P_2 + ... + P_n} = \frac{[X]}{L_1 + L_2 + ... + L_n} \qquad (4.8)$$

The photochemical lifetimes can be compared to the typical transport time $\tau_{tp} = H^2/K_z$, where $H = R \cdot T/(M_{air} \cdot g)$ is the local scale height. As can be seen in figure 4.5, the photochemical lifetimes of H_2O, CH_4 and H_2 are higher than the transport time throughout all modeled heights. Therefore their inclusion into the model's transport equations is necessary; on the other hand the same is true for the exclusion of CH_2O and other short lived species, as they are faster destroyed than transported.

Figure 4.6 shows the production and loss rates of H_2O. For comparison, $2 \cdot L(CH_4)$ is also plotted. The production maximum of H_2O is some km higher than the maximum of the methane loss rate. This shows that most of the H-atoms stemming from the CH_4-decomposition chain first are incorporated into intermediate species before ending up in H_2O. The transport of the remaining methane is enhanced over that of water vapor due to a stronger vertical gradient, while the short-lived species of the methane oxidation chain remain in the same box of the model and form water molecules. Therefore, the vertical displacement of maximum CH_4 loss is somewhat higher than that of H_2O formation.
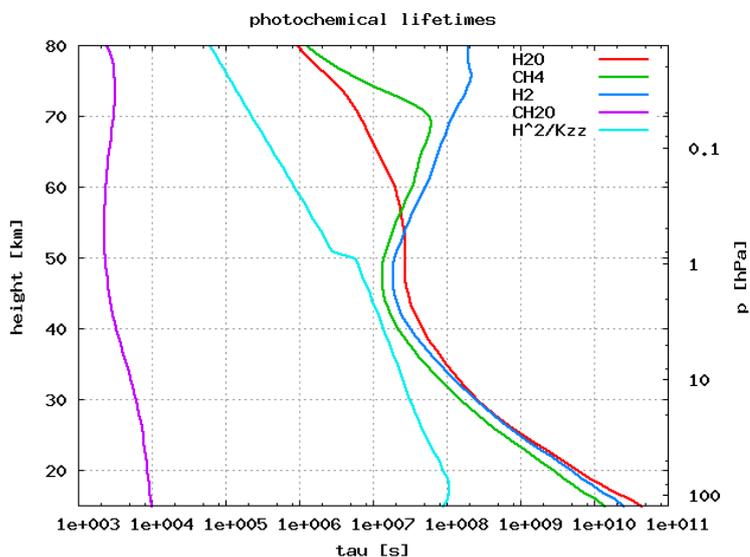
Figure 4.5 : *Modeled lifetimes of the most important trace gases. For comparison, also the typical transport time H^2/K_z is shown. As the lifetime of CH_2O is smaller than the transport time, it is not to included in the model's transport scheme.*
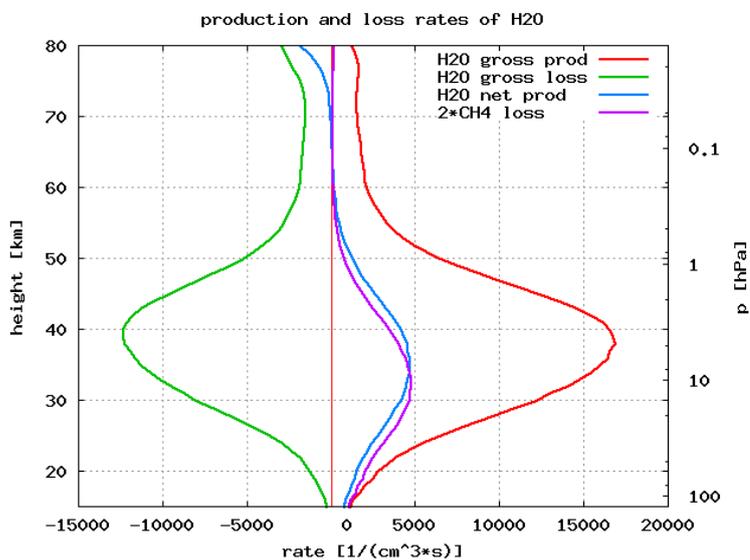
Figure 4.6 : *Modeled production and loss rates of H_2O. For comparison, also $2 \cdot L(CH_4)$ is plotted. The H_2O production maximum is some km higher than the maximum of CH_4-loss, which shows most of the H-atoms are first incorporated into intermediate species before ending up in H_2O.*
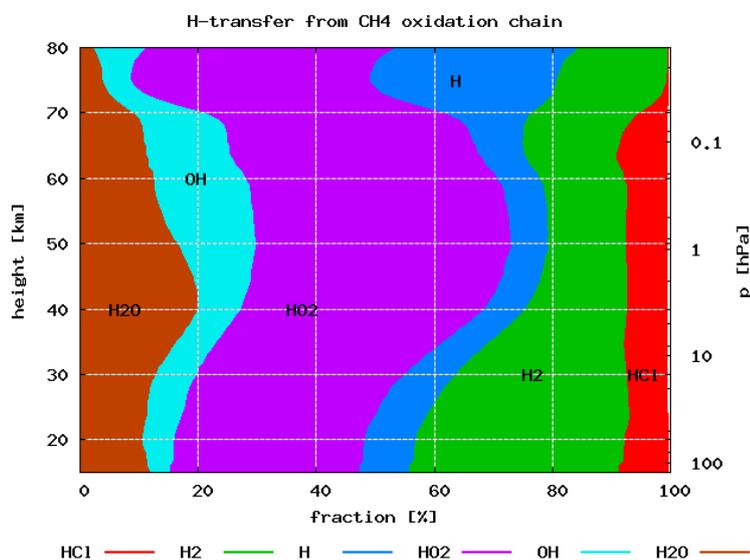
Figure 4.7 : *Fraction of the H-atoms stemming from the CH_4-oxidation chain that are incorporated into the various minor trace gases. Less than 20% of all H-atoms are directly built into H_2O-molecules, while the majority takes a detour via the HO_x-family, H_2 and HCl.*

4.5.3 Hydrogen Isotopic Composition

Figure 4.7 shows the the fraction of H-atoms stemming from the CH_4-oxidation chain incorporated into the products H_2O, OH, HO_2, H, H_2 and HCl. Only a small fraction - less than 20% - of the H-atoms is directly transfered into H_2O. The vast majority of H-atoms makes a detour via the HO_x family or the longer-lived trace gases H_2 and HCl.

Figure 4.8 allows to investigate where the H-atoms in freshly produced H_2O come from. Clearly, the reactions of type $OH + HX \longrightarrow H_2O + X$ dominate the production of water. As only one of the two hydrogen atoms of H_2O stems from OH, the hydrogen input maximum by OH is 50%. Below $70km$, only a tiny fraction of H_2O stems from the only source not involving OH, $H + HO_2 \longrightarrow H_2O + O(^3P)$. Only above $70km$, this reaction gains importance due to the increased amount of H-radicals stemming from photodissociation processes.

The other three important sources for the H-atoms in the produced water in the stratosphere are HNO_3, HO_2 and CH_4. Especially HO_2 gains importance in the upper stratosphere and throughout the mesosphere.

Figure 4.9 shows the modeled isotopic hydrogen composition of H_2O, CH_4 and
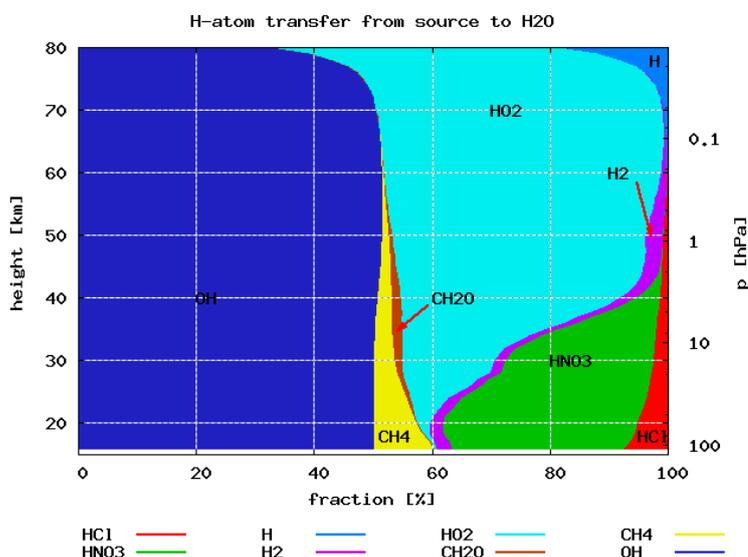
Figure 4.8 : *Fraction of the H-atoms in H_2O stemming from the various sources. Clearly, OH and HO_2 dominate the picture. The reaction $H + HO_2 \longrightarrow H_2O + O(^3P)$ gains importance above $70km$.*

H_2. Also, δD of freshly produced water as calculated from the local sources of H_2O and HDO is displayed. The isotopic composition of the in-situ produced water parallels the one of CH_4 in the stratosphere, as the fraction of the OH, $O(^1D)$ and Cl sinks remains roughly constant in that region (see figure 4.10). In the lower mesosphere, the hydrogen atoms stem from HO_2 instead of CH_4 and HNO_3, so that the isotopic difference between the produced water and methane changes. Above $70km$, the influence of the photodissociation is visible, which proceeds without fractionation in the model.

Figure 4.9 includes CH_4 isotope data obtained from a stratospheric balloon flight[4]. Methane is known to have a small seasonal cycle, and one can not assume to get a perfect fit between the model and a single dataset, as the tropospheric concentration, initial isotopic composition and oxidation mechanisms may change during its cycle and latitudinal changes in its oxidation chemistry. In figure 4.11, δD of methane is plotted versus the remaining fraction. Fitting the data onto a Rayleigh function (see equation 2.30), an average fractionation $\epsilon = -120‰$ and $\epsilon = -121‰$ is obtained for the data of Brass and Rice et al. [2003], respectively. The model results in a somewhat smaller $\epsilon = -150‰$. Comparing these results to the individual fractionations of the four decomposition pathways of methane

---

[4]data not yet published, courtesy of Marc Brass
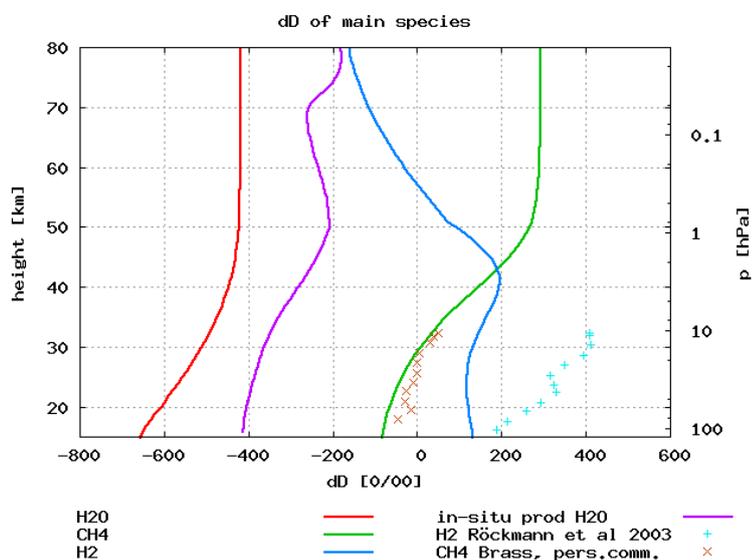
Figure 4.9 : δD of the main hydrogen bearing species H_2O, CH_4 and H_2. Also, the isotopic composition of in-situ produced water is shown. For comparison, data from two stratospheric balloon flights (Brass, personal communication, and Röckmann et al. [2003]) is included.
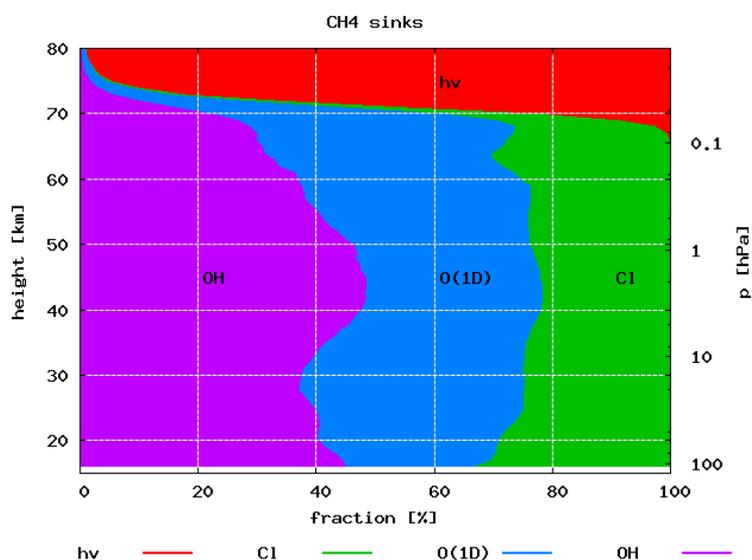
Figure 4.10 : Relative fractions of the 4 methane sink reactions. Photodissociation only plays a role above $70km$, whereas the influence of the OH, Cl and $O(^1D)$ sinks remains roughly constant below $70km$.
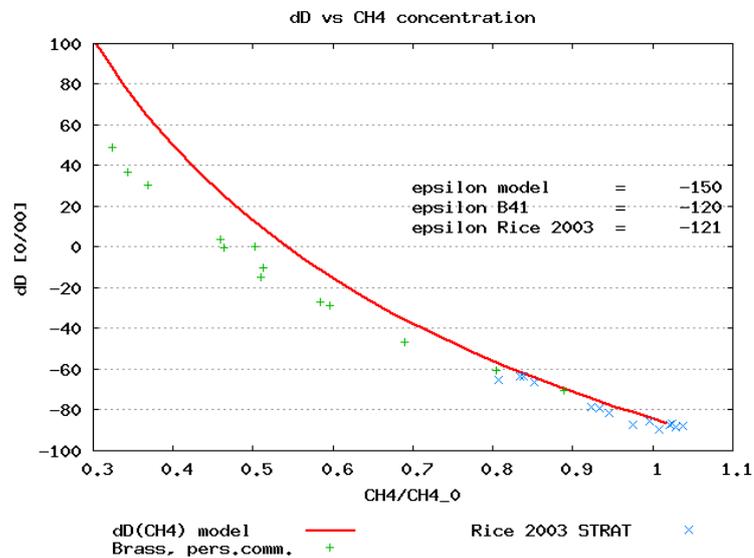
Figure 4.11 : *The Rayleigh-plot shows a difference between the modeled and measured data which could be explained by an underestimated $O(^1D)$-sink in the model.*

(figure 4.3) leads to the conclusion that the data obtained from Brass and Rice et al. [2003] are stronger influenced by the $O(^1D)$-sink than predicted by the model, or that mixing is underestimated.

δD of H_2O increases with height due to water produced from the CH_4 oxidation. Above $50 km$, virtually no change can be seen, as almost all CH_4 has been destroyed on its way into the mesosphere. As total hydrogen is conserved, there can be only exchange between the two major reservoirs H_2O and H_2 via decomposition and recombination. As there is approximately four to five times more H_2O than H_2, any change in the isotopic composition of H_2O will be enhanced by that factor in H_2.

In figure 4.12, the modeled HDO is compared to stratospheric measurements [Johnson et al., 2001b, Dinelli et al., 1991, Rinsland et al., 1991, Stowasser et al., 1999]. There is agreement with all measurements except Stowasser et al. [1999], which were taken at high northern latitudes and are thought to be influenced by the sedimentation of PSC particles.

In the model, δD of H_2 does not change much in the stratosphere, before getting depleted in the mesosphere. This is contradicted by recent measurements [Rahn et al., 2003, Röckmann et al., 2003], which show a very strong enhancement of several hundred ‰ in the stratosphere. Data from a balloon-borne airsampler [Röckmann et al., 2003] is included in figure 4.9; δD of H_2 increases in the
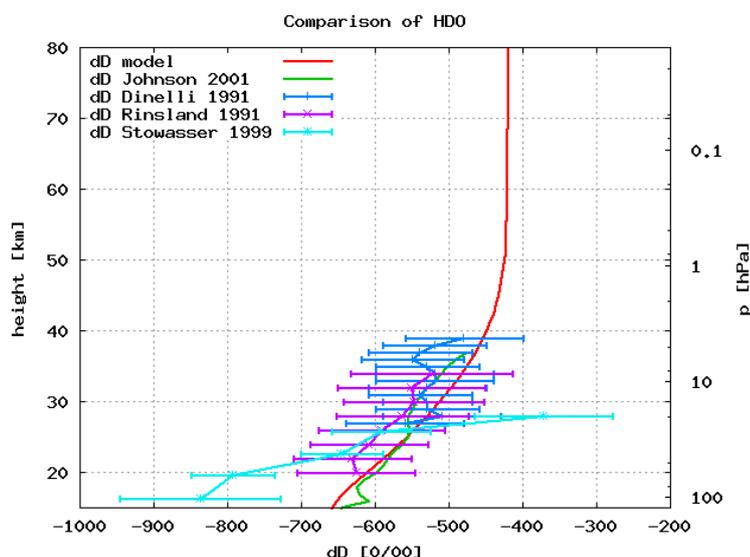
Figure 4.12 : *Modeled and measured δD of H_2O. The agreement between model and measurements is excellent except for Stowasser et al. [1999], though this dataset is not really representative as it was taken at high northern latitudes under the influence of PSC particle sedimentation.*

stratosphere to $\approx 450‰$. It is not well understood how this extreme enrichment is implemented into H_2, as the following discussion will show.

In figure 4.13 the fraction of H-atoms incorporated into freshly produced H_2 is shown. The main source is the photodissociation of CH_2O up to $55km$; above that level the reaction $HO_2 + H$ becomes dominant. Figure 4.14 shows the fractions of the three H_2-sinks OH, $O(^1D)$ and Cl. Roughly 60% of H_2 is destroyed in the reaction with OH, 35% by $O(^1D)$ and the rest by Cl.

In figure 4.15, the isotopic composition of the sinks and sources of H_2 are investigated. Freshly produced H_2 starts at $\approx -380‰$ above the tropopause, which is a result of the strong fractionation in the CH_4 oxidation by Cl and OH. Decomposition of methane by these two reactants totals about 75% with a fractionation of $\approx -380‰$, while the other 25% react with $O(^1D)$ with a fractionation of $\approx -55‰$. Together with the stratospheric input value of $\delta D = -86‰$ for methane, the $-380‰$ freshly produced H_2 can be explained. Due to Rayleigh fractionation in CH_4 decomposition, the isotopic composition of H_2 produced enriches with increasing altitude. At $\approx 50km$, the molecular hydrogen source changes from CH_4 decomposition to $HO_2 + H$, leading to a further depletion of the H_2 source with altitude.
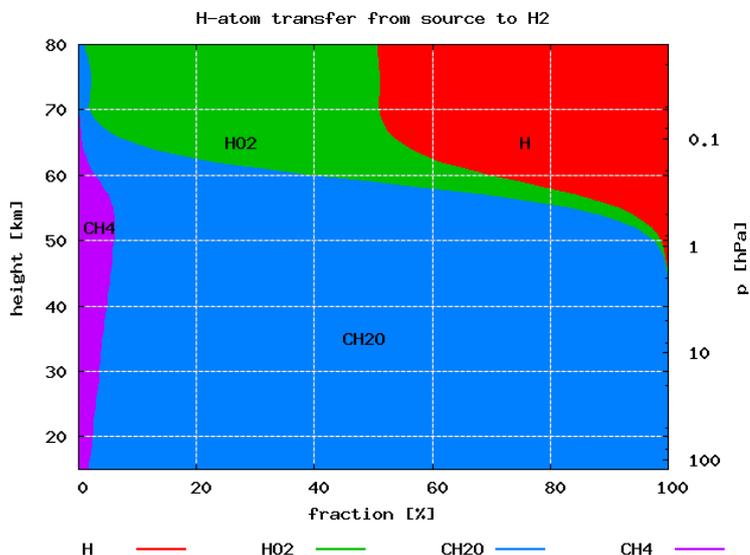
Figure 4.13 : *Sources of the H-atoms in produced H_2. The dominant source below $55km$ is the photodissociation of CH_2O. Above that level the reaction $HO_2 + H$ becomes the main source.*
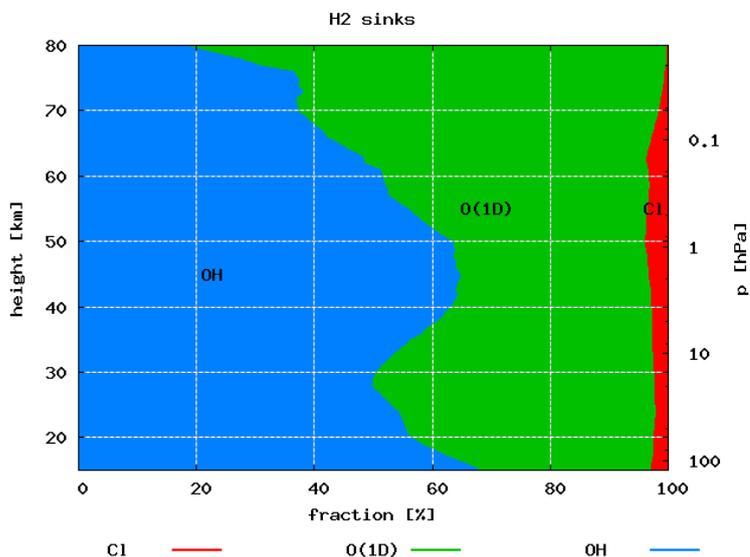
Figure 4.14 : *Fractions of the H_2 sinks. Cl plays only a minor role; about 60% of H_2 is destroyed via OH, 35% via $O(^1D)$.*
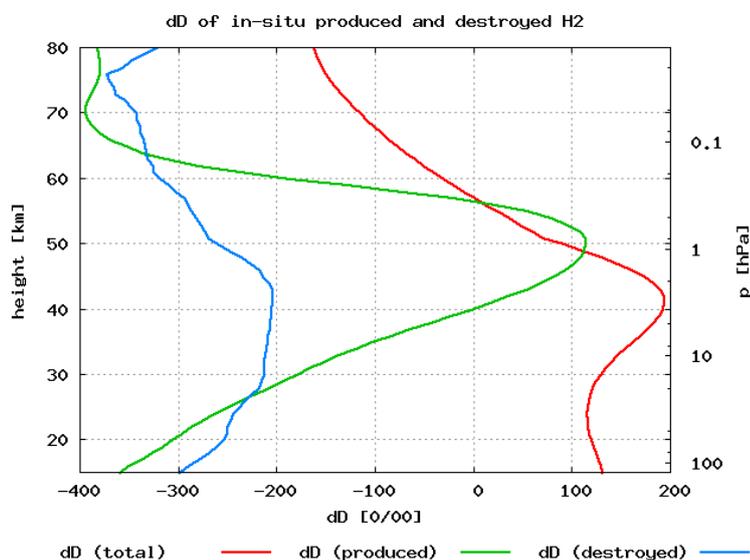
Figure 4.15 : *Modeled isotopic composition of H_2, with both δ-values for in-situ produced and decomposed H_2 shown. The increase of δD of H_2 near the stratopause could be a sink effect, as the H_2 mixing ratio decreases slightly in this area (see figure 4.4).*

In the model the relative fraction of the sinks OH and $O(^1D)$ varies, and the fractionation factor of $HD + OH$ has a temperature dependency. Therefore, the behavior of the sinks does not parallel the isotopic composition of H_2.

The extreme enrichment in measured H_2 could be due to additional fractionation occurring in

1. CH_4 oxidation

2. photolysis of CH_2O

3. sink effects in either OH, $O(^1D)$ or Cl

4. oxidation of precursors of CH_2O

The first possibility, CH_4 oxidation, can be ruled out quite easily. The enrichment in H_2 would deplete the remaining methane severely, an effect that is not seen in the CH_4-data.

To test the photolysis of CH_2O, the fractionation factor of $CHDO$ was increased from 1.0 to 5.0. This resulted in $\delta D(H_2)$ similar to the observed values, but such an extreme fractionation seems to be very unlikely.

Interestingly, the small modeled maximum in $\delta D(H_2)$ could be effect of the sink reactions. As shown in figure 4.15, both produced and destroyed H_2 are isotopically depleted with respect to the H_2 present. The resulting δD-maximum is therefore due to a slight imbalance in the H_2-budget, so that H_2 has a small net sink at this height. Thus studying the sink reactions of H_2 might prove interesting for the solution of the heavy-hydrogen puzzle, though it may not be the dominant effect.

During the oxidation of the CH_2O precursors, the branching ratios could add additional fractionation. For example, the reaction $CH_3D + OH$ is statistically expected to yield 25% $CH_3 + HDO$, and 75% $CH_2D + H_2O$. Deviations from this statistical expected value can lead to fractionation; especially in the first oxidation step of CH_4 an additional fractionation in the branching ratio is expected. Gierczak et al. [1997] have studied the reaction $CH_4 + OH$ with deuterated methanes. They see an increase in the kinetic isotope effect with every substituted hydrogen atom, so that the fractionation is largest for CD_4. It appears that almost no deuterium bond with the carbon is broken, so that only hydrogen atoms are released in the initial methane oxidation step. This is verified by the fractions of the reaction rates given by Gierczak et al. [1997] :

$$\frac{k(CH_3D)}{k(CH_4)} = 0.74$$

$$\frac{k(CH_2D_2)}{k(CH_4)} = 0.52$$

$$\frac{k(CHD_3)}{k(CH_4)} = 0.28$$

$$\frac{k(CD_4)}{k(CH_4)} = 0.12$$

As the numbers show, the reactions rates are almost linearly related to the number of hydrogen atoms in the methane molecule, so that about 96% of $CH_3D + OH$ produces $CH_2D + H_2O$ [Gerst and Quay, 2001]. A model run was performed in which this reaction was set to 100%, but the resulting δD of H_2 is still too low by $\approx 200...300\%_0$ to explain atmospheric observations. However, if also in the second abstraction step $CH_3O + O_2 \longrightarrow CH_2O + HO_2$ all deuterium atoms are left in the formaldehyde, a match between the observed and modeled δD can be found. The isotopic composition of the sources and sinks of this model run are shown in figure 4.16. δD of molecular hydrogen rises to a maximum of $600\%_0$, which is in agreement with the maximum enrichments found in the
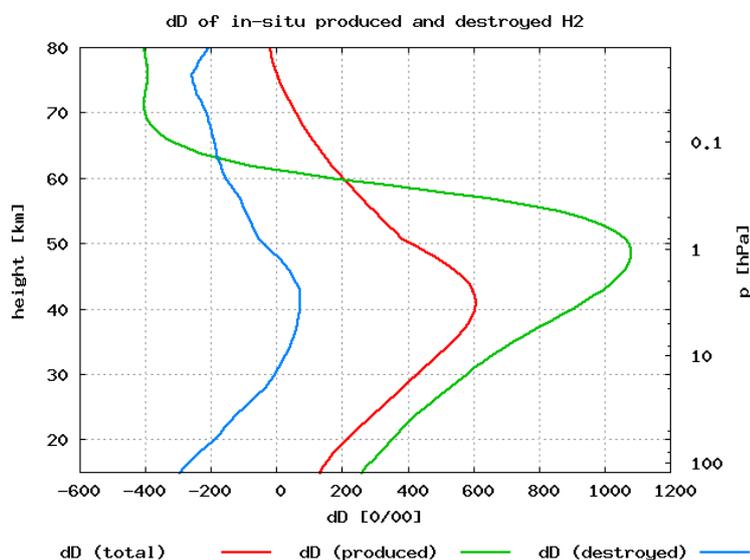
Figure 4.16 : *Model isotopic composition of H_2. In this model run it was assumed that all deuterium is left in the methane oxidation chain, and finally ends up in CH_2O prior to photolysis.*

stratosphere[5].

That all deuterium is left in the methane oxidation chain is pure speculation, and has not been verified so far. However, as the data of Gierczak et al. [1997] see such huge preference in the abstraction of hydrogen, it surely is an effect that should be further investigated. It is also an effect that will change the isotopic composition of water vapor. As molecular hydrogen is getting isotopically heavier than in the base model by $\approx 400\%_0$, water vapor will undergo an additional depletion of $\approx 40\%_0$.

4.5.4   Oxygen Isotopic Composition

One of the greatest obstacles in modeling the oxygen composition of water vapor is that only few of the many fractionation factors needed have been measured so far. Therefore, the remaining fractionation factors are calculated from the changed collision frequency (equation 4.3).

Additionally, oxygen bearing species are known to exchange isotopes. These exchange reactions can be fast compared to chemical reactions, thus the results

---

[5]Thomas Röckmann, personal communication
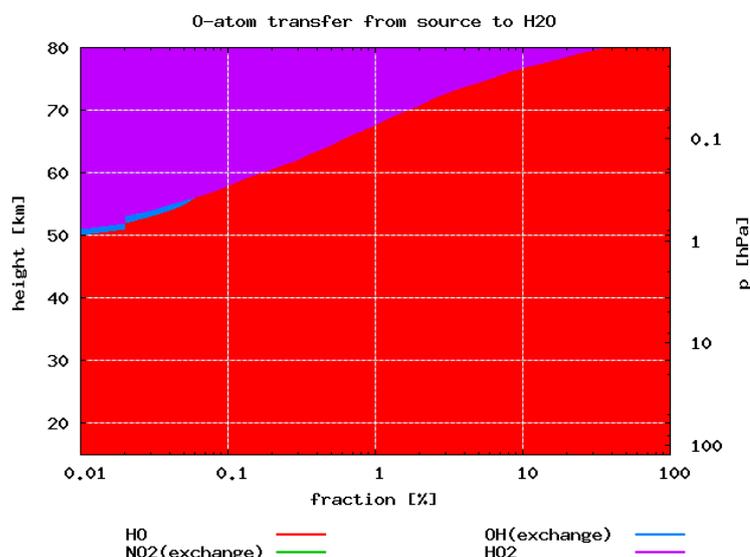
Figure 4.17 : *Modeled fractions of the sources of H_2O in the middle atmosphere. The reactions that form H_2O from OH clearly dominates the picture below $60km$ by more than 99%. HO_2 gains importance above $60km$. The exchange reactions of type $OH + H_2Q$ are negligibly small; exchange with NO_2 is not included in the base model.*

of a model depend to a large portion on assumptions about the exchange rates. Unfortunately, the exchange rates of $QH + O_2 \longleftrightarrow OH + OQ$ (R37), $HOQ + O_2 \longleftrightarrow HO_2 + OQ$ (R38) and $NOQ + H_2O \longleftrightarrow NO_2 + H_2Q$ (R55) are presently not known. Here, the estimates from Lyons [2001] are used. The mentioned exchange reactions are set to zero in the base model, and turned on to their estimated upper limit in sensitivity studies.

Water vapor is formed in the middle atmosphere almost exclusively by reaction of OH with H-bearing species (R1, R2, R3, R4, R5, R40, R43). Only above $60km$, the reaction $H + HO2$ (R34) gains importance. This is demonstrated in figure 4.17, which also shows the fraction of H_2O molecules formed in isotope exchange reactions with OH (exchange with NO_2 is zero in the base model).

Due to this dominance of OH and HO_2 in the formation of H_2O in the middle atmosphere, it is necessary to analyze the formation of OH-bonds in order to investigate the isotopic composition of in-situ produced water vapor.

One can distinguish between 5 different types of OH-bonds formed:

1. OH-bonds formed by reaction with molecular oxygen (MDF)

2. OH-bonds formed by reaction with ozone (MIF)

3. OH-bonds formed by reaction with $O(^1D)$. As $O(^1D)$ is formed during ozone decomposition, it also carries the MIF-signature of ozone, most likely from the terminal O-atom (asymmetric O_3)

4. OH-bonds formed by isotopic exchange with NO_x. As the isotopic composition of NO_x is determined in reactions with both the MIF-ozone and the MDF-oxygen reservoir, it also carries a MIF-signature.

5. OH-bonds formed by reaction with $O(^3P)$. Due to rapid exchange between $O(^3P)$ and O_2, these OH-bonds carry MDF-signature, but are depleted with respect to O_2 (note that the $\approx 2‰$ anomaly of $O(^3P)$ shown in figure 4.2 is only due to the difference in λ for O_2 and H_2O).

The fractions of these five reservoirs contributing to the formation of new OH-bonds are shown in figure 4.18; the contribution from $O(^3P)$ is negligibly small. In the stratosphere, up to $\approx 80\%$ of the OH-bonds are formed via the MIF-signature bearing compounds $O(^1D)$ and NO_x; the direct reaction with ozone is only important in the mesosphere. A plot of Δ^{17} (figure 4.19) confirms that indeed the maximum of the anomaly coincides with the maximum OH-production from the $O(^1D)$ and NO_x reservoirs.

MIF is therefore introduced into H_2O dominantly in a three-step process: First, the Δ^{17}-anomaly is transfered to $O(^1D)$ by O_3 photolysis, and to NO_x via $NO + O_3 \longrightarrow NO_2 + O_2$. From these reservoirs the anomaly is transfered to OH_x via the isotopic exchange reactions $QH + NO$ and $QH + NO_2$, or via the reactions $CH_4 + O(^1D)$ and $H_2O + O(^1D)$. Finally, by H-abstraction, the MIF is transfered into H_2O.

Effectively all OH-bonds formed are enriched in ^{17}O and ^{18}O with respect to VSMOW, as all four major reservoirs O_2, O_3, $O(^1D)$ and NO_x have $\delta^{17}O > 0$, $\delta^{18}O > 0$. Therefore, freshly formed H_2O is also isotopically enriched versus VSMOW (figure 4.20). The resulting total H_2O is therefore also enhanced versus its original entry value at the tropopause (figure 4.21), i.e. water gets progressively enriched in oxygen isotopes as it ascends in the stratosphere.

4.5.5 The Influence of the Unknown Oxygen Exchange Reactions

As mentioned above, the influence of the oxygen exchange rates $HO_2 + O_2$ (R38), $OH + O_2$ (R37) and $NO_2 + H_2O$ (R55) can only be estimated, as the
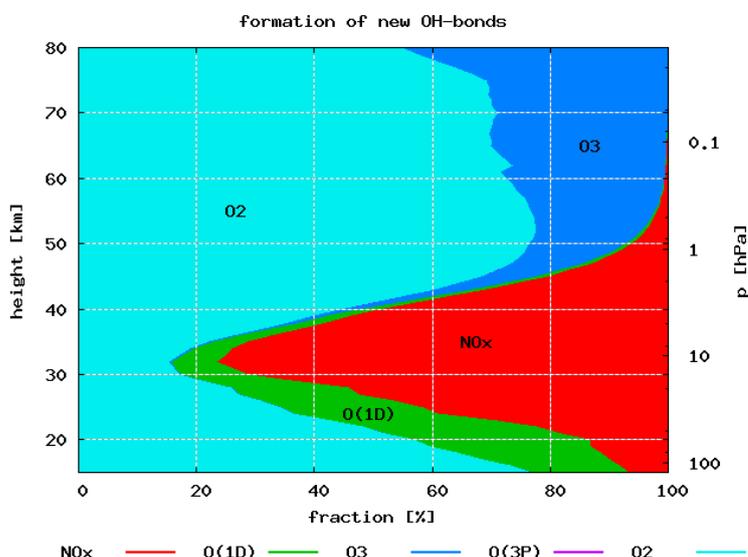
Figure 4.18 : *Fractions of freshly formed OH-bonds from the different oxygen reservoirs. In the stratosphere, most of the OH-bonds are formed from the MIF-bearing reservoirs $O(^1D)$ and NO_x. The ozone reservoir (MIF) plays only a role in the mesosphere, while $O(^3P)$ can be neglected.*

exchange rates have not been determined experimentally. The parameters given in table 4.4 for R37 and R38 are for the estimated upper limits [Greenblatt and Howard, 1989, Sinha et al., 1987]. For R55, it is assumed that the exchange $NOQ + H_2O$ proceeds at the same speed as $QH + H_2O$ (R22). The results of setting the unknown rates to these values are shown in figures 4.19 and 4.21.

It can be seen that the total oxygen isotopic composition of water vapor does not change much by switching R37, R38 on. The influence of O_2 on freshly formed OH-bonds is now stronger than in the base model, which leads to a slight depletion, as O_2 is less enriched than NO_x. On the other hand, the Δ^{17}-anomaly in H_2O now vanishes, as the exchange with MDF O_2 diminishes the anomaly in OH_x. That the anomaly shown in figure 4.19 goes to negative values is due to different choices of the 3-isotope exponent λ for different processes. While by definition of Δ^{17}-anomaly in equation 2.27 a $\lambda = 0.528$ for water vapor is assumed, $\lambda = 0.507$ for O_2 or $\lambda = 0.513$ for H_2O in kinetic fractionation (see section 2.3.5). This leads to the negative Δ^{17} values seen in figure 4.19, although no real anomalous fractionation is involved.

When R55 is switched on at its maximum value, the isotopic range of H_2O changes dramatically (figure 4.21). This also leads to a large oxygen isotope
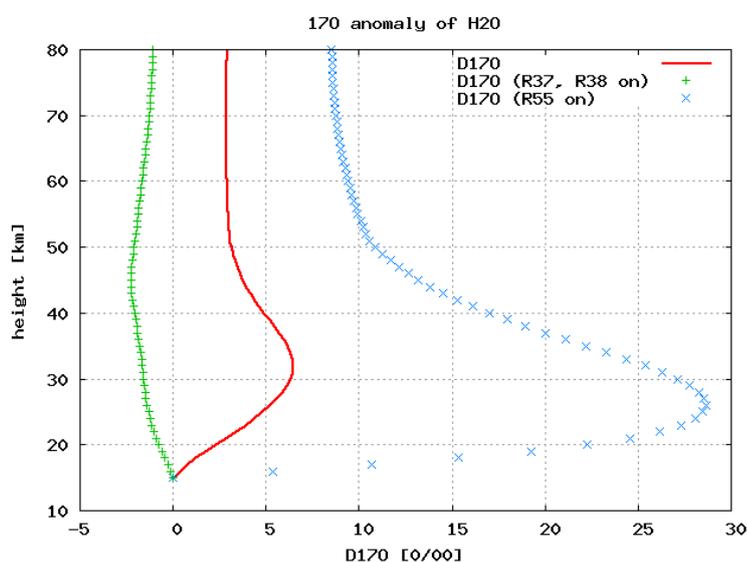
Figure 4.19 : Δ^{17} *of* H_2O. *The maximum of the anomaly coincides with the* OH-*production maximum from* $O(^1D)$ *and* NO_x *(see figure 4.18). When switching the exchange rates with* O_2 *(R37, R38) on, the anomaly basically vanishes - the remaining negative anomaly is due to different* λ*s in reaction rates. Exchange with* NO_2 *(R55) could be an effective way of producing the anomaly in* H_2O*, as explained in the text.*
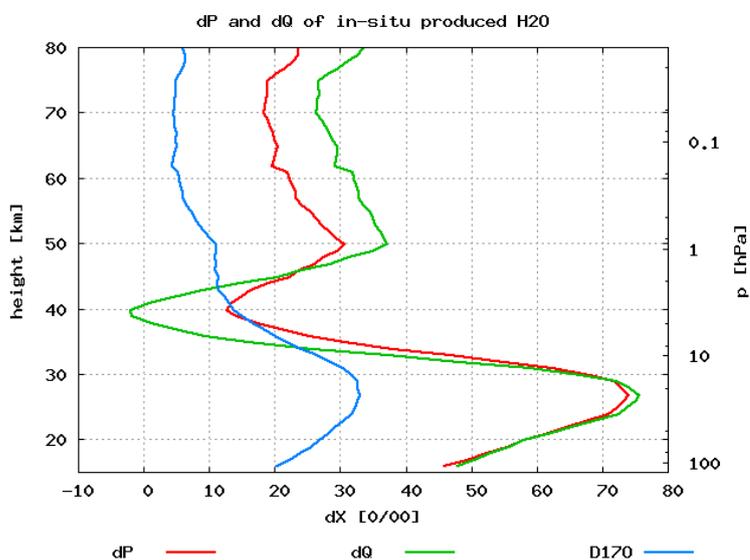
Figure 4.20 : $\delta^{17}O$, $\delta^{18}O$ and Δ^{17} of in-situ produced water. As effectively all OH-bonds formed are enhanced versus VSMOW, so is the resulting H_2O. The maximum of the anomaly is produced at $\approx 27km$.
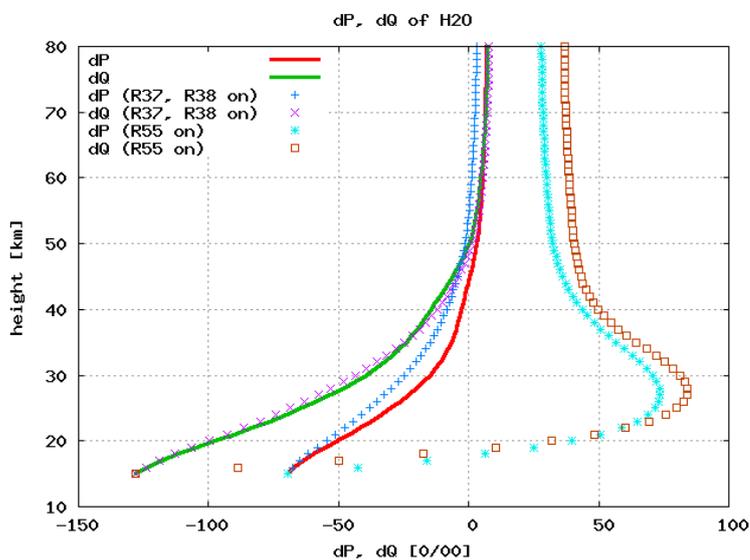
Figure 4.21 : $\delta^{17}O$ and $\delta^{18}O$ of total water. Water vapor gets enhanced in the middle atmosphere with respect to its initial entry value at the tropopause due to in-situ produced water with $\delta^{17}O > 0$, $\delta^{18}O > 0$ (figure 4.20). Also shown are the effects of switching R37, R38 (exchange with O_2) or R55 (exchange with NO_2) on.

anomaly. One actually has to be cautious, because NO_2 is kept as a fixed parameter in this model, and its isotopic composition was derived under the assumption that this exchange rate is zero. As the concentration of H_2O is approximately $500 - 5000$ times higher in the stratosphere than that of NO_2, the anomaly in NO_2 could be dampened by this exchange reaction. It is therefore important to investigate which effect - the transfer of MIF into NO_2 by ozone decomposition (R60), or the transfer out of NO_2 by isotopic exchange with water vapor (R55) - dominates. At $35km$, comparison of reaction rates R60 and R55 yields

$$\frac{k_{60} \cdot [NO] \cdot [O_3]}{k_{55} \cdot [NO_2] \cdot [H_2O]} = 1667$$

Thus the isotopic composition of NO_2 is indeed dominated by the ozone decomposition. Therefore, NO_2 is potentially able to produce a huge Δ^{17}-anomaly in stratospheric water vapor, and it would be very desirable to measure this reaction rate.

4.5.6 The Influence of Transport

A natural limit of a one-dimensional model is the lack of meridional transport. As was described above, water vapor enters the stratosphere dominantly in the tropics, is transported upwards and north-/southwards as part of the Brewer-Dobson circulation and returns to the troposphere at high latitudes. Thus water vapor at high latitudes is actually more influenced by stratospheric chemistry, as it has undergone a longer way through the middle atmosphere than water vapor at the bottom of the tropical tropopause.

So far, only the model of Ridal and Siskind [2002] of H_2O and CH_4 includes two-dimensional transport. The effect described above - "older" water vapor and methane at higher latitudes - is clearly visible in their model (see figure 4.22).

As was suggested by Johnson et al. [2001a], comparison of $\delta^{18}O$ and δD with v approximately removes the effects of transport. Johnson et al. [2001b] describe a simple photochemical model for the isotopic composition of water vapor as a result of methane oxidation and reaction with $O(^1D)$ only, with parameters optimized for their datasets. For comparison, their modeled δD and $\delta^{18}O$ is shown in figure 4.23. The agreement for δD is remarkable. The slight discrepancy at mixing ratios above $6ppm$ results from the photodissociation of H_2O which is not included in the model of Johnson et al. [2001b]. Also for $\delta^{18}O$ the general agreement is good, though the model of Johnson et al. [2001b] predicts an
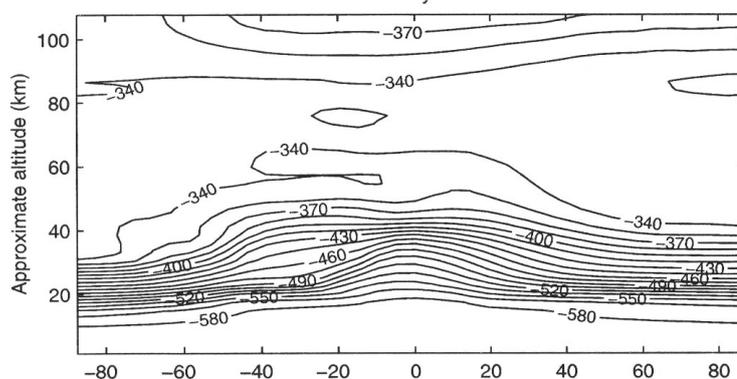
Figure 4.22 : δD *of water vapor as modeled by Ridal [2001]. The general effect of meridional transport is that water vapor in the polar regions is chemically "older".*

additional depletion of $\approx -25\text{‰}$. Considering that their model was optimized for their experimental data, which has typical errors of $> 50\text{‰}$, the agreement between the main features of the two models is satisfactory. However, the model presented here includes the whole photochemistry of water vapor, so that its sensitivity to input parameters can be tested thoroughly, while the accuracy of Johnson et al. [2001b] depends on the optimization to their datasets.

4.5.7 The Budget of the Middle Atmosphere

One distinct advantage of a numerical model over measurements is that sources and sinks can be calculated directly, and budgets of each individual atmospheric species can be compiled.

By adding up all sources and sinks of H_2O, CH_4 and H_2, the total amount of methane oxidized and H_2O, H_2 produced can be calculated. This calculation shows that a net $4.93 \cdot 10^{13} g/a$ of H_2O and $2.30 \cdot 10^{11} g/a$ of H_2 are produced from $2.31 \cdot 10^{13} g/a$ input of methane into the middle atmosphere.

The ratio between H_2O, H_2 net production and CH_4 loss can be calculated from the total source and sink strengths to be

$$\frac{P(H_2O)}{L(CH_4)} = 1.90$$
$$\frac{P(H_2)}{L(CH_4)} = 0.08$$
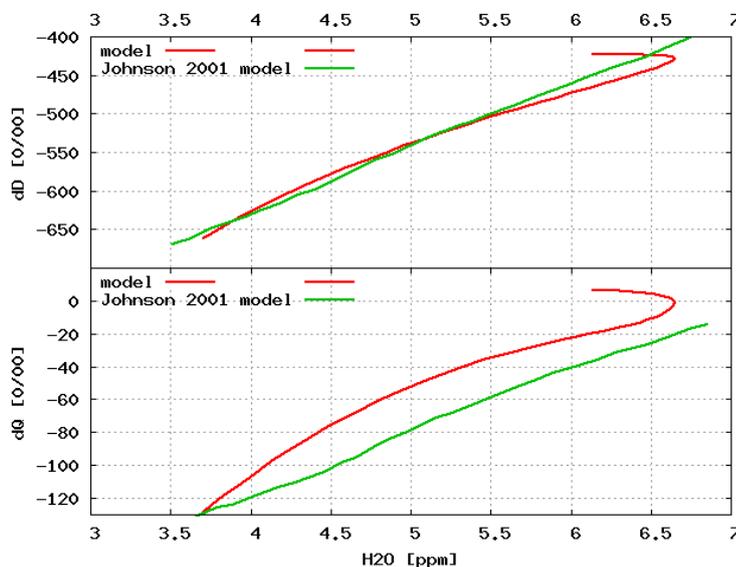
Figure 4.23 : $\delta^{18}O$ and δD plotted versus the H_2O mixing ratio. In comparison, the model of Johnson et al. [2001a] is shown.

which - for H_2O - is in good agreement with Dessler et al. [1996] (1.94 ± 0.27), and in reasonable agreement with Hurst et al. [1999] (1.973 ± 0.003) and Zoeger et al. [1999] (1.975 ± 0.030).

Interestingly, the gross production of H_2O in the middle atmosphere is much larger than its net production. An amount of $2.03 \cdot 10^{14} g/a$ - roughly four times the net production - is cycled through the OH_x family. The hydrogen isotopic composition of H_2O is limited by the total potential hydrogen amount $S = H_2O + H_2 + 2 \cdot CH_4$ and thus can not change much since total hydrogen is conserved. However, its oxygen isotopic composition is not bound by such a constraint. Thus, through this recycling through OH_x, water vapor could eventually reach equilibrium conditions with the oxygen and ozone reservoirs.

4.6 HTO - a Tracer for Atmospheric Transport

The radioactive tracer tritium differs from the stable isotopes as it has additional sources and an radioactive sink ($\tau = 17.8a$). However, for the discussion of HTO in the lower and middle atmosphere, more simplified models than the complex photochemical model described above can be applied, as the concentration of HTO varies over orders of magnitude. Therefore, smaller fractionation processes
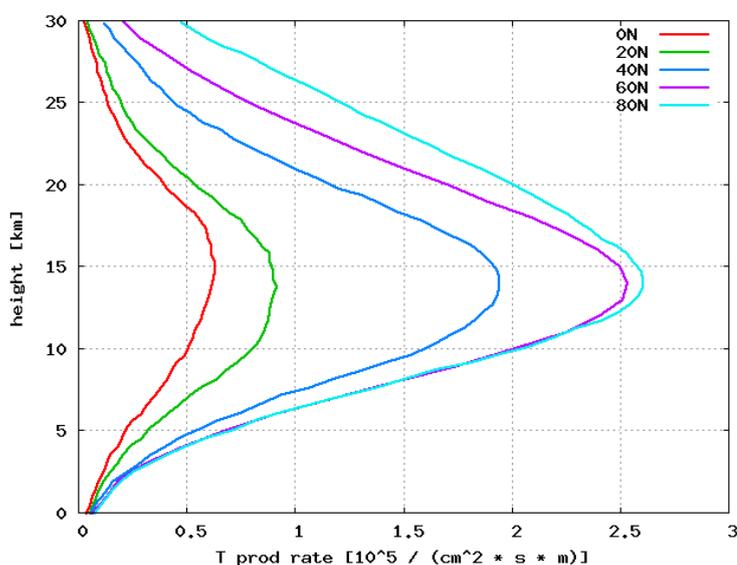
Figure 4.24 : *Latitudinal and height dependence of the tritium production rate [Zahn, 1995, Lingenfelter, 1963, Bhandari et al., 1966].*

play only a minor role.

Tritium is naturally produced by high-energetic nucleons (approximately 85% protons, 14% α-particles) stemming from cosmic rays. Its total production is estimated to be $\approx (0.25 - 0.28)cm^{-2}s^{-1}$ tritium atoms [Lal and Peters, 1967, Masarik and Beer, 1999] or $(200 - 224)g/a$. This results in a natural tritium reservoir of $\approx 3.6kg$ in equilibrium conditions. However, the production rate is dependent on latitude and height, as shown in figure 4.24. About two thirds of the production takes place in the stratosphere. Freshly produced tritium atoms are quickly incorporated into HO_2, OH and H_2O via reactions with O_2, O_3 and HO_2 (R12, R13, R14), respectively. From there on, they are incorporated into the water vapor and molecular hydrogen cycle.

During the 1950s, 1960s and 1970s there was a huge input of tritium into the stratosphere stemming from superficial nuclear bomb test by the USA, UK and USSR. Tests until 1962 released about $600kg$ into the atmosphere. After the Limited Test Ban, only an additional $\approx 20kg$ were released by France and China [Rozanski et al., 1991]. As the ocean acts as a giant tropospheric sink for atmospheric HTO (the tropospheric lifetime of water vapor is roughly ten days), the stratospheric HTO reservoir decreases mainly by stratosphere-troposphere exchange. Assuming a mean turnover-time of $5a$, much less than $0.4kg$ of all bomb-tritium injections should remain in atmospheric HTO at present time.

Currently, tritium is mainly produced anthropogenically by nuclear power plants ($\approx 25g/a$), experimental fusion reactors ($2.2-5.7kg/a$) and for military purposes for the maintainance of nuclear bombs ($\approx 5kg/a$). Consumer products are estimated to incorporate several hundred grams of tritium [Rozanski et al., 1991]. However, the total amount of anthropogenically produced tritium is hard to estimate.

A smaller amount of the anthropogenically produced tritium is incorporated into molecular hydrogen and methane. As the atmospheric lifetime of these two species are much longer than for water vapor ($2a$ for H_2, $7-8a$ for CH_4), some of the bomb-tritium remains in these species even today. Zahn [1995] quotes their tritium reservoirs in 1994 to be $\approx 0.35kg$ (HT) and $\approx 0.12kg$ (CH_3T), versus pre-bomb levels of $(2-5) \cdot 10^{-3}kg$ and $(0.5-1.8) \cdot 10^{-3}kg$, respectively [Zahn, 1995, Okai and Takashima, 1991]. Considering the atmospheric lifetimes of H_2 and CH_4, as well as radioactive decay, these tritium reservoirs should be smaller than $5mg$ (in HT) and $19g$ (in CH_3T) by today. Their tritium ratio can be approximated from the global hydrogen and methane burden ($\approx 200Tg$ of H_2 and $\approx 4850Tg$ of CH_4 [Seinfeld and Pandis, 1998]) to be $7TU$ and $5 \cdot 10^3TU$, respectively.

4.6.1 A Simple Model of HTO

To get estimates for the concentration of HTO in the troposphere and stratosphere, a simple one-dimensional model in C++ has been developed. It stretches from $0-35km$, with a box height of $1km$. The only effects modeled are evaporation of H_2O and HTO from the surface, vertical advective transport and precipitation. Further, production and decay of HTO is implemented into the model.

When discussing the atmospheric profile of HTO, the effects from tritiated methane and molecular hydrogen can nowadays be neglected. Molecular hydrogen is believed to have tritium ratios of $< 10TU$, whereas HTO reaches levels of $> 10^5TU$ in the stratosphere on its own, which will be shown below. For the same reason, CH_3T can only add a negligible amount of tritium to stratospheric HTO.

Evaporation from the surface is modeled by a constant flow of H_2O and HTO into the lowermost box. The evaporation rate is set to $0.7m/a$. This rate is typical for $60S$ [Roedel, 2000]. The tritium ratio of the evaporated water is modeled to have $0TU$, $10TU$ and $20TU$, which covers the range of surface waters.
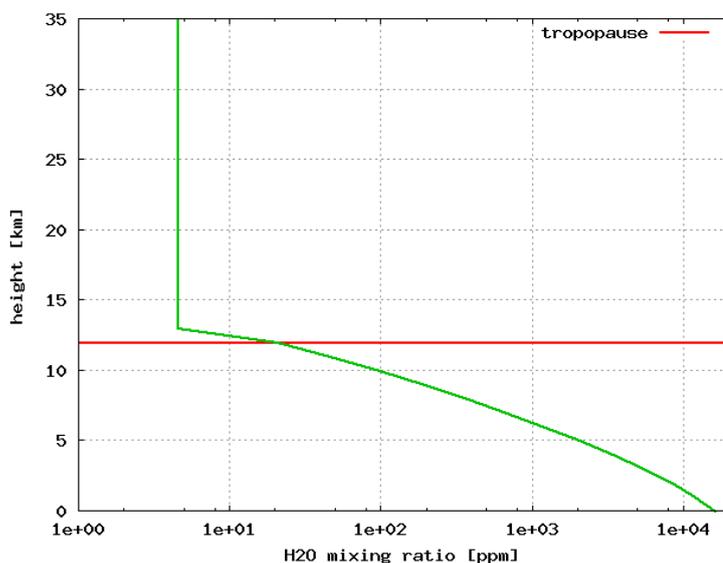
Figure 4.25 : *The modeled water vapor profile as used in the tritium model. As methane oxidation is not included in the model, the profile remains constant at* $4.5ppm$ *in the stratosphere.*

The vertical flux $F(HTO)$ can be described as the sum of $F_{adv}(HTO)$, the flux associated with advective transport, and $F_{liq}(HTO)$, which describes the transport of the liquid phase. $F_{adv}(HTO)$ can be calculated using equation 4.1. The eddy constants used are the ones given by Massie and Hunten [1981].

The flux describing transport in the liquid phase is coupled to the hydrological flux, so that $F_{liq}(HTO) = F_{liq}(H_2O) \cdot{}^3 R_{liq}$. Of course, during condensation, the temperature dependent equilibrium factors ${}^3\alpha_{vl}$ and ${}^3\alpha_{vs}$ (see equations 2.13 and 2.14) have to be taken into account. As only ${}^3\alpha_{vl}$ is known, it is also used as an estimate for ${}^3\alpha_{vs}$. Condensation removes all moisture above dew-/frostpoint in a single timestep. Reevaporation of falling droplets is not included in the model. The temperature profile used decreases linearly from $288K$ at the surface to $206K$ at $12km$, the tropopause level. Above tropopause level, no further condensation occurs. The resulting water vapor profile has a constant $4.5ppm$ in the stratosphere (see figure 4.25), as methane oxidation is not included in the model.

The production rate of HTO is taken from the $60S$ latitude dataset from Zahn [1995] (see figure 4.24). This choice of latitude is taken, as the air samples taken in this project stem from this region. Radioactive decay of tritium uses a decay rate $\tau = 17.8a$.
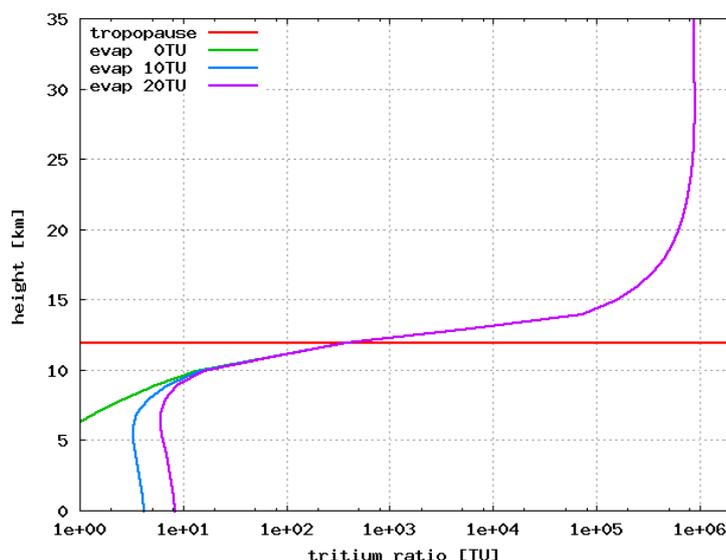
Figure 4.26 : *The modeled HTO profile shows a steep increase in the tritium ratio above $8 - 10km$. Below that level, the tritium ratio is more governed by evaporated surface-HTO. In the stratosphere, the ratio increases dramatically due to HTO production, a long stratospheric residence time and the low H_2O concentration.*

The modeled tritium ratios are shown in figure 4.26. The effects from HTO evaporating from the surface are seen up to $8 - 10km$. Above that level, the HTO profile is dominated by the tritium produced in the stratosphere. Here, the high production rate, the low water vapor content and the slow vertical transport result in a steep increase in the tritium mixing ratio. At the tropopause, the tritium ratio is about $370TU$; it sharply increases further to about $8.6 \cdot 10^5 TU$ in the upper stratosphere. The mass-weighted average of all HTO above the tropopause level is about $22000TU$. This number is only half the tritium ratio of $5 \cdot 10^5 TU$ given by Ehhalt et al. [2002]. Their estimate assumes a mean residence time of $5a$ for all water vapor above tropopause level, which seems to be quite high. Usually, troposphere/stratosphere exchange is quoted to have a characteristic time of $\approx 2a$ [Seinfeld and Pandis, 1998]. This results in a tritium ratio of $2 \cdot 10^5 TU$, which is in better agreement with the model presented here.

On the other hand, the model seems to underestimate the HTO mixing ratio in the troposphere right to the tropopause level, which will be discussed below.

Comparison with Measurements

Close to the tropopause, where the HTO-profile is dominated by transport via eddies, the HTO mixing ratio can be approximated by [Zahn, 1995, Ehhalt, 1971]

$$HTO(\Delta z) = C_1 \cdot exp\left(\frac{\Delta z + z_0}{a_1}\right) + C_2 \cdot exp\left(-\frac{\Delta z + z_0}{a_2}\right) \qquad (4.9)$$

where HTO, C_1 and C_2 are given in HTO-molecules per mg of air; Δz is the vertical distance to the tropopause. z_0, a_1 and a_2 are fit parameters given in km for the datasets of the various authors (here shown for mid-latitudes):

author	year	C_1	C_2	z_0	a_1	a_2
Ehhalt [1971]	1966	3.60	147.0	7.93	1.79	2.42
Mason and Östlund [1976]	1972	5.20	14.9	4.30	1.43	1.81
Zahn [1995]	1993	10.00	4.5	−0.60	1.75	2.35

Comparison between the model and the fits of the above mentioned authors is shown in figure 4.27. The washout of bomb tritium from the stratosphere over time is clearly visible. The highest HTO values at a given height above the tropopause are found in the early data from Ehhalt [1971], whose samples were taken in 1966. The data from Mason and Östlund [1976] already show washout effects, while the data from Zahn [1995] is thought to be almost free from bomb tritium effects.

The model seems to agree reasonably well from $2 - 5km$ above the tropopause level with the data from Zahn [1995]. However, below tropopause level the discrepancy between model and measurements become apparent. The model underestimates the HTO mixing ratio by a factor of ≈ 100. The reason is probably the instant removal of precipitation in the model. This leads to a far too high removal rate of HTO. Reevaporating rain drops would deposit HTO at lower levels and dampen the sharp decrease in HTO in the troposphere. However, reevaporation is very difficult to implement into the model. Therefore, the model is only useful from about $2km$ above tropopause level upwards. Below tropopause level, it may only serve as a lower limit.
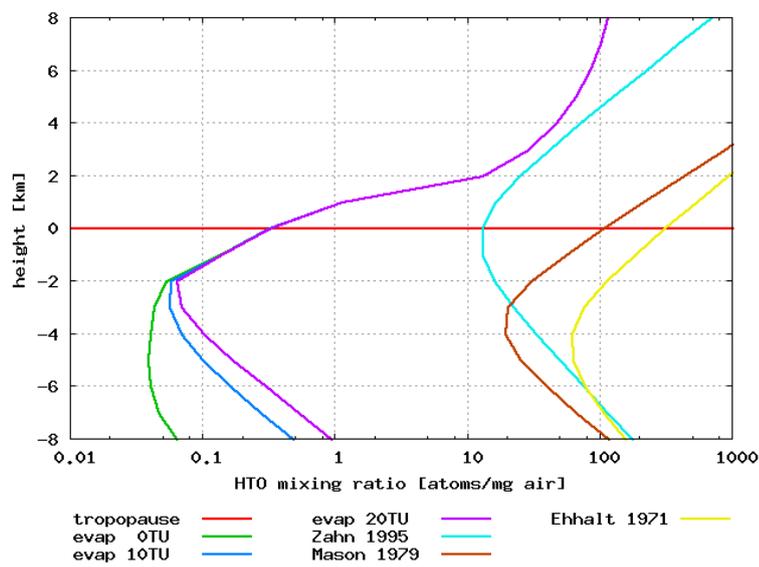
Figure 4.27 : *Modeled and measured HTO mixing ratios, plotted versus the distance to the tropopause. The profiles of Ehhalt [1971] and Mason and Östlund [1976] are influenced by high levels of bomb tritium. This effect is thought to be removed in Zahn [1995].*

Chapter 5

Analytical System

5.1 Isotope Ratio Mass Spectrometry

5.1.1 Principle of a Magnetic Sector Mass Spectrometer

In a mass spectrometer, atoms or molecules are ionized in the ion source (e.g. by electron collision) and accelerated in an electric field. Usually first passing through electric focusing lenses and slits, the ions are subjected to a magnetic force by a magnetic field:

$$\vec{F} = -(n \cdot e) \cdot \vec{v} \times \vec{B} \qquad (5.1)$$

where e is the elementary electric charge, $\vec{v}$ the particle's velocity and $\vec{B}$ the magnetic field strength. n is the number of electrons removed in the ionization, and is usually 1 as double or higher ionization rarely occurs. As the direction of the force points perpendicularly to both velocity and magnetic field, the ion is forced on a circular trajectory with radius

$$R = m \cdot \frac{v}{e \cdot B} \qquad (5.2)$$

where m is the mass of the particle. Therefore, the trajectory of a particle can be altered by either changing its velocity (by means of electric acceleration) or the magnitude of the magnetic field. However, by keeping both v and B constant, particles of different mass can be separated and leave the magnetic field on different trajectories. Detection can occur on a collector cup which is grounded via an electric resistor. An incoming particle may neutralize its electric charge
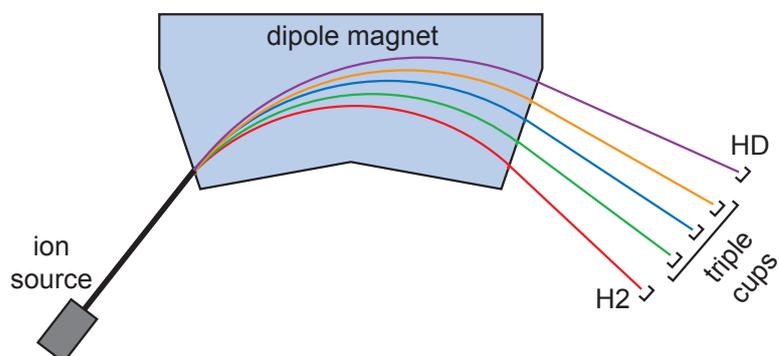
Figure 5.1 : *Ion trajectories in the Deltax-XP isotope ratio mass spectrometer. δD is measured using the outer cups, while oxygen analysis focuses on the inner triple cups.*

with a free electron of the detector cup. As this charge has to be replaced from ground, a current flows through the resistor which can be used to measure the signal strength of the particle beam.

Though a number of different mass spectrometer types exist (e.g. quadrupole, time of flight), the work described in this thesis has been exclusively performed on a dipole mass spectrometer with multiple detector cups, as schematically shown in figure 5.1. The isotopic composition of H_2O is determined after conversion to O_2 and H_2. Incoming oxygen molecules (masses 32, 33 and 34) are measured on the inner triple collector assembly, while hydrogen molecules (masses 2 and 3) are analyzed with the two outer cups at a lower magnetic field strength.

5.1.2   Sample Inlet

For the analysis of atmospheric trace gases, one usually has the choice between offline and online methods, which both have some advantages and disadvantages over each other.

In an offline method, the sample gas is usually concentrated and converted to a measureable species (i.e. CH_4 is converted to CO_2 for ^{13}C or to H_2 for deuterium analysis) in external sample containers (i.e. glass flasks). The sample gas then can be transferred into the mass spectrometer, usually through a dual inlet system as shown in figure 5.2. Here, the sample gas is admitted to the ion source through a system of valves that alternatively switch between sample and reference gas. To adjust the signal strength of both reference and sample gas to the same level, both are admitted from pressure adjustable bellows.
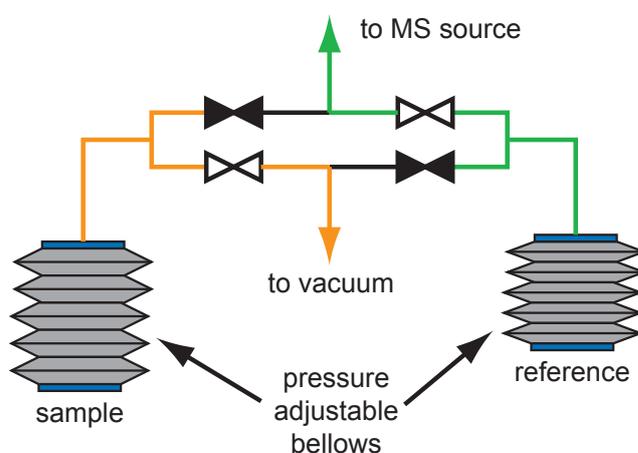
Figure 5.2 : *Working principle of a dual inlet system. Sample and reference gas are stored in pressure adjustable bellows. Capillaries connect the bellows to a change-over valve, which selects one of the two gases to flow into the evacuated mass spectrometer's source. The other gas flows into vacuum, so that there is always gas flowing through each capillary.*

The disadvantage of offline methods is that the sample size has to be sufficiently large (in the $\approx 50\mu l$ range) to be safely handled and transfered. For the analysis of an atmospheric trace gas that has a mixing ration of $1ppm$, one therefore needs to sample and store $50l$ of air to receive $50\mu l$ of sample material. This usually requires big sample containers at high pressure, which are hard to fill, handle and store.

A solution to this problem are online methods. They make use of the fact that a mass spectrometer actually needs much less sample to provide a sufficient signal than the amounts used in offline methods. The sample is concentrated and processed online, e.g. through a gas chromatographic system, and usually flushed into the mass spectrometer in a carrier stream of helium. The reference material is either also processed through the online system, or is introduced into the source by an open split acting as a switching valve (see figure 5.3). Usually, an aliquot size of $\leq 20nl$ is sufficient, leading to sample air volumes of roughly $20ml$ at $1ppm$ mixing ratios (though usually several hundred ml are sampled to provide a sufficient amount of aliquots).

The disadvantage of online systems versus offline methods is the reduced precision. This is due to the increased amount of background atoms from the carrier gas stream and the different signal analysis: The dual inlet provides a stable signal, while the online systems produce a peak which needs detection parameters
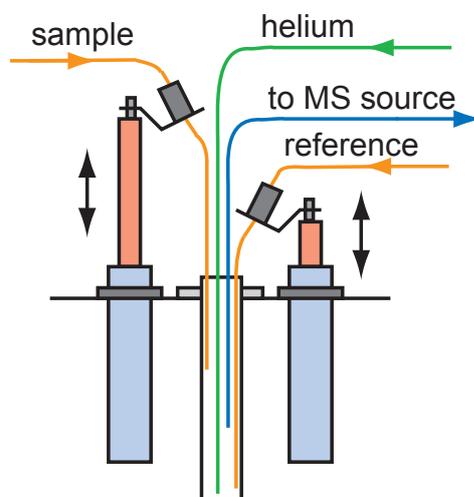
Figure 5.3 : *Working principle of an open split. It consists of a small glass tube, into which capillaries are inserted. Purified helium flows constantly into the split. The main capillary to the mass spectrometer is fixed, while transfer capillaries with sample or reference gas can move above or below the main capillary, thus acting like a valve.*

and background correction (see figure 5.4).

5.2   Conventional Water Isotope Analysis

Table 5.1 gives a rough overview over stratospheric measurements of stable water isotopes. Measurement errors are usually no better than $\approx 20‰$, $\approx 80‰$ and $\approx 70‰$ for δD, $\delta^{17}O$ and $\delta^{18}O$, respectively. The broad data ranges and large errors clearly indicate the need for a more precise measurement method.

Of the two rare oxygen isotopes, usually only the more abundant $\delta^{18}O$ is measured, as for all natural waters in precipitation and hydrology the MDF law applies. The standard measurement method for $\delta^{18}O$ is by equilibrating a water sample at $25C$ with CO_2 and measuring its isotopic composition. The isotopic composition of the water is used by applying the equilibrium fractionation

$$^{18}R_{H_2O} =^{18} R_{CO_2} \cdot^{18} \alpha \qquad (5.3)$$

with $^{18}\alpha = 1.04111$ at $25C$ (Brenninkmeijer et al. [1983] and references therein). $\delta^{18}O$ can be easily measured using mass spectrometry, but information about

author	δD			$\delta^{17}O$			$\delta^{18}O$			h [km]	
	min	max	σ_{min}	min	max	σ_{min}	min	max	σ_{min}	min	max
Abbas et al. [1987]	-470	-330	35							25	38
Carli and Park [1988]	-530	-380	72							31	38
Dinelli et al. [1991]	-461	-373	60	-368	-185	130	-106	-3	120	27	39
Dinelli et al. [1997]	-586	-455	75							20	38
Guo et al. [1989]							70	395	110	22	37
Johnson et al. [2001b]	-840	-420	?	-400	60	?	-300	75	?	9	38
Kuang et al. [2003]	-700	-320	21							8	22
Moyer et al. [1996]	-600	-450	30							15	40
Pollock et al. [1980]	-877	51	18							17	43
Rinsland et al. [1991]	-632	-524	80	-175	98	80	-141	75	70	20	54
Stowasser et al. [1999]	-840	-370	50							17	30
Webster and Heymsfield [2003]	-918	36	18	-123	167	?	-292	88	?		19

Table 5.1 : *Previously published stratospheric datasets of water vapor and its isotopic composition. Note that this table is only meant to illustrate data ranges and errors. Datasets which were only published in graphs are given approximately. The errors shown are the minimum errors found in the datasets and do not necessarily belong to the range borders displayed.*

$\delta^{17}O$ is lost due to the interference with the much more abundant ^{13}C signal on mass 45. Using water samples in the milliliter range, precisions up to $\pm0.01‰$ can be achieved using dual inlet mass spectrometers.

For the analysis of δD, the water sample is usually reduced to H_2 over a hot metal surface such as zinc, uranium, manganese, nickel or chromium [Gehre et al., 1996]. Precision is better than $\pm1‰$ using samples in the order of about $1\mu l$ for directly coupled preparation methods.

So far, only optical methods are able to measure both the oxygen and hydrogen isotopic composition in a combined measurement. While optical methods are of great importance for satellite-borne remote sensing instruments for investigations in the middle and upper stratosphere, where interference from the water-rich troposphere is diminishing, their practical use on airplanes in the upper troposphere and lower stratosphere is still limited by low accuracy. Webster and Heymsfield [2003] cite their precision within the range of $18-50‰$ for δD (the precision for a single measurement of $\delta^{17}O$ and $\delta^{18}O$ is not explicitly stated). However, using tunable diode laser spectroscopy, Kerstel et al. [1999] report their practical use in laboratories, where accuracies of $\pm3‰$ and $\pm1‰$ have been achieved on $10\mu l$ samples for δD and $\delta^{17}O$, $\delta^{18}O$, respectively.

One problem for the investigation of the isotopic composition of water vapor in the UT/LS by a sampling technique followed by high precision IRMS in the laboratory so far has been the huge amount of sample needed, at least about $10\mu l$ for oxygen isotope analysis. Associated with this large amount of sample is the need for a sampling device which is capable of removing the low water

content - about $3 - 5ppm$ - from a stratospheric air parcel. At the same time, traps have to be sufficiently small in order to minimize memory effects of water adsorbed on surfaces. These memory effects can be reduced by baking the system out at elevated temperatures, which is hard to achieve with big traps. Also, the application of cryogenic traps aboard aircrafts and balloons requires them to be as small and light as possible and to consume a minimum amount of cooling fluids. Addressing all these issues, reducing the sample size to a minimum appears to be the natural choice.

With continuous-flow isotope ratio mass spectrometry (CF-IRMS), the required sample size can be downsized considerably. Begley and Scrimgeour [1997] reported a CF-IRMS pyrolysis system for δD and $\delta^{18}O$ analysis of $5nl$ aliquots with precisions of $\pm 2‰$ and $\pm 0.3‰$, respectively. The system consists mainly of an alumina tube filled with Ni-wires at a temperature of $1050C$. H_2O is reduced to H_2 and CO by reaction with carbon deposited on the Ni surface. The disadvantage of this system is that $\delta^{17}O$ can not be measured due to interference from the stronger ^{13}C signal.

Baker et al. [2002] reported a system to reduce H_2O to O_2 by reaction with CoF_3 at $370C$ to measure both $\delta^{17}O$ and $\delta^{18}O$. Using aliquots of $20nl$, the precision of this system is about $\pm 0.5‰$ for $\delta^{18}O$ and $\pm 0.3‰$ for $\delta^{17}O$.

Both systems make use of a syringe for the injection of liquid samples. For atmospheric samples, this is a disadvantage, as it requires the sample to be larger than the amount to be analyzed and to be at least in form of a droplet that can be soaked into the syringe.

Therefore, the aim of this project has been to develop a system with the following properties:

- combined measurements of δD, $\delta^{17}O$ and $\delta^{18}O$ on a single sample

- minimizing the amount of sample required

- making the use of sample containers possible

- minimizing memory effects in the handling and processing of the sample

5.3   Experimental Setup

Figure 5.12 gives an overview of the new system. It consists of an insulated box heated to $240C$ which contains all parts that have contact with water vapor in

order to minimize memory effects. All lines shown are of $0.0625"OD \times 0.020"ID$ stainless steel, if not specified differently.

For real atmospheric water vapor samples, separate traps have to be used which can be filled in an in-situ sampler. In order to test the performance of the analytical system alone, a calibration trap built into the system was used.

A water sample of normally $120nl$ volume is injected into a stream of purified helium through a high temperature septum (ALLTECH, part no 15132) using a $0.5\mu l$ syringe (HAMILTON, part no 89259/00). The septum is placed outside the box for easy access and is located at the end of a $2mm\,ID$ stainless steel tube heated to $200C$ for fast evaporation.

The sample enters the calibration trap, a dead volume of $150ml$ made of stainless steel heated to $270C$ and kept at a constant absolute He pressure of $2bar$. The exit of the container is connected to a 4-port Valve (Valco, part no C4UWT) which is used to switch between the calibration trap and a real external sample container.

From the helium diluted sample, several aliquots can be taken using a 6-port Valve (Valco, part no C6UWT) and a cryogenic focus trap. The focus consists of a $15cm$ stainless steel tube $0.125"OD \times 0.085"ID$ with a $20\mu m$ stainless steel frit (ALLTECH, part no 703225) inserted $4cm$ into the tube to prevent ice crystals to be carried away in the gas stream. On the outside, a thermocouple is located in the middle of the tube and tucked to it by a coil of sheathed heating wire. The focus tube is centered into a $10mm\,ID$ stainless steel tube and sealed into it with ceramic glue at both ends (Cotronics Corp., Durapot 809). Two $0.25"$ tubes welded to top and bottom of the outer tube hold adapters to teflon tubes, through which liquid N_2 can be pumped. The so-built cryofocus is operated at either $-120C$ by evaporated nitrogen gas cooling or $+400C$ by using the heating wire. The flow trough the calibration trap and the focus is controlled by a mass flow controller at the outlet (MKS, part no 1179AX11CS1BW).

After an aliquot of the sample has been trapped in the focus, the 6-port valve is switched and the focus is heated, so that the sample is carried away in a clean He stream controlled by a second mass flow controller (MKS, part no 1179AX11CS1BW). The analysis mode - oxygen or hydrogen - can be selected by two further 4-port valves, leading the He stream through the selected conversion system. The non-used system is flushed with He. After conversion, as detailed in the following paragraphs, the sample enters an open split from which it is admitted into the mass spectrometer (Thermo Finnigan, $Delta^{plus}XL$).

Oxygen analysis: H_2O reacts with CoF_3 according to the reaction

$$2H_2O + 4CoF_3 \longrightarrow 4CoF_2 + 4HF + O_2 \tag{5.4}$$
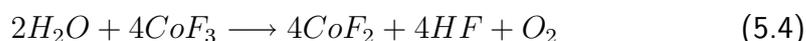
The reaction takes place in a nickel tube $0.125"OD \times 0.083"ID$ (ALLTECH, part no 30801) of $13cm$ length with a stainless steel frit inserted $1cm$ from the bottom. It is filled with approximately $180mg$ of CoF_3 and fixed in an aluminium block furnace ($4cm \times 4cm \times 10cm$) at $370C$, following the recommendations given by Baker et al. [2002]. The HF produced is removed in a NaF trap by the reaction

$$NaF + HF \longrightarrow NaHF_2 \qquad\qquad (5.5)$$
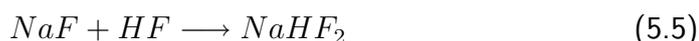
The NaF trap consists of a $5cm$, $0.125"OD \times 0.085"ID$ stainless steel tube with steel frit completely filled with NaF (approximately $130mg$). Any condensables left in the gas stream are removed by a subsequent liquid nitrogen trap and can be vented to safety during night.

Hydrogen analysis: Following roughly the method described by Begley and Scrimgeour [1997], a $29cm$ long $0.0625"OD$ alumina tube is filled with 3 strands of nickel wire and located in a tube furnace. Carbon is deposited on the Ni-surface by adding methane through a prime/purge valve (SGE, part no 1236103) to the helium stream. H_2O is reduced to H_2 and CO at $1050C$; a Nafion water trap is used to prevent possible traces of H_2O to flow into the mass spectrometer.

5.4   Experimental Procedure

For the characterization of the analytical system the calibration trap is used instead of a real trap. For the analysis of a sample, the syringe is first cleaned with acetone in order to prevent cross-contamination between samples. Then it is loaded with the sample water. The needle is purged about ten times with the sample water prior to injection. As the standard amount, $120nl$ is loaded into the syringe and injected via the septum into the calibration trap. The needle remains in the hot injection port for about $25s$ to ensure complete evaporation. As the pressure in the $270C$ hot calibration trap of $\approx 150ml$ is about $2bar$, the resulting initial mixing ratio is about 0.1%.

While loading the focus trap, the flow out of the calibration trap is $4ccm/min$. The flow is set to zero at all other times to save sample material. The focus is loaded for $120s$ at $-120C$, which corresponds to an initial aliquot amount of $\approx 350nmol$ of water. Of this first aliquot, less than $175nmol$ of hydrogen or $22nmol$ of oxygen will pass into the mass spectrometer. The rest is vented away in the split which has a ratio of $2:1$ for hydrogen and $8:1$ for oxygen analysis. $350nmol$ of sample may appear quite large for a CF-method, but each

aliquot has to pass through the whole analytical system where it can be effected by memory effects. Hence wasting some of the sample material in the open split is preferred to minimize contamination in the system.

The remaining sample is continuously diluted with helium, this mixing ratio and the aliquotted amount decrease with a characteristic decay time $\tau \approx 96min$.

After loading, the focus is switched to injection mode and heated to $400C$; the injection flow is either $8ccm/min$ for oxygen or $2ccm/min$ for hydrogen analysis. The aliquot is converted as described above, analyzed in the mass spectrometer and the cycle is repeated. In this fashion, more than 25 aliquots can be analyzed from a single injection, usually $10-12$ injections for O_2, the rest for H_2 analysis. Thus, about ten individual measurements for both signatures are carried out and the isotopic composition of the injected sample can be derived from the entire time series of the aliquots, as will be explained below.

After the last measurement, the mass flow controller valve is fully opened and the calibration trap purged for at least $20min$ at roughly $80ccm/min$. Before each new sample, a system blank is measured, and no traces of vapor of the previous sample have been detected using this purging method.

Figure 5.4 shows the MS chromatograms for oxygen (masses 32, 33 and 34) and hydrogen (masses 2 and 3) of one aliquot, each followed by reference gas injections via the open split interface. The asymmetry of the peak is caused by rapid heating and slower decay due to adsorption of H_2O on walls of the tubes. Blanks, i.e. measurements without injections of H_2O, give peak heights of a few millivolts and few seconds in length only, therefore the background is negligible.

In order to allow for the combined measurement of hydrogen and oxygen isotopes, the following details have to be explained:

- The $Delta^{plus}XL$ mass spectrometer is focused to an intermediate setting. This somewhat limits the precision and signal height of the O_2 beam, but still gives satisfactory results. This problem can be avoided using a MS with automatic electronic focussing like the new $Delta^{plus}XP$ instrument, which allows fast switching from H_2 to O_2 analysis. Such an instrument has been used in the later stages of this project.

- In principle, an even smaller sample amount - about $60nl$ - is required for the hydrogen analysis only, while for oxygen analysis the larger amount of $120nl$ is desirable, since memory effects play a larger role, as will be explained later. Therefore, oxygen analysis is performed first and the system is switched to hydrogen analysis after about 10-12 aliquots have been measured and half of the sample has been used.
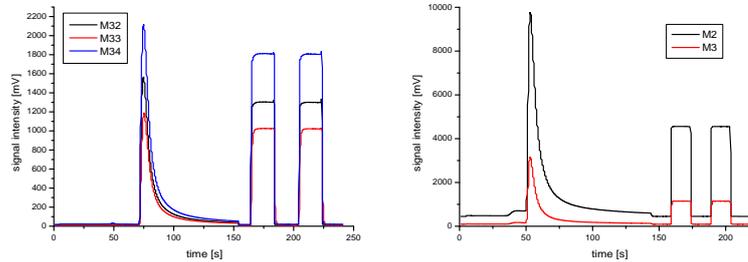
Figure 5.4 : *Signal of the mass spectrometer during the analysis of an aliquot. Signals for oxygen (masses 32, 33 and 34) and hydrogen (masses 2 and 3) are shown. Although the actual amount of sample is less for H_2 than for O_2, the signal is higher due to different amplification factors for the different collectors as well as the different flow rates for the two analysis systems. The asymmetry of the peaks is due to rapid heating and sticking of H_2O molecules onto surfaces, resulting in a broad tail.*

5.5   Data Interpretation

Ideally, each aliquot measured should have the same isotopic composition. Due to a number of effects such as memory, mixing, isotopic exchange and fractionation, the values for each aliquot differ from each other and show a time evolution. Figure 5.5 shows the typical time series of a sample. Generally, both hydrogen and oxygen values show a trend. The oxygen values might be influenced by isotopic exchange with oxygen on the steel surfaces, as will be explained later.

Therefore, the area-weighted average of the δ-values given by the mass spectrometer was chosen as a "machine response" of a sample:

$$\delta X_{ms} = \frac{\sum_i A_i \cdot \delta X_i}{\sum_i A_i} \tag{5.6}$$

where A_i is the measured peak area of the i-th peak and is decaying roughly exponentially with time. δX_{ms} is not the true isotopic composition of the sample, but the true value can be found by applying a calibration.
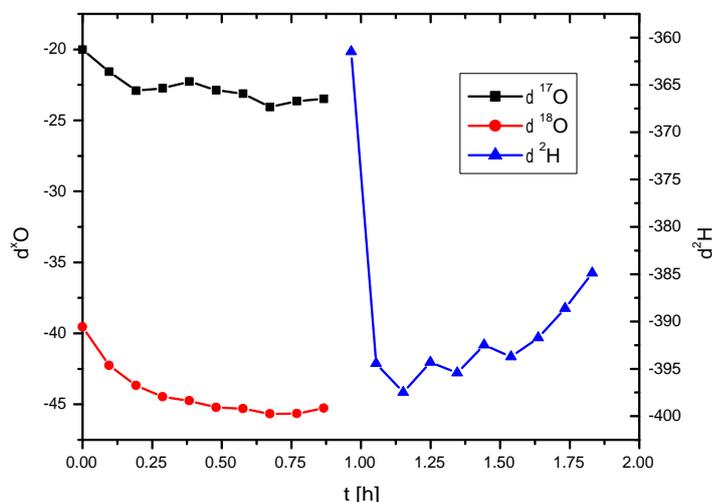
Figure 5.5 : *Isotopic time series of a typical sample (7th injection of SLAP). Plotted δ-values are the direct output given by the mass spectrometer software. Note different scales for oxygen and hydrogen values.*

5.6   Results

5.6.1   International Reference Standards

To specify the performance of the analytical system, injections of the three principal international reference standards VSMOW, GISP and SLAP were made; the results are shown in figure 5.6.

The measured values for δD reach their steady state values immediately after changing the sample material, while the values for $\delta^{17}O$ and $\delta^{18}O$ clearly display memory effects. This effect demonstrates that there is a reservoir of oxygen in the system which isotopically exchanges with the sample water. Memory water itself can be ruled out as a major reservoir, as it would also cause the δD measurements to be influenced. The measured values are summarized in table 5.2, ignoring the first sample of VSMOW and the first two samples of GISP and SLAP for $\delta^{17}O$ and $\delta^{18}O$.

Using the data obtained in this measurement series, a linear calibration can be applied. A difficulty here is that the $\delta^{17}O$ composition of GISP and SLAP are not well established. Li et al. [1988a] quote it to be $-(13.14 \pm 0.19)‰$ and
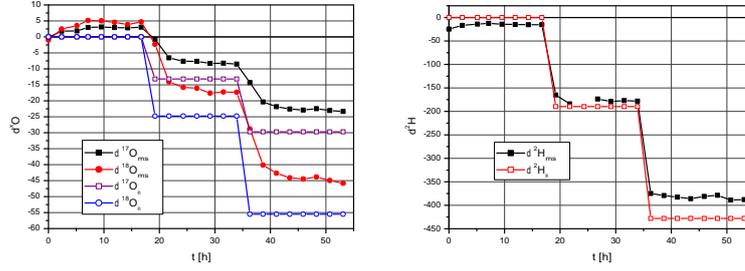
Figure 5.6 : *Time series of injected reference standards. δD_{ms} reaches it steady-state value immediately after changing the reference material, while $\delta^{17}O_{ms}$ and $\delta^{18}O_{ms}$ display memory effects.*

	$\delta^{17}O$				$\delta^{18}O$				δD			
	ref.	$\bar{x}$	σ_{n-1}	n	ref.	$\bar{x}$	σ_{n-1}	n	ref.	$\bar{x}$	σ_{n-1}	n
VSMOW	0	2.65	0.56	7	0	4.18	0.95	7	0	-16.0	3.7	8
GISP	-13.17	-8.06	0.41	5	-24.79	-16.81	0.82	5	-189.7	-176.1	6.4	6
SLAP	-29.70	-22.69	0.52	6	-55.50	-44.31	1.10	6	-428.0	-382.4	4.9	8

Table 5.2 : *Steady state data for the injected reference standards. Note that the first sample of VSMOW and the first two samples of GISP and SLAP are not included in the statistics of $\delta^{17}O$ and $\delta^{18}O$. All δ-values are expressed in ‰.*

$-(29.90 \pm 0.22)$‰, respectively. Meijer and Li [1998] have measured natural waters over a wide range and have established the $\delta^{17}O = (\delta^{18}O + 1)^{0.528} - 1$ relationship, though they do not quote the $\delta^{17}O$-values for GISP and SLAP. By applying the power law, $\delta^{17}O = -13.17$‰ and $\delta^{17}O = -29.70$‰ are calculated for GISP and SLAP, which is within the errors quoted by Li et al. [1988a]. Therefore, the calculated values are adapted here.

With the given isotopic composition of the reference materials, the true δ-values can be calculated as $\delta X = A + B \cdot \delta X_{ms}$ using the following parameters:

	$\delta^{17}O$	$\delta^{18}O$	δD
A	-3.303	-5.045	17.661
B	1.169	1.142	1.167
R^2	0.9977	0.9980	0.9991

The precision after applying the calibration is lowered by the fact that $B \geq 1$. This results in a standard deviation of $\sigma = \sigma_{ms} \cdot B$. Therefore the overall precision of the calibrated system is about 0.7‰, 1.3‰ and 7‰ for $\delta^{17}O$, $\delta^{18}O$ and δD, respectively.

5.6.2 Mass Independently Enriched Sample

In order to test the system's ability to measure samples not obeying the mass-dependent-fractionation law, a special mass-independently-fractionated water sample was prepared. MIF-O_2 was prepared by mixing tank oxygen with a small amount of O_2 artificially enriched in $\delta^{17}O$. MIF-CO_2 was produced by combusting carbon in a vessel containing the MIF-O_2 mixture. About $2.4mmol$ of this CO_2 was equilibrated with $1.0g$ of H_2O in a water bath at $25C$ for one week to ensure complete isotopic exchange. Afterwards, the sample water was frozen with a dry ice-acetone mixture at $-78C$ and the CO_2 separated into another vessel using liquid nitrogen.

Using the oxygen isotope exchange method developed by Assonov and Brenninkmeijer [2001], the isotopic composition of the CO_2 was measured on a dual-inlet mass spectrometer. The isotopic composition of the water was calculated using the known fractionation factor for $\delta^{18}O$ and assuming $^{17}\alpha = (^{18}\alpha)^{0.528}$ as suggested by the MDF-law. Using the method described in this paper, the sample water was measured four times with the new system. Ignoring again the first values due to memory effects, the remaining three measured values show excellent agreement with the CO_2 method, as displayed in figure 5.7.

5.7 Discussion

The system described above has been designed for measurement of all three stable isotope signatures of small atmospheric water vapor samples. In its present state, the precision of the analytical system is sufficient to allow detailed investigations of water transport in the atmosphere. For the characterization of the system, a sample size of $120nl$ of water has been chosen, which is at the low end of what can be handled in a reproducible manner with syringe injections for testing/calibration purposes, and on the other hand can be sampled in the atmosphere in a reasonable time. For modern continuous-flow techniques this is still a huge amount of sample; 25 injections are made and several hundred nanomoles used per injection. Thus, from the MS side, the system could certainly be downsized further, without severe loss of precision, for example by decreasing the peak area or the split ratio in the open split interface. A reason for sticking to the large peak sizes in the present setup is the presence of remaining memory effects which are expected to get larger on smaller sample peaks.

The memory effect evident in the oxygen isotope measurements were later confirmed to be due to oxidized steel surfaces, as inspection of the calibration trap revealed oxidation on its walls. Hence an isotopic exchange between surface
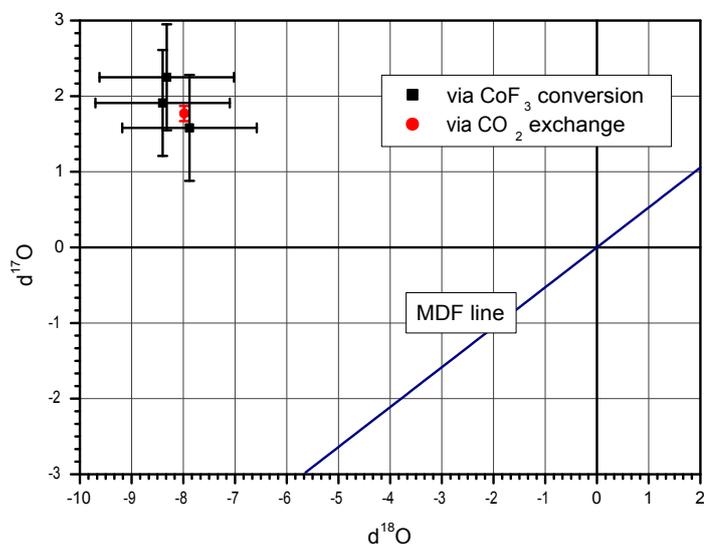
Figure 5.7 : *Results of the MIF water sample. The three datapoints of the CoF_3 conversion method agree very well with the CO_2 exchange method. The error bars indicate the typical error for the analytical system.*

oxygen and the water sample seems likely. This also explains the trend in the δ-values for oxygen in the aliquot time series, as this is an indication for the ageing of the sample inside the calibration trap. To avoid this source of error, the next version of the calibration trap was built using a gold plated inner surface. Though the measurements described above were not repeated at full length due to limited mass spectrometer time, simple experiments with syringe injections revealed a drastic drop in the memory effects. As the main interest in this work has been the measurement of external atmospheric samples, these sample containers were built with gold plated surfaces, and after thorough testing of the system performance no further series of experiments were performed using the auxiliary calibration trap. Memory effects of the external sample containers are further described in section 7.4.7.

Another possible limitation on the precision are the broad and asymmetric sample peaks in the mass spectrometer. As mentioned above, they arise because the water is released from the focus trap by heating, which for a sticky substance like water takes relatively long and leads to the asymmetric peak shape. This could be improved by refocusing the products O_2 and H_2 after conversion and then eluting onto a short column before the samples enter the open split interface.

In the case of O_2, refocusing is not feasible since there is a slow bleed out of the CoF_3 reservoir for days to weeks after putting in a new batch of CoF_3. This O_2 would be concentrated together with the sample O_2 and contaminate the measurement, as established by repeated blank tests. Therefore this has not been pursued further. For H_2, however, refocusing H_2 on molecular sieve, as done in the method for determination of the isotopic composition of atmospheric hydrogen [Rhee et al., 2004], could improve the precision.

One final limitation on sample size is that the blank water from sample containers has to be negligible compared to the amount of sample. The absence of system blanks from the calibration trap after flushing with He in between sample injections indicates that this is indeed the case.

5.8 External Samples

As described above, the analytical system allows analysis of external sample containers. Like the internal calibration trap, external sample containers must be heated in order to to avoid water molecules sticking to their walls. Further, the connection lines of the sample containers have to be purged prior to analysis to avoid atmospheric water vapor mixing with sample water.

Figure 5.11 shows the setup for external samples. The sample containers are placed in a standard household oven at $T = 250C$. In order to avoid temperature fluctuations, the oven has been modified and possesses an external temperature controller (JUMO, iTRON16), which keeps fluctuations below $2C$. The valves inside the oven (V1,V2 and V3) are Nupro SS-4H with modified steel handwheels, as the standard aluminium handwheels tend to destroy the valves during the heating/cooling processes.

The experimental procedure is as following: The sample container is connected to a helium and vacuum line via valves V1,V2 and V3 as shown in figure 5.11. After it is connected to the lines, the connection line is evacuated for $10min$ prior to analysis by closing V1 and V4 and opening V2 and V3. The vacuum reaches a minimum of $10^{-2}hPa$ using the vacuum pump (Pfeiffer, DUO 2.5). Thereafter, the vacuum valve V3 is closed and the righthand line is filled with helium (V4 open). The outlet line is opened so that helium flows through the bypass valve V2 into the analytical system. In this mode, the standard blank is measured.

If the standard blank shows no irregularities, the bypass valve is closed and helium is allowed to flow into the container via V5. As the container is usually

evacuated after filling with sample water, valve V6 is opened about $30s$ later to avoid backward flow through the analytical system into the sample container.

In the first measurement run after opening the valves of the sample container, $12ccm$ of gas from the sample container is flushed through the analytical system in order to fill the lines with the sample. Analysis of the samples is carried out as already described in section 5.4, except that $4ccm/min$ flow is used during loading and $1ccm/min$ at other times. The helium pressure is the same as for the calibration trap ($2bar$ absolute pressure) and the external sample containers also have about $150ml$ volume, so that peak areas are of the same magnitude as for the calibration trap.

After the sample has been analyzed, the container is flushed for $20min$ with the MFC's valve fully opened. Afterwards, it is filled with $2bar$ of helium and locked, so that it is not underpressured after cooling and can be stored without risk.

When analysis of external sample containers was tested, a problem arose with the analysis of H_2. It appears that nitrogen leftovers from the filling of the traps caused increased collisions of molecules in the mass spectrometer, making accurate measurements of δD impossible. As a tight time schedule had to be kept, this problem could not be addressed, so that only oxygen isotope analysis is possible with external sample containers at present. However, it is believed that this problem can be solved in the future.

The design of the external sampling containers is described in the next chapter. Results of calibration and atmospheric sampling with these containers are found in chapters 7 and 9.
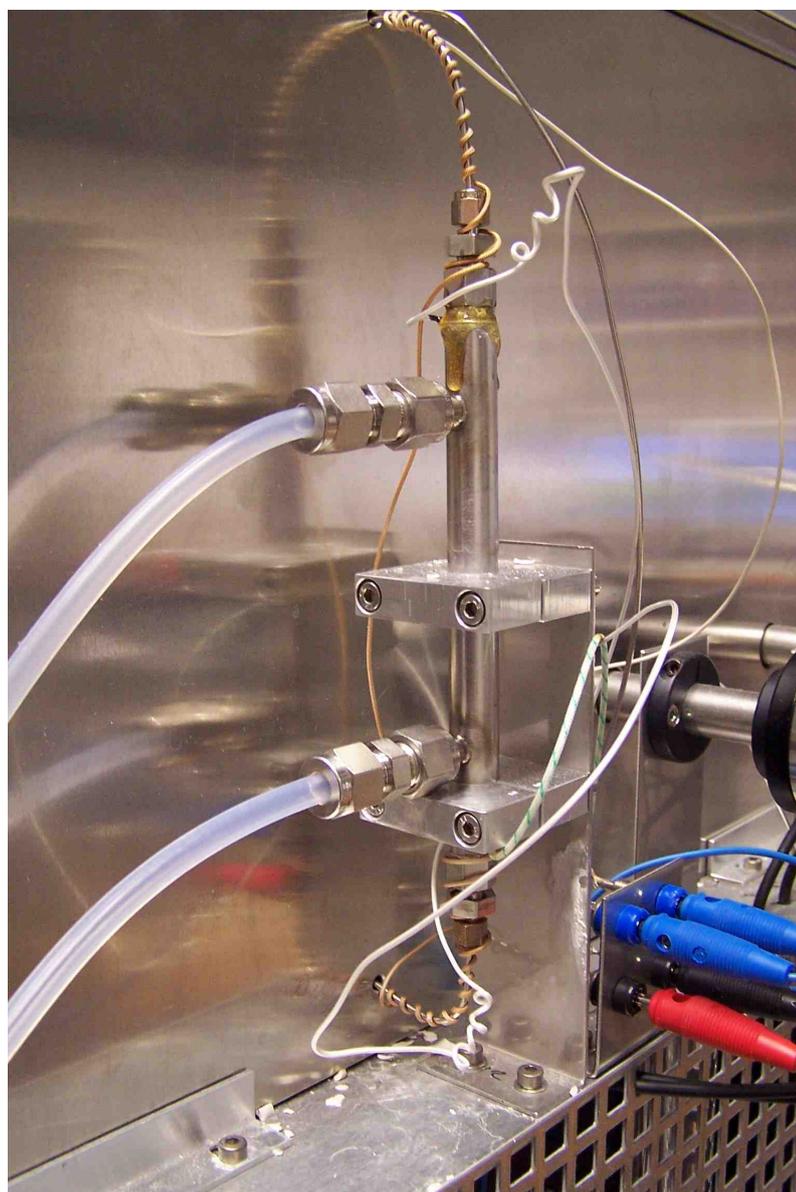
Figure 5.8 : *The H_2O focus unit of the analytical system. Shown are the teflon lines for the evaporated liquid nitrogen, and the coiled heating wires.*
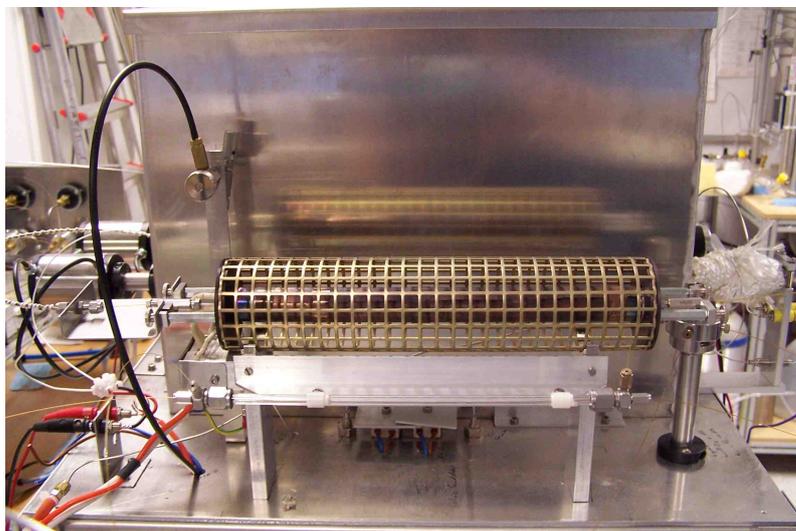
Figure 5.9 : *Hydrogen pyrolysis furnace. To its bottom, the nafion tube for trace water removal after pyrolysis is can be seen.*
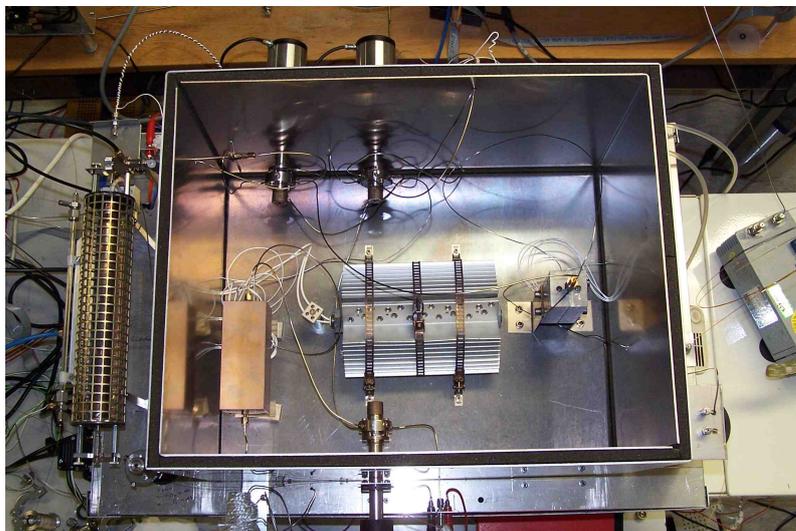
Figure 5.10 : *The analytical system as seen from top. Inside the heated box, the calibration trap is located at the bottom left side. The big block in the center serves as heater for the box. To its right, the CoF_3 block furnace can be seen. The switching valves for the focus are on the top right, H_2/O_2 analysis switching valve on the top left and internal/external sample switch at the bottom.*
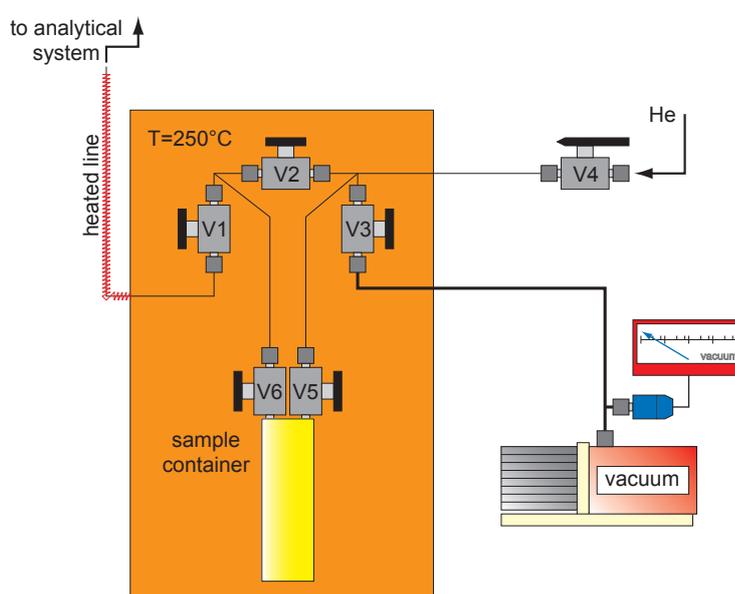
Figure 5.11 : *Setup for external sample containers. The container and all valves that have contact with H_2O are enclosed in an oven at $T = 250C$. The connection to the sample container can be evacuated prior to analysis via the vacuum pump. During analysis, valve V2 is closed to allow the helium gas to stream through the container.*
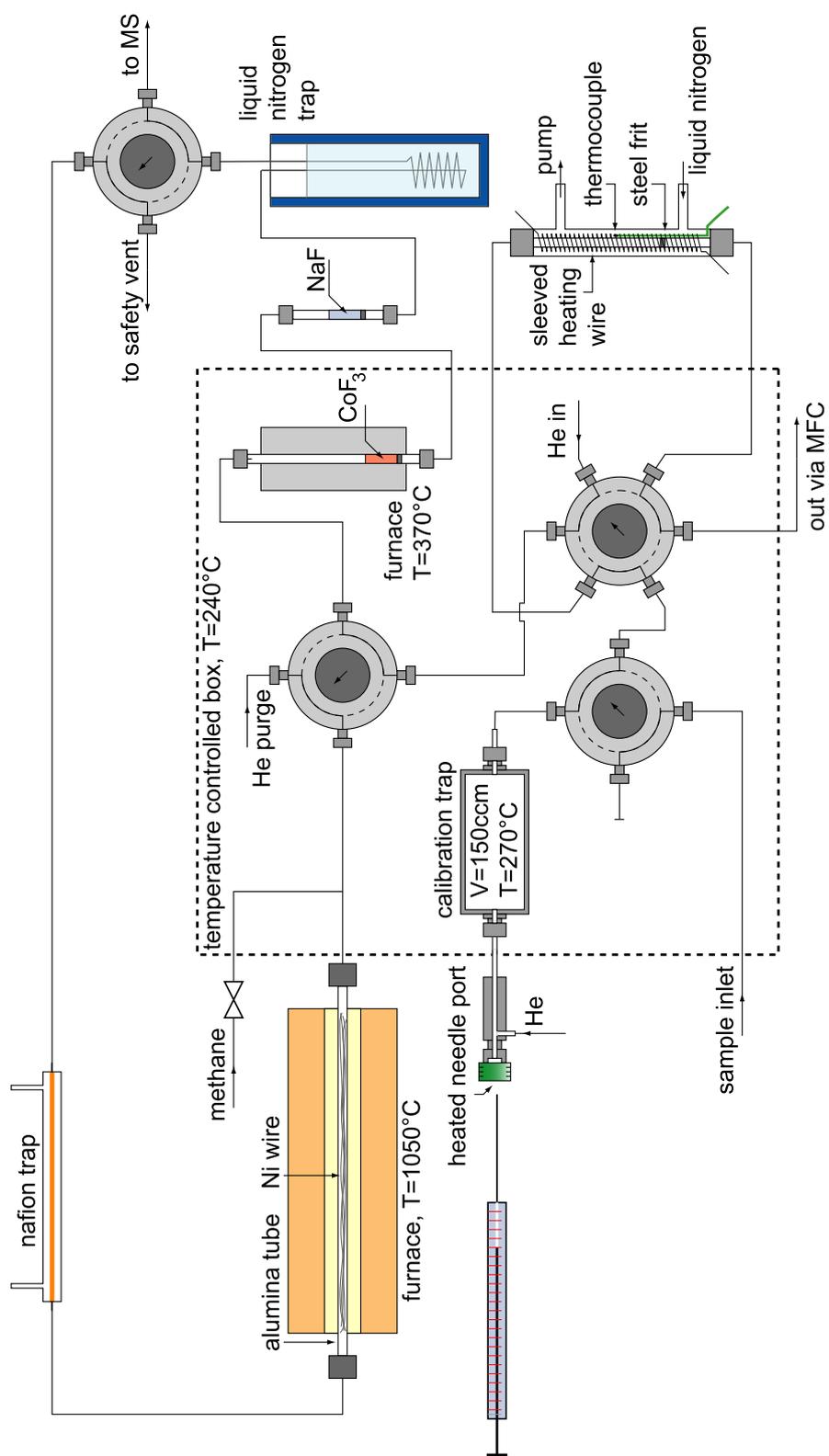
Figure 5.12 : *Setup of the system; description see text.*

Chapter 6

Sampling System

6.1 Sample Containers

Special attention has been given to the design of the sample containers. As purging these containers is achieved fastest by applying heat, all parts of the container including the valves are chosen to withstand heat and a huge number of heating/cooling cycles. First tests with standard metal bellow valves (Nupro SS-4H) showed that they were wearing out after a couple of heating/cooling cycles due to expansion problems of the sealing stamp. Therefore, the more reliable valve type SS-4BG was chosen, which can be heated up to $400C$.

VCR fittings were chosen for connections as they can withstand a great number of opening/closing cycles and heat, whereas standard Swagelok fittings tended to bake together in the oven. Also, replacement of the sealing rings of the VCR fitting is easy.

In the construction of the sample containers, gold plated surfaces were used to avoid similar problems as with the first stainless steel version of the calibration trap. However, of the 20 sample containers built, three were kept in unplated stainless steel. These three sample containers showed in later experiments the same behavior as the gold plated containers. It can therefore be assumed that stainless steel is a valid option, as long as there are no oxidized spots on it. However, with no long-term storage tests available so far, the gold plated traps are preferred. Covering all stainless steel surfaces in the traps has not been possible, as even the gold plated containers possess stainless steel valves and a stainless steel frit.

A crucial parameter for the design of the sample container is its length, as this limits the trapping efficiency at a given air flow. This is very important,

since the equilibrium fractionation factor of water vapor increases with decreasing temperature, and Rayleigh distillation effects will certainly occur with loss of sample.

If the container walls can be treated as a black surface (i.e. no water molecules bouncing from them), the trapping efficiency under laminar flow can be approximated to be [Zahn, 1995, Franz, 2002]:

$$\eta \;=\; 1 - exp\left(-\frac{5.76 \cdot V \cdot D_{H_2O}}{F \cdot R^2} \cdot \sqrt{\frac{T}{293K}}\right) \qquad (6.1)$$

$$\;=\; 1 - exp\left(-\frac{5.76 \cdot \pi \cdot L \cdot D_{H_2O}}{F} \cdot \sqrt{\frac{T}{293K}}\right) \qquad (6.2)$$

where $D_{H_2O} = 0.33 cm^2/s$ is the diffusion constant of water vapor in air at $293K$ and $1013 hPa$. L is the length of the trap, and F the mass flow rate. The constructed traps have a length of $25cm$. Therefore, at a flow rate of $300 mL/min$, it's maximum trapping efficiency is $> 99.999\%$.

Another limit to the trapping efficiency is the water vapor saturation pressure at the bath temperature. However, as liquid nitrogen is used as cooling agent, the remaining water vapor pressure can be neglected.

Further, the efficiency of the trap can be limited by ice particles that are carried away in the gas stream. These particles are potentially enriched in heavy isotopes and thus impose a further threat to measurements. To avoid ice particles being blown away, a frit was inserted into the stub end of the coaxial trap, which can be seen in figure 6.1.

6.2   Main Dewar and Sampling Manifold

The central part of the sampling system is a liquid nitrogen dewar, into which the sample containers can be inserted. This main dewar can hold up to ten sample containers. It consist of a solid outer aluminium shell, and a welded inner part made out of stainless steel. The inner shell is covered by an insulating foil and the space between the inner and outer shell is evacuated to minimize heat transfer. A dewar manufactured in this style can hold the liquid nitrogen under sampling conditions for roughly $8h$. Addition of molecular sieve pellets into the evacuated space, which are in thermal contact with the liquid nitrogen, increases
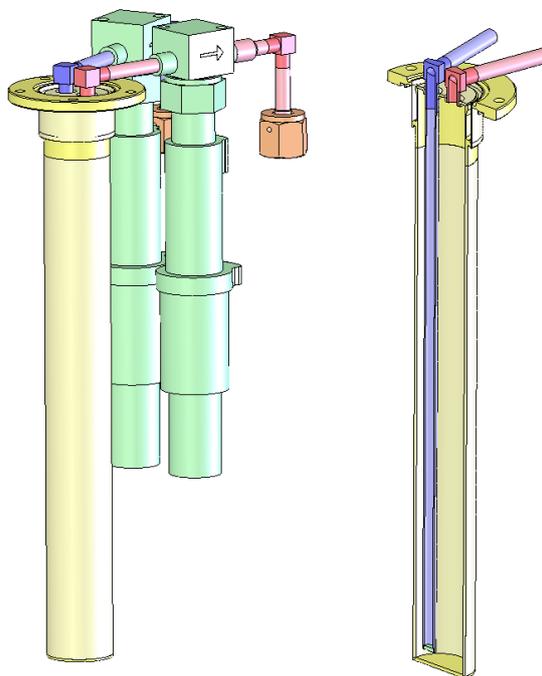
Figure 6.1 : *The left picture shows a schematic of a sampling trap, with electric motors attached to the valves (green). In the right picture, a cut shows the outlet stub and tubing. A frit is inserted into the end of the outlet stub inside the trap.*

the sampling time up to $20h$ because gases are efficiently removed and thus do not contribute to the heat transfer. The main dewar can be seen in figure 6.3.

Attached to the main dewar are two concentric rings of 0.25" tubes made out of electropolished stainless steel, acting as inlet and outlet manifolds. The sample containers can be attached to the lines by metal bellow (see figure 6.4). Both inlet and outlet manifolds can be closed by SS-4BG valves, which is important for keeping them clean during and after purging.

During purging, the inlet manifold has to be heated. Therefore, a total of $9m$ of heating wire $(5.65\Omega/m)$ was coiled around the inlet ring and the connecting stubs. By applying $\approx 2.4A$ from a transformator, the ring is heated to about $150C$. Though there remains a small unheated section between the valve of the sample container and the VCR connection to the stub, blanks have shown that this imposes no problem (see section 7.4.1 for details).

Figure 6.2 : *Sample container. At the top the VCR fittings and the valves can be seen. At the right, the flange by which the sample container can be attached to the sampling dewar is visible.*

6.3   Aircraft Sampler

For taking samples on aircrafts, the sampling system was built into an aluminium frame. Air flows through the aircraft inlet and connecting valves into a flexible stainless steel line. From a T-connection, a small fraction of the total air flow is directed through the sampling system, while most of the air flows back to the outlet. This way, a very high flow is purging the flexible steel lines all the time. All connection parts of the inlet/outlet system were designed to have at least KF16 dimensions in order to maximize flow.

The minor air flow is directed through the inlet manifold, where it is divided into the actual sample flow ($300ccm/min$) and a flow purging the inlet ring at all times ($250ccm/min$). The flow rates are controlled by mass flow controllers (MFC) (Analyt, GFC17). After the MFCs, the flows are recombined into a diaphragm valve pump (Vacuubrandt, MZ2D). The flow rates can be logged by a laptop computer, though this is not essential for the operation of the instrument.

6.4   Balloon Sampler

A dedicated sampling device has been built for balloon sampling. Here, additional problems are encountered because stratospheric air has only about $5ppm$

Figure 6.3 : *Main dewar with no sample containers attached.*

water vapor mixing ratio and stratospheric air has pressures less than $100 hPa$. Therefore, either a larger air flow than in the upper troposphere or a longer sampling time is required. However, the lower maximum pressure drop leads to a smaller available flow rate. As a first measure, no frits were inserted in the sample containers dedicated to balloon sampling. However, the flow is still very small, so that long sampling times have to be considered. In future projects, it might be necessary to change the tube diameter from 0.25" to at least 0.375".

In contrast to the airplane sampler, the balloon sampler is fully automated and can be controlled from the ground station.
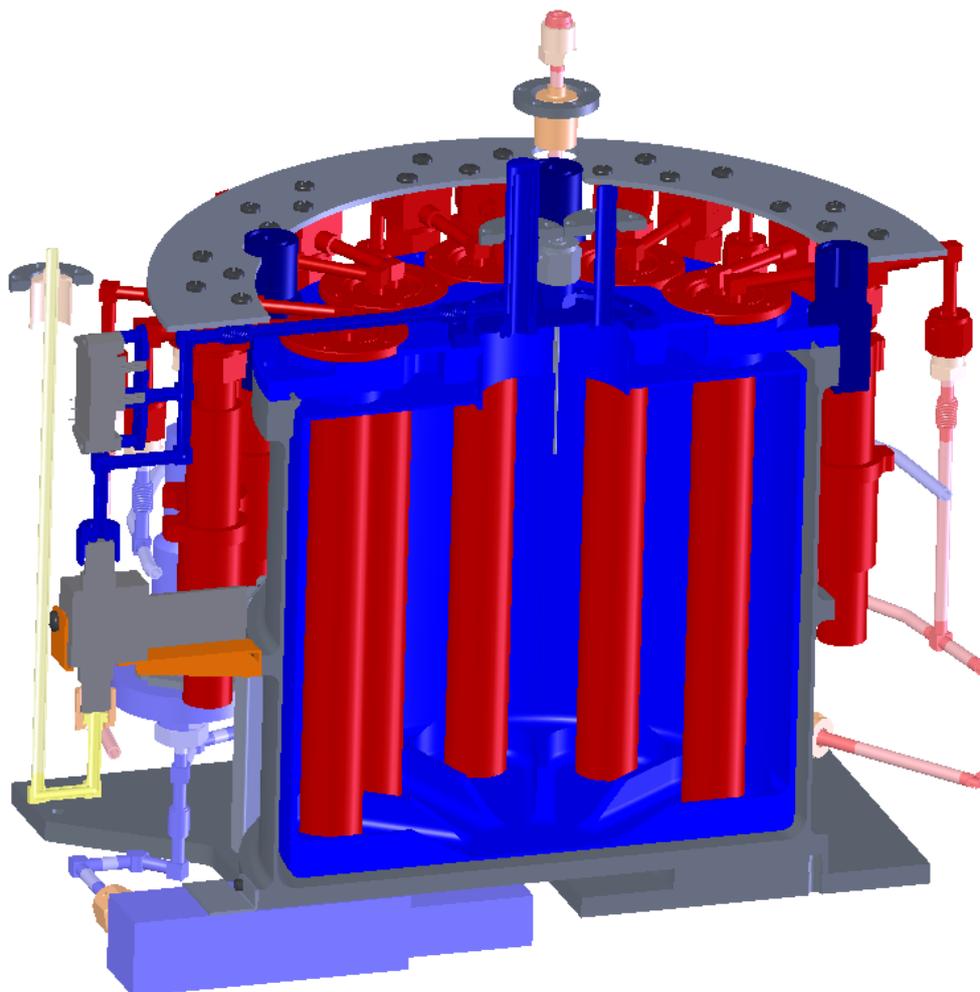
Figure 6.4 : *Cut through the main dewar and sample containers. The connection to the inlet and outlet rings can be seen. The blue main tank is filled with liquid nitrogen, which can evaporate through the blue top stubs.*
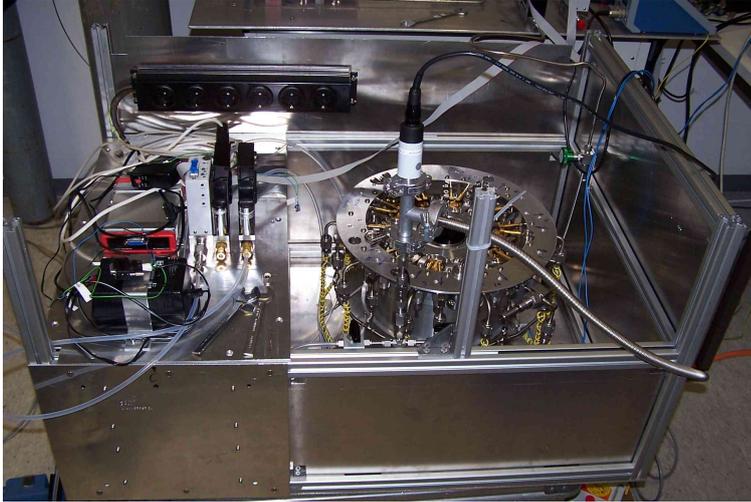
Figure 6.5 : *The whole airplane sampler unit with top lid and side panels removed.*

Figure 6.6 : *Balloon sampler. One can see the inlet and outlet manifolds with attached stubs and bellows. Further, the motors and couplings to the valves of the sample containers can be seen.*

Chapter 7

Calibration System for External Samples

The system described here can be used for the production of a humidified nitrogen gas stream with desired isotopic properties of H_2O. In principle, both hydrogen and oxygen isotopologues of H_2O can be produced and measured in order to obtain a calibration for the external sample containers. However, problems arose in the H_2-measurements with these external sample containers, which are thought to be caused by impurities by nitrogen-leftover in the traps. Such traces of nitrogen can lead to increased collisions in the mass spectrometer during H_2 analysis. This leads errors that can not be corrected easily. As a tight time schedule had to be kept, only oxygen isotope analysis was performed, so that also no calibration was available for the atmospheric measurements later on. However, it is believed that this issue can be addressed in the future.

7.1 Setup

In order to test the sampling system, a device had to be developed that is able to produce a gas stream with moisture conditions similar to the ones encountered in the UT/LS zone. The system described below is capable of producing a N_2 gas stream with known water vapor mixing ratios in the range of $\approx 5...60 ppm$. Further, the isotopic composition of the water vapor can be controlled in the range $\delta D = -440... - 140\%_0$ or $\delta^{18}O = -60... - 20\%_0$.

Figure 7.1 gives an overview of the setup. Nitrogen gas is first cleaned of all residual water vapor by a purifier capsule (SAES pure gas, MicroTorr PS11-MC1-N). The mass flow controller MFC1 (MKS, 1179AX53CS18V) provides the

main gas stream of $1200ccm/min$. Two additional mass flow controllers, MFC2 and MFC3 (MKS, 1179AX11CS18V) lead minor gas streams of $0...10ccm/min$ through two evaporizers, in which the gas bubbles through waters with known isotopic composition. After recombination with the main gas stream, a gas stream with controlled moisture has been created. CO_2 can be added to the gas stream via MFC5. A pressure controller (MKS, 640A13TW1M32M) guarantees that the pressure inside the system is constant at $1200hPa$. The mass flow controller MFC4 (MKS, 1179AX13CS1BV) regulates the flow into an attached sampling unit (see chapter 6 for details). All lines are of electropolished stainless steel $(1/4")$ in order to minimize surface memory water on the lines; only the ellbows connecting the evaporizers are of PFA.

The H_2O mixing ratio is controlled by the flow through MFC1, MFC2 and MFC3, the bath temperature, and the absolute pressure inside the system. Assuming the residual water vapor content through MFC1 is negligible, the mixing ratio is given by

$$v = \frac{E_l(T)}{P_{sys}} \cdot \frac{F_2 + F_3}{F_1 + F_2 + F_3} \qquad (7.1)$$

where $E_l(T)$ is the water vapor pressure (see equation 2.1), P_{sys} is the absolute pressure inside the system, and F_i denotes the flow through the different mass flow controllers.

In order to control the isotopic composition of the water vapor, the evaporizers were filled with $7.5g$ of two waters of different isotopic compositions: VOSTOK $(\delta D = -386.9‰, \delta^{18}O = -49.3‰)$ from melted Antarctic ice, and MPIK $(\delta D = -58.7‰, \delta^{18}O = -8.64‰)$ from demineralized tap water. The isotopic composition of the water vapor is calculated by equation 2.10 by inserting the fractions of the flows through MFC2 and MFC3:

$$\delta X_{vapor} = \frac{F_2 \cdot \delta X_2 + F_3 \cdot \delta X_3}{F_2 + F_3} \qquad (7.2)$$

For the calculation of δX_i, the isotopic composition of the water vapor in the evaporizers, the equilibrium fractionation factor α_{vl} (see equation 2.13) has to be taken into account:

$$\delta X_v = \frac{\delta X_l + 1}{\alpha} - 1 \qquad (7.3)$$

To avoid errors due to the temperature dependence of the fractionation factors and of the vapor pressure, the evaporizers are placed in a temperature controlled

bath (HAAKE, KT90W) at $7C$. At this temperature, $E_l = 10.02hPa$, $^2\alpha = 1.09558$ and $^{18}\alpha = 1.01100$. The temperature stability of the bath is usually better than $0.2C$; this results in errors of about 0.02‰ in $\delta^{18}O$ and 0.3‰ in δD.

7.2 Calibration versus Frostpoint Hygrometer

Due to the lack of an appropriate independent method, the isotopic vapor composition produced by the system described here can not be directly confirmed. Therefore, a mixing ratio calibration versus a frostpoint hygrometer was performed to check the dynamics of the system, and to draw conclusions for its isotopic vapor composition.

The frostpoint hygrometer in use was a dew point mirror 373LX from *MBW calibration*[1]. This hygrometer is capable of measuring frostpoints down to $-95C$, which is well below the typical conditions under which the system is used ($\approx -65C$ frostpoints). It is known for a very fast response time in the order of a few minutes in the $-65C$ range, though response at the lower temperature range increases to above 30 minutes.

In a frostpoint hygrometer, light is reflected by a temperature controlled mirror and its intensity measured. The temperature is controlled so that a constant thin film of ice is maintained on the mirror. The vapor mixing ratio of the gas stream over the mirror can then be calculated from the vapor pressure over ice ($E_s(T)$, equation 2.2) and the head pressure over the mirror.

7.2.1 System Blanks

In order to quantify the residual water vapor blank from the purifier, the valves leading to the evaporizers where closed and the mixing ratio monitored. It dropped below $0.06ppm$, which is an negligible amount as compared to the typical $50ppm$ used for filling sample containers.

Next, measurements were performed with opened valves of the evaporizers. If only one of the evaporizers was opened, the vapor mixing ratio was between $0.5...0.6ppm$. If both were opened, a mixing ratio of $1.0ppm$ was measured. It is therefore a valid assumption that both evaporators add a blank of $0.6ppm$ to the final gas stream. At a typical desired mixing ratio of $\approx 50ppm$, this leads to an impurity of $\approx 1\%$ in the gas stream. Thus errors in the isotopic composition of the vapor are in the order of 3‰ and 0.4‰ for δD and $\delta^{18}O$, respectively.

---

[1] the frostpoint hygrometer was borrowed from the FZ Karlsruhe, thanks to Ottmar Möhler

date	Hi Iso		Med Iso		Lo Iso	
	slope	intercept	slope	intercept	slope	intercept
12/05/2004	0.942	0.430	0.964	-0.079	0.996	0.368
13/05/2004	0.962	0.638	0.949	0.429	0.948	0.257
14/05/2004	0.970	0.272			0.944	0.546

Table 7.1 : *Slopes and intercepts for the different experiments. Hi Iso denotes full flow through the evaporizer with MPIK water, Lo Iso full flow through VOSTOK. Med Iso is half of the total flow going through each evaporizer.*

7.2.2   Linearity and Dynamical Behavior

To check for a linear correlation between the frostpoint hygrometer and the mixing ratios calculated from the electronic output of the mass flow and pressure controllers, experiments with varying mixing ratios were performed. The total flow $F = F_2 + F_3$ through MFC2 and MFC3 was adjusted so that mixing ratios between zero and a maximum of $75ppm$ were achieved. Figure 7.2 shows the response of the hygrometer to the targeted mixing ratios.

As one can see, the monitored signal follows the setpoints almost immediately, but the time needed to adjust and stabilize the signal depends largely at the mixing ratio. Lower mixing ratios need longer adjustment times, as only a limited amount of water vapor is able to lay a film of ice onto the mirror of the frostpoint hygrometer. At higher mixing ratios, the hygrometer's response time decreases significantly. Switching from $25ppm$ to $50ppm$ setpoints, the hygrometer's signal is within $1ppm$ of its final value after 2 minutes, and within $0.3ppm$ after approximately 5-6 minutes. Also, a little overshooting is visible which may be caused by the temperature control of the mirror.

Several of the experiments similar to the one shown in figure 7.2 were performed, either with full flow through one of the MFCs and zero through the other, or with each of them providing half of the total flow. For each run, slope and intercept were calculated and are summarized in table 7.1.

As there appears to be no difference in the slopes for the different experimental series, the mixing ratio of the humidified gas stream can be calculated using the mean slope and intercept of all these experiments:

	all slopes	all intercepts
$\bar{x}$	0.959	0.358
σ_{n-1}	0.018	0.218
n	8	8
$\sigma_{n-1}/\sqrt{n}$	0.006	0.077

As the system can produce stable and reproducable mixing ratios on demand through both evaporizers, it can be assumed that also the isotopic composition of the calibration gas can be calculated from the flow rates through the evaporizers. Indeed the following experiments show that also the isotopic setpoints are reproduceable. One remaining question is how fast the system reacts to setpoint changes, which will also be shown below.

7.3 Filling of Sample Containers

Figure 7.3 shows how sample containers are filled with the calibration system. The $500ccm/min$ flow from the calibration system is flowing through the inlet line to a pressure regulator (MKS, 640A13TW1M22M) that keeps the system at $400hPa$. From the inlet line, a small flow of $300ccm/min$ is let through the sample containers, the rest is used to purge lines and stub ends all time. The flow through the sample trap is regulated by a massflow controller (Analyt, GFC17, $2l/min$). The traps are immersed in the liquid nitrogen bath of the sampling unit that removes the water content from the nitrogen stream. During filling of the sample containers, a diaphragm pump (Vacuubrand, MZ-2D) is connected. After sampling, it is switched to a vaccum pump (Pfeiffer, DUO 2.5) for the evacuation of the sample containers.

7.4 Experimental Section

A number of tests were performed to demonstrate the capabilities of the described systems. First, blank experiments were performed to find a suitable procedure for purging the sampling system and the sample containers. A large number of samples was taken to perform a calibration. Also, the linearity of the system to both isotopic composition as well as sample amounts have been checked.

7.4.1 Blanks

Prior to taking the samples, the sampler's manifold was evacuated to $10^{-3}hPa$ for at least $12h$ while applying heat ($\approx 150C$) via a heating wire. To demonstrate that this method for cleaning the tubing system prior to sampling is sufficient, blanks were taken and analyzed. Five of the ten containers in the sampler were filled in the nitrogen stream while the valves of the evaporizers were kept closed in order to ensure that no water vapor was added to the gas stream. The

remaining five containers were not filled. After sampling, the first five and an additional three containers were evacuated over liquid nitrogen, while the other two containers were kept closed to check if there was any contamination left after purging the containers in the oven.

The first five containers showed small peak areas of typically $0.3Vs$, ranging from $0.1Vs$ to a maximum of $0.5Vs$. These peaks were so low that the mass spectrometer software had trouble of to define these peaks well. As compared with typical peak areas of $\approx 14Vs$, these background peaks are negligible.

The three containers which were not filled but evacuated showed no definable peaks at all, leading to the conclusion that the background peaks in the first five samples were either introduced by the nitrogen gas stream or a leftover from the purging process.

Of the last two blanks, one was unfortunately lost due to a handling error, but the other one also showed no measurable signal. Therefore the purging method to flush the containers at $250C$ for $20min$ with the MFC's valve fully opened appears to be sufficient to remove all traces of water vapor in the container.

7.4.2   Calibration

For the calibration of the system, the standard amount of $4.5l$ of gas was pumped through the sample containers at a flow rate of $300ml/min$ and $15min$ sampling time. The nitrogen gas was humidified with $48ppm$ water with isotopic composition of $(-31.9‰, -59.6‰)$ (*LowIso*) or $(-10.4‰, -19.6‰)$ (*HiIso*) for $\delta^{17}O$ and $\delta^{18}O$, respectively. This isotopic range is determined by the isotopic composition of the water in the evaporizers (VOSTOK and MPIK) and the bath temperature (see equation 7.2). This flow rate, sampling time and moisture result in a sample amount of $\approx 162\mu g$ of water.

CO_2 can strongly affect the results due to isotope exchange with H_2O. It is abundant in the stratosphere with mixing ratios of $350...370ppm$, which is much higher than the stratospheric mixing ratio of H_2O of $4...6ppm$. In order to distinguish between effects stemming from CO_2 in the gas stream and clean water samples, no CO_2 was admitted to the gas stream for the calibration runs. After sampling, the sample containers were evacuated to $10^{-3}hPa$ at liquid nitrogen temperature.

Figure 7.4 shows the results from these runs. Of the ten sample containers available, five were filled with LowIso. Afterwards, the isotopic content of the gas stream was changed to HiIso and another five samples were taken. This experiment was repeated three times (sa270604, sa010704 and sa040704). Afterwards,

the experiment was repeated twice with first filling five sample containers with HiIso and five with LowIso thereafter (sa070704 and sa100704).

As one can see, the system reacts quickly to switching from LowIso to HiIso. There is a small trailing effect in container 6 of about $2‰$ [2], but this within the precision of the stable signal. This small trailing effect might be caused by the CF-IRMS system, as the individual aliquots analyzed show a trailing effect towards a stable value.

However, switching from HiIso to LowIso seems to have a trailing effect on the the isotopic composition of the vapor. This is likely caused by the different lengths of tubing that connect the evaporizers to the main flow line. The evaporizer with HiIso has a longer connection line ($\approx 30cm$) than the one filled with LowIso ($\approx 10cm$). Therefore, it is likely that it will bleed out humidified gas longer than the LowIso humidifier.

The first datapoint of LowIso shows a small shift towards higher values. As this is the container to be analyzed first on a given day, this effect seems to stem from a tendency of the CF-IRMS system to shift towards higher values during night, most likely due to bleeding out oxygen containing molecules during night with an unknown isotopic composition. Therefore, the first datapoint should be ignored if it differs significantly from the rest.

Ignoring further the trailing datapoints in tubes 6 and 7 as shown in figure 7.4, steady state values were found from which a linear calibration can be made. Fitting the isotopic composition of the gas stream defined by equation 7.2 to the measured $\delta^{17}O_{ms}$ and $\delta^{18}O_{ms}$ values, the following parameters are obtained:

	slope		intercept	
	value	error	value	error
$\delta^{17}O$	1.55621	0.04859	3.81295	0.83134
$\delta^{18}O$	1.53697	0.04280	9.34795	1.44449

The errors of slopes and intercepts are due to the precision of the entire system. Therefore, the error of an individual sample can later be calculated using Gaussian error laws, resulting in errors of $(0.9‰...1.4‰, 1.7‰...2.4‰)$ for $(\delta^{17}O, \delta^{18}O)$ in the range of the calibration system $(-10.4‰... - 31.9‰, -19.6‰... - 59.6‰)$.

7.4.3 Separation of CO_2

As CO_2 is with $\approx 370ppm$ much more abundant in the UT/LS region than water vapor ($\approx 5...100ppm$), it is necessary to separate the CO_2 collected from the

---

[2] all numbers applying to $\delta^{18}O$, if not mentioned otherwise

water sample while the sample is still frozen in order to avoid isotopic exchange. Several experiments were performed in which dry ice or a dry ice/acetone mixture was used to increase the temperature in the sampler dewar to $-78C$. At this temperature, the vapor pressure of water is about $8 \cdot 10^{-3} hPa$. It was first assumed that evacuating the sample containers with a rotary vane pump with a maximum vacuum of $10^{-3} hPa$ would not influence the sample as at this temperature the vapor pressure also builds up very slowly, hence pumping on it shortly would not remove too much sample. However, using this evacuation method, all samples displayed a significant positive shift (roughly $4‰$), thus clearly displaying Rayleigh distillation effects.

In order to avoid this distillation effect, the temperature was lowered to less than $-94.8C$ by using a frozen acetone mixture. While there was still liquid nitrogen left in the sampling dewar, it was filled with $2.5l$ of acetone. On demand, more liquid nitrogen was added to maintain frozen acetone ice. The temperature of this ice was monitored, and evacuation of the sample containers was performed while the temperature was between $-94.8C$ and $-120C$. In this temperature range, the vapor pressure of water is less than $0.4 \cdot 10^{-3} hPa$ and the vapor pressure of CO_2 is well above $1hPa$. As a further precaution against distillation effects, the pressure of the sample container was monitored and the container was closed as soon as the pressured dropped below $5 \cdot 10^{-3} hPa$.

Figure 7.5 shows results from measurements performed under the same conditions as the calibration run. The effects already mentioned - the shift towards high values in the first sample and the trailing effect in container 6 - is also seen here. The remaining samples are in agreement with the CO_2-free samples measured before, so that this CO_2 separation scheme was applied for future samples containing carbon dioxide.

7.4.4   Linearity

In order to test the linearity of the system versus the isotopic composition of the sample water, one run (sa240704) was performed with the first three sample containers at $\delta^{18}O = -59.6‰$, five samples with $-39.6‰$ and two with $-19.6‰$. The results are shown in figure 7.6.

Samples 1, 4 and 9 display the memory effects as already mentioned above. However, the other samples are within the 2σ errors given by the calibration. Therefore, linearity within the isotopic range tested can be assumed.

7.4.5 Retrieval of Mixing Ratio

A measure for the amount of a sample can be derived from the integrated signal intensity of the mass spectrometer, the peak area. However, a difficulty arises as the peak area decays approximately exponentially with time, as aliquot after aliquot is flushed out the sample container and the freshly incoming helium dilutes the mixing ratio of the sample container. Therefore, an exponential decay function is fitted on the peak area of the aliquots, and the amplitude at $t = 0$ is taken as the peak area value for a given sample (see also section 5.4).

Figure 7.7 shows the mixing ratio of a sample as a function of the peak area. The mixing ratio of the calibration system was fixed at $48ppm$ during all experiments to avoid longtime trailing effects and the flow through the calibration traps was kept constant at $300ccm/min$. The sample amount is changed by varying the sampling time. The standard sampling time was $15min$, and was varied during one experiment from $4...30min$ (see section 7.4.6). Signal linearity can be certified from this additional data, and the mixing ratio can be calculated from peak area (A) and volume sampled (V). Since the zero-point is well defined by the absence of system blanks, only the slope needs to be fitted onto the data:

$$v = (3.55 \pm 0.70)\frac{ppm}{Vs} \cdot A \cdot \frac{4.5l}{V} \qquad (7.4)$$

7.4.6 Signal Linearity

One crucial requirement for the system developed is that the measured values may not strongly depend on the amount of water in the sample container. While the mixing ratio of water vapor in the stratosphere is known to vary from about roughly $4...7ppm$, in the tropopause region variations from roughly $4...100ppm$ are possible. If sampling time and air flow are constant, huge variations in the sample amount can occur. At a later stage, the sample amount could be controlled by using a hygrometer together with the sampler during a sampling flight. However, at this stage of the project, no hygrometer was available.

To test signal linearity, a series of experiment was performed (sa220704), in which the sampling time was varied while air flow and moisture of the nitrogen stream were kept constant ($48ppm$, $\delta^{17}O = -31.9‰$, $\delta^{18}O = -59.6‰$). Three sample containers (tubes 1,2 and 3) were filled for the standard sampling time of $15min$, 2 containers (4,5) for $7.5min$, 3 containers (6,7 and 8) for $30min$ and the remaining containers (9,10) for only $4min$. Container 10 was lost due to a handling error. The results are displayed in figure 7.8. The measurements with peak areas less than $10Vs$ are just outside the 2σ error stemming from the

calibration. Thus it is likely that the error increases somewhat at lower peak areas.

7.4.7   Memory effects

The combined apparatus of analytical system, calibration line and sample containers displays memory effects, which can either be addressed by conditioning or by including the effects into the individual error of a sample.

The memory effect of the sample containers can be estimated using the data obtained from the calibration (figure 7.4). In all five sample runs, the measured value for each container reaches a stable value immediately, so there is no trend visible after the isotopic setpoints were switched. This means that the amount of memory water or surface oxygen in the sample traps is negligible.

As has been mentioned above, the calibration system itself produces memory effects (the datapoints marked as trailers in figure 7.4), probably caused by slow mixing or bleeding from the evaporizers. These effects therefore need not to be considered when taking atmospheric samples.

The analytical system itself displays two kinds of memory effects. The first is displayed in the first measured sample of the day, which appears to have a trend towards high δ-values. As it is hard to quantify this effect - it may depend on the down time of the system - it is recommended to condition the CoF_3 prior to the measurement of atmospheric samples by injecting and measuring a water sample with low isotopic composition (e.g. SLAP) from the calibration trap.

The second memory effect of the analytical system happens when switching between samples with different isotopic composition. A problem here is that this effect is masked by the trailing effect of the calibration line in most experiments performed. However, it can be seen in figures 7.4 and 7.5 that under ideal conditions (i.e. by flushing the calibration line after switching the isotopic composition setpoint prior to taking the next sample) the effect is quite small. An estimation for the size of the effect can be obtained by the data in figure 7.5, where the sample in container 16 has $\delta^{18}O = -23.8\text{‰}$. The isotopic setpoints are -59.6‰ and -19.6‰, so that the memory effect of container 16 is $\approx 10\%$. For the calculation of the individual error of an atmospheric sample it is therefore assumed that it might be influenced by no more than 10% by the last sample.

7.4.8 Capability to Measure MIF Samples

As one can clearly see in the datasets above, $\delta^{17}O$ and $\delta^{18}O$ appear to be closely correlated. It is therefore of interest, to which accuracy a mass independently fractionated sample can be measured.

In Figure 7.9, the data from samples sa200704, sa220704 and sa240704 $\ln(1 + \delta^{17}O)$ was plotted versus $\ln(1+\delta^{18}O)$. As explained in section 2.3.5, the samples should lie on a line of slope 0.528. Indeed, a line fitted on the data gives the slope 0.522 ± 0.004, which is in good agreement with 0.528 within the error.

Further, Δ^{17} (equation 2.27) was calculated for the datapoints in figure 7.9, resulting in a mean of $0.06‰$ and a standard deviation of $0.35‰$.
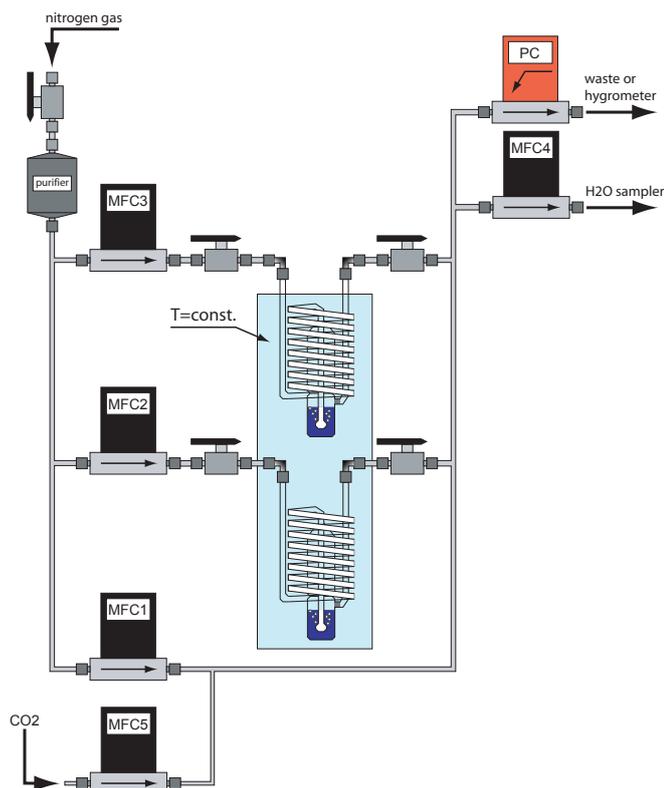
Figure 7.1 : *Schematics of the calibration system. The purified N_2 gas stream is split into two gas streams (range $0...10ccm/min$) going through evaporizers filled with waters of known isotopic composition, and the main gas stream, $1200ccm/min$, controlled by MFC1. The gas streams recombine after the evaporizers with known moisture and isotopic composition. The Pressure controller regulates the pressure inside the system. MFC4 emits gas into a connected sampling system.*
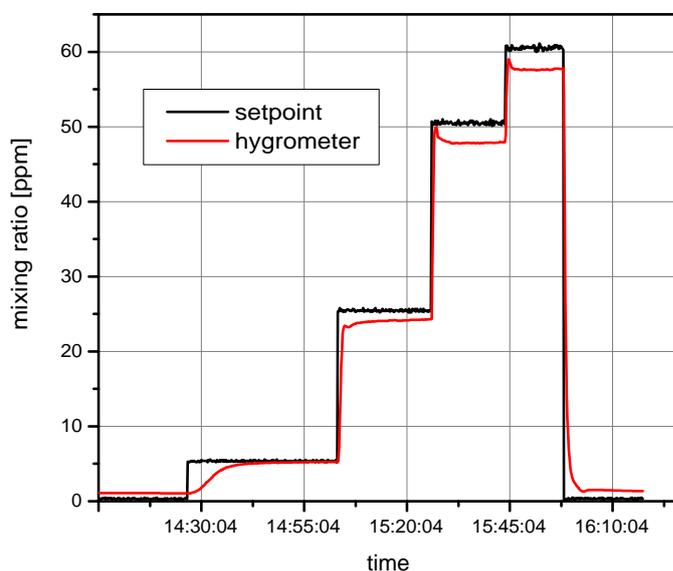
Figure 7.2 : *Targeted (setpoint) and measured (hygrometer) H_2O mixing ratios. The frostpoint hygrometer follows the setpoint with a response time that increases at lower mixing ratios. Also a minor overshooting occurs after changing the humidity setpoint, which is probably due to a temperature oscillation in the mirror of the hygrometer.*
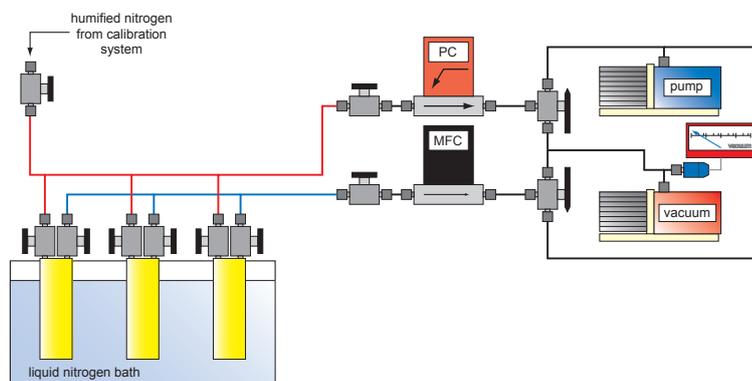
Figure 7.3 : *Setup for filling of external sample containers. The inlet line is shown in red, the outlet line in blue. The diaphragm pump (blue) is used during filling when a flow rate of $500 ccm/min$ is processed. It can be switched to a rotary pump (red) via 2-way valves for the evacuation of sample containers. Only three of the ten possible sample containers are shown.*
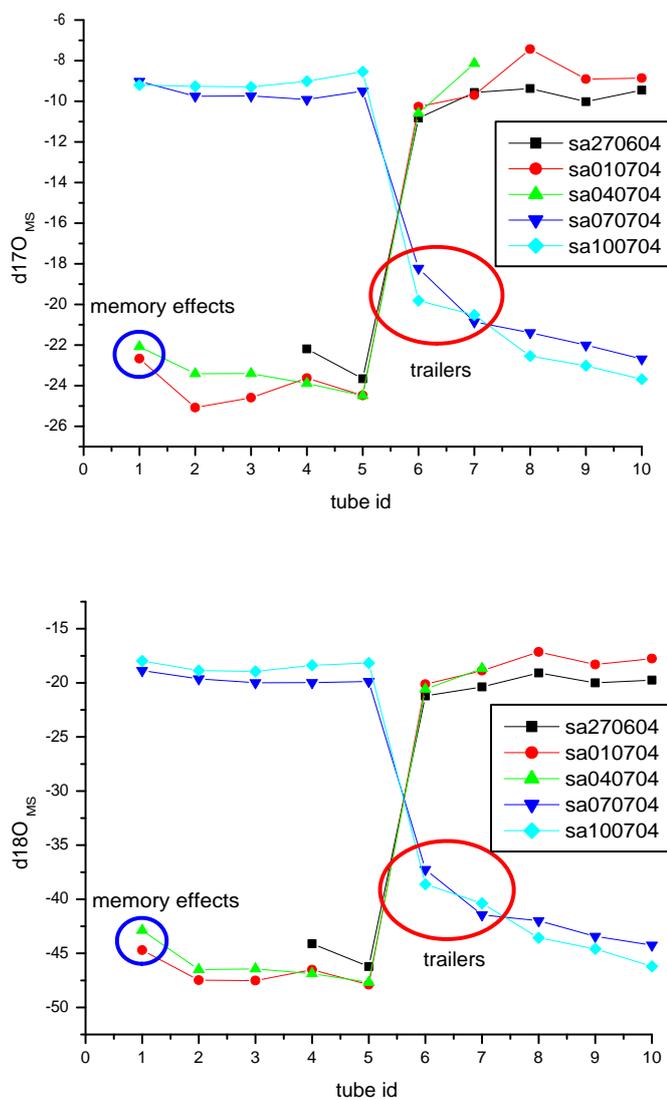
Figure 7.4 : *Calibration data for $\delta^{17}O$ and $\delta^{18}O$ of the system. Shown are the calculated values $\delta^{17}O_{ms}$ and $\delta^{18}O_{ms}$ as explained in section 5.5 versus the tube identity number, which coincides with the series in which the samples were taken.*
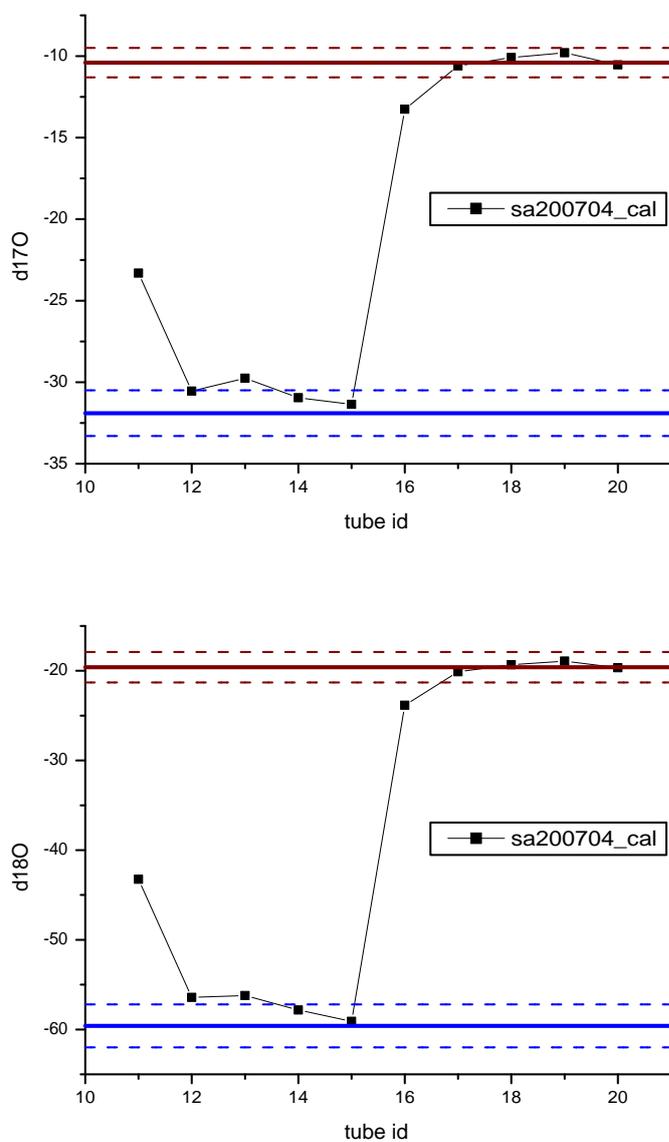
Figure 7.5 : *Sample run with added CO_2 and subsequent separation over acetone ice. Also shown are setpoint values and expected errors (dashed lines, 1σ) applying to the calibration. Though memory and trailing effects are visible (tube 1 and 6), the steady state values agree well with the set values.*
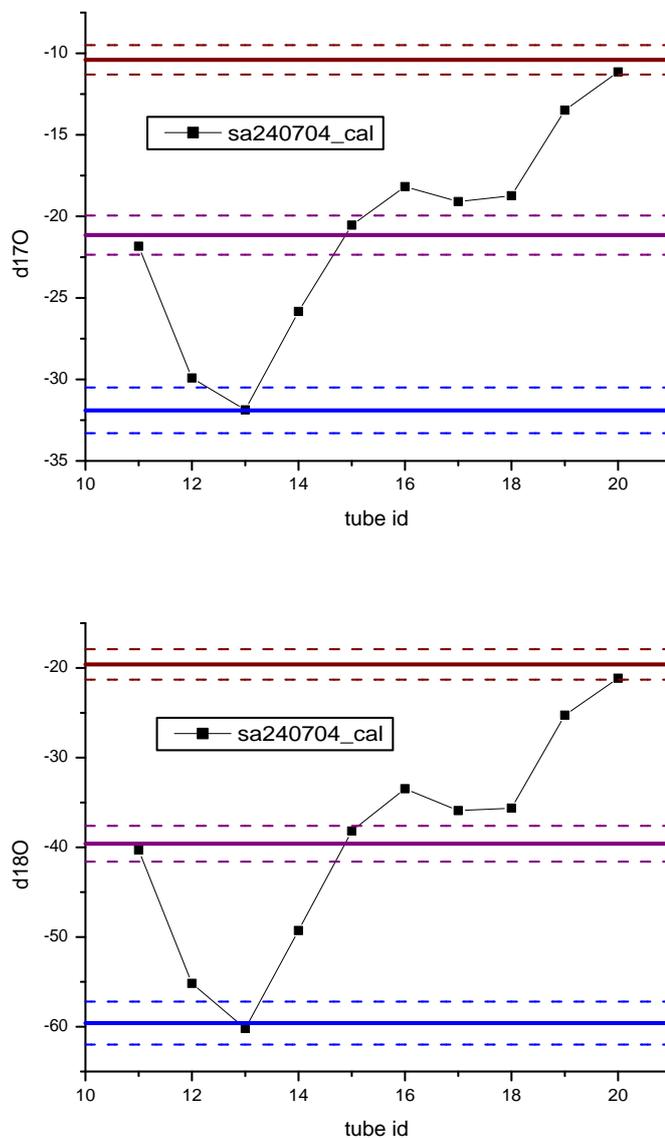
Figure 7.6 : *Linearity test versus the isotopic composition of the samples. The sample containers were filled with three different isotopic water vapors. Neglecting the trailing effects displayed in tube 1,4 and 9, the remaining samples are within the 2σ errors as given by the calibration (1σ errors displayed by the dashed lines).*
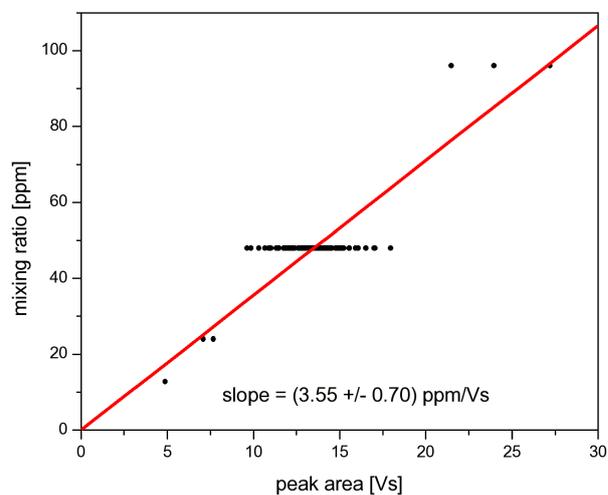
Figure 7.7 : *Mixing ratio as a function of the integrated peak area of the mass spectrometer.*
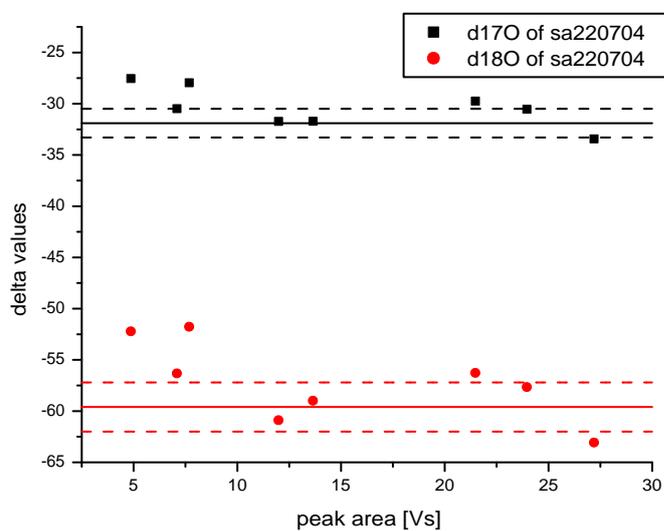
Figure 7.8 : *Delta values plotted versus area of the sample peak. No dependency of the deltas on the sample amount is thought to be seen, though the scatter increases at low peak areas.*
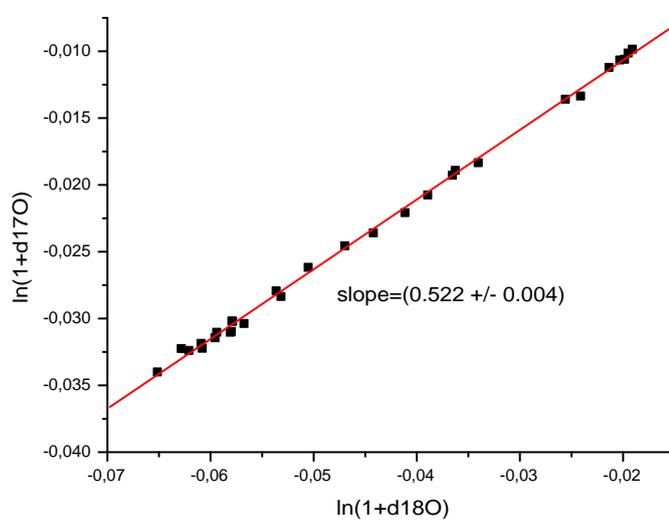
Figure 7.9 : $\ln(1+\delta^{17}O)$ *plotted versus* $\ln(1+\delta^{18}O)$. *The data is taken from samples sa200704, sa220704 and sa240704. The correlation line has a slope of* 0.522 ± 0.004, *which is within* 2σ *error in agreement with the expected* 0.528. *No datapoints from the calibration are included in this plot, as this would artificially draw the correlation line to a slope of* 0.528.

Chapter 8

Experiments with the HTO Sampler

In addition to the experiments with the stable isotope sampling gear, measurements with an aircraft HTO-sampler have been performed. This sampling gear has been described in detail elsewhere [Franz, 2002], so that only its main features will be explained here.

The principal idea of this device is to collect water vapor on a drying agent (molecular sieve), and extract and analyze it later in a laboratory. Early experiments with various drying agents were performed by Soyez [1999]. Molecular sieves are generally applicable to the measurements of HTO and HDO, whereas they show oxygen isotope exchange effects.

8.1 Technical Features of the HTO Sampler

The sample containers are stainless steel tubes of $275mm$ length and $40mm$ inner diameter, closed on each end with $SS-43S6$ *Swagelok* valves with 3/8" connecting tubes. The tubes are filled with $\approx 250g$ molecular sieve $5\mathring{A}$. Steel sieves are inserted at the end of the tubes to prevent the molecular sieve to leave the tubes. The estimated efficiency at a flow of $F = 50l/min$ (STP) is around 99% [Franz, 2002]. Overall, 18 tubes were built.

A major disadvantage of these tubes is that they offer a big flow resistance, and thus conventional pumps can not deliver a sufficiently large flow at low pressures. As a solution, a supercharger usually used in the automobile industry (*EATON M62*) was used as a pump. It's limitation is its maximum compression ratio of $1:2$, so that at $300hPa$ outside pressure it's maximum flow rate is $420l/min$

(STP). In these experiments, the pressure drop on the sample tubes is larger than $150hPa$, so that a maximum flow of only $\approx 25l/min$ through the tubes is possible. However, during purging of the aircraft's inlet lines, the full flow can be expected.

The rack containing the sampler also holds pressure and mass flow sensors. The tubing allows a huge bypass flow through the main inlet line of the aircraft, and a minor flow through a bypass parallel to the inserted sample tube.

In the laboratory, the water vapor is removed from the molecular sieve by heating the sample tubes to $400C$ for about $23h$ in a $250ml/min$ stream of clean nitrogen gas at $\approx 300hPa$. The water vapor is frozen into a glass trap at $-75C$. After collecting the water vapor in this trap, it is evacuated, sealed, and the water is transfered into a small glass finger by heating the trap to $300C$ and cooling the finger to $-75C$ for $\approx 15min$. From here it is weighed, transfered into an autosampler vial with a μl-pipette and finally analyzed [1].

8.2 Calibration

As described in Franz [2002], the system needs to be calibrated, as the extracted water is influenced by memory water and other effects. However, the correction procedure described here differs from the one in Franz [2002], as the system showed a different characteristic. The main difference might be caused by an undetected leak in the previous system, that adds water vapor from ambient air to the sample water. This does not automatically mean that the measurements in Franz [2002] are wrong, as the leak was then automatically included into the calibration scheme.

Already in the measurements of Franz [2002] it was visible that the precision for δD-measurements using molecular sieves is quite low - in the experiments below it is about $\pm 46‰$. However, mass spectrometrical analysis of δD is easier than tritium analysis in a scintillation counter. Therefore the calibration procedure was performed with waters of known δD and $\approx 0TU$. In the subsequent atmospheric measurements, emphasis is given on the tritium analysis with the parameters obtained from this deuterium calibration.

Filling the sample tubes in an actual stream of air is quite difficult to achieve, as even the turbocharger used could not be run under laboratory conditions to provide the necessary flow rate. As it has only a compression ratio of $1:2$, one

---

[1]Analysis was carried out by the Institute for Environmental Physics (IUP) of the University of Heidelberg. My thanks go to Ingeborg Levin and Christel Facklam for deuterium analysis and to Reinhold Bayer for the tritium analysis
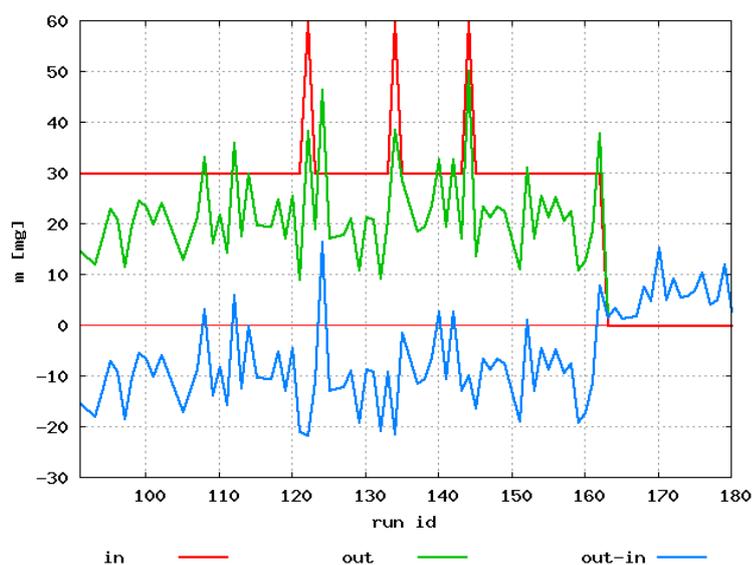
Figure 8.1 : *Mass balance of the laboratory samples. In general, m_{out} is smaller than m_{in}. Also, a blank is visible. This suggests that the extracted water is a mixture of a blank and a fraction of the original sample water.*

would needsa multistage of several compressors to get a flow rate of $25l/min$ at $300hPa$ inlet pressure. However, as the calculated efficiency of the sample tubes is $\approx 99\%$ and fractionation during the sampling process is assumed to be negligibly small, another scheme was applied.

The sample tubes were filled with $30mg$ of water with known isotopic composition (MET with $\delta D = -0.15\permil$, and GREENLAND with $\delta D = -281\permil$). The water was placed into a blind plug connected to the closed sample container. After heating the blind plug with a heat gun, the valve of the sample container was opened and the water vapor released into the sample tube. Leaving the blind plug on the tube, the valve was kept open for about $24h$ to ensure complete transfer of the water into the sample tube.

Figure 8.1 shows the mass balance for all sample containers. The extracted mass is generally lower than the input. This can be explained by destruction of H_2O in the molecular sieves, i.e. by integrating H_2O into its crystal structure. Some of this water may again be released, as can be seen when no H_2O was put in (run id 163-180). Therefore, one is left with the tasks of finding an average value for the mass and isotopic composition of the blank, as well as the average extraction efficiency.

An estimate for the blank can be obtained from runs 163-180, where there was no
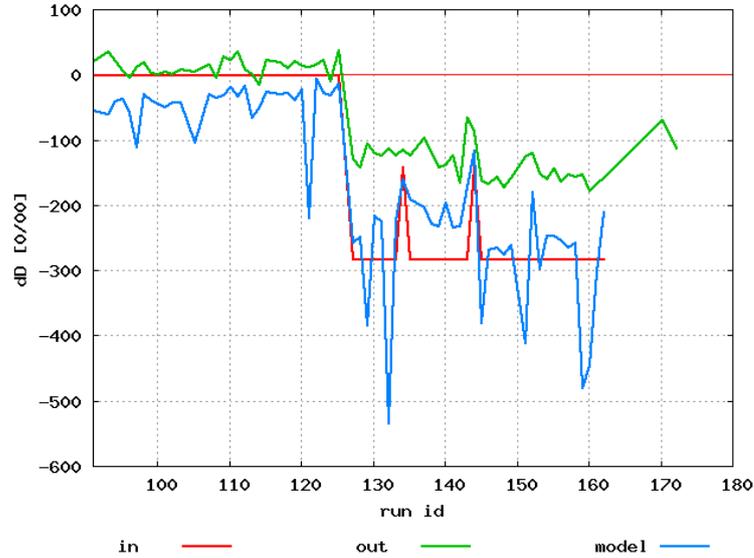
Figure 8.2 : *Isotopic composition of the laboratory samples. The difference between δD_{in} and δD_{out} is larger for lighter samples, which can be explained by the isotopic composition of the blank. The reconstructed δD_{model} mimics the main features of the input. The larger spikes with $\delta D_{model} < -350‰$ is caused by too small $m_{out} < 15mg$.*

water input, yielding a mean of $m_{blank} = 5.8mg$ and standard deviation $3.9mg$. Subtracting this value from the measured output mass and dividing through the input mass gives an average extraction efficiency of mean $\eta = 0.6$ and standard deviation 0.2.

Figure 8.2 shows the isotopic composition of the input and extracted water. The difference between extracted and input water is larger at lower isotopic levels, indicating that the blank has $\delta D_{blank} > 0‰$. Its actual isotopic composition can be calculated from making an isotopic mass balance for each sample, resulting in a mean of $\delta D_{blank} = 138‰$.

δD_{in} of the input water can be calculated as

$$\delta D_{in} = \frac{\delta D_{out} - \left(1 - \frac{m_{out} - m_{blank}}{m_{out}}\right) \cdot \delta D_{blank}}{\frac{m_{out} - m_{blank}}{m_{out}}} \tag{8.1}$$

Using this calibration, a reconstruction of δD of each measurement has been obtained. δD_{model} is shown in figure 8.2. Especially for samples $m_{out} < 14mg$, it differs significantly from the actual input water - these are the spikes below $-350‰$. However, this is a criterion easily controlled for rejecting samples. The

difference $\delta D_{in} - \delta D_{out}$ has a standard deviation of 46‰ if all samples below $m_{out} = 15mg$ are rejected.

For the retrieval of ^3R the following equation can be used, whereby an isotopic composition of $^3R_{blank} = 5TU$ is assumed - a value typical for surface waters:

$$^3R_{in} = \frac{^3R_{out} - \frac{m_{out}-m_{blank}}{m_{out}} \cdot ^3R_{blank}}{\frac{m_{out}-m_{blank}}{m_{out}}} \tag{8.2}$$

For the calculation of the HTO mixing ratio ς, the volume V of the sampled air has to be known. The mixing ratio can then be calculated using $\eta = 0.6$ from the calculation above:

$$\varsigma_{in} = \frac{m_{out} - m_{blank}}{\eta \cdot M_{H_2O}} \cdot ^3R_{in} \cdot N_A \cdot \frac{V_{STP}}{V \cdot M_{air}} \tag{8.3}$$

Due to the errors in m_{blank} and η, the error in ς is approximately 30%.

Overall, the precision of the HTO sampler is sufficient to allow the investigation of PSC particle sedimentation via increased tritium levels in the tropopause region. As shown in section 3.2.4, a 10% sedimentation of the PSC layer into the tropopause layer doubles the HTO mixing ratio encountered. This is the minimum that can be resolved with this apparatus. However, the precision of δD is not really sufficient for detailed analysis of atmospheric processes, so that δD of later atmospheric samples will not be discussed.

Chapter 9

Atmospheric Measurements

Using the analytical equipment described in the previous chapters, the first isotope measurements on upper tropospheric and stratospheric water vapor were made on samples collected on aircraft flights between New Zealand and Antarctica. The aircraft, a *C-17 Globemaster*, operates as a transporter for staff and equipment for the Antarctic observatories McMurdo and Scott Base. These aircraft are not designed for, but are frequently used for scientific experiments.

The sampling region was chosen for two main reasons. First, the tropopause level is located at lower altitudes near the poles, and thus it is possible to sample stratospheric air without making use of special high altitude aircraft. Second, one of the main goals of the work presented here was to quantify the Δ^{17} anomaly in stratospheric water vapor. As global circulation results in downward flux of stratospheric air at high latitudes, the probability to find an isotope anomaly is higher near the poles.

Overall, six flights were performed; two in August 2003 collecting HTO samples with the molecular sieve sampling unit, and two each in August and October 2004 using the new cryogenic sampler for the stable water isotopologues. The sample inlet was connected to the hull of the aircraft, with its inlet/outlet slits located at a minimum distance of $\approx 15cm$ from the aircraft hull and before the wing and engines. Since this is not a scientific flight, navigational data was not measured online and so data written down by the aircraft crew at intervals of $\approx 30min$ has to be used. From this data the position, temperature and altitude of the samples collected are interpolated. As the airplane is kept at a stable level through most of the flight, these interpolations are sufficiently accurate.

The tropopause heights are derived from potential vorticity plots received from the *NASA Goddard Automailer*, which are available every $24h$. Due to limited

resolution, the error in in locating the tropopause at $-1.6PVU$ is estimated at $800m$.

9.1   Oxygen Isotopes

Samples for the analysis of $\delta^{17}O$ and $\delta^{18}O$ were taken during flights on August 21 and 25, and October 13 and 14 of 2004; exact dates, times, positions etc of the individual samples are given in appendix A. Overall, 38 samples and 2 blanks were taken. The blanks were processed exactly like the samples (purging, heating, evacuating, freezing and transport). All samples were analyzed within 3 weeks after sampling to avoid chemical alteration in the sample containers as much as possible. Analysis was carried out as described in chapter 7, and the data given here is obtained by applying the calibration from section 7.4.2.

To avoid contamination with surface water from the inlet tube or the $3.5m$ long flexible stainless steel line connecting the inlet to the sampler, the inlet line was flushed $30min$ prior to sampling. The purge flow of $> 100l/min$ (STP) provided by the dynamic forward pressure of the aircraft was maintained during the whole sampling process. Additionally, the inlet line had been flushed with dry nitrogen gas one day prior to each flight to remove surface water. These measures were taken to assure that the smaller air flow of $550ml/min$ (sample plus bypass flow) taken from the main flow into the sampler was free from surface contamination as far as possible.

The errors stated for $\delta^{17}O$ and $\delta^{18}O$ originate from three sources: 1) from the calibration itself, 2) from memory effect considerations and 3) from the two blanks taken. The errors of these sources are added quadratically, following Gaussian error calculation. The errors of the calibration are discussed in section 7.4.2. For the memory effects, a constant 10% of the difference between the measured sample and its predecessor is assumed (see section 7.4.7).

The blank taken in August showed a $0.5Vs$ background signal. This introduces only a minor error into most of the measurements. A check of the analytical system revealed a minor blockage in one line, so that purging the sample containers prior to sampling in August had been less effective than it had been during the calibration. As repairing the lines was not an option (it might have affected the calibration), the sample containers were additionally evacuated after the purging procedure and refilled with helium after the measurement process. The blank taken in October hence was negligibly small (only $4mV$ high on mass 32), so that the line blockage can be identified as the source for the first background blank. To consider the blank in the samples taken in August, it is assumed

that its isotopic composition stems from filling the containers via the calibration system, and the error is calculated accordingly with its isotopic range (i.e. $\delta^{18}O_{min} = -59.6$‰, $\delta^{18}O_{max} = -19.6$‰, see section 7.4.2).

The combined errors are usually less than 2.5‰ and 5.0‰ for $\delta^{17}O$ and $\delta^{18}O$, respectively. Only the combination of small sample amount and high blank results in higher errors; one datapoint has been removed in the plots shown below for this reason. The individual errors come to approximately same parts from the calibration and the high blank in the measurements of August, whereas memory effects play only a minor role. As the blank is zero in the October measurements, approximately two thirds of the error in these data come from the calibration, and one third from memory considerations.

9.1.1 Results

The mixing ratio of the samples can be calculated from the peak area in the mass spectrometer and the amount of air sampled (equation 7.4). The air volume is accurately measured by the mass flow conroller with 2% precision. The main error therefore stems from the 20% uncertainty in the slope of the calibration.

In figure 9.1 the mixing ratio is plotted versus ambient temperature. For air crossing the tropopause from the troposphere, the tropopause cold point determines the last point at which condensation can occur. Therefore, a correlation between tropopause temperature and mixing ratio can be expected at tropopause level or below. Such a dependence, though with a high scatter, is seen for samples with $\upsilon > 10ppm$ in figure 9.1. Neglecting the outlier at $-41C$, a gradient of $\approx 4ppm/C$ is found.

Air above the tropopause cold point is subject to temperature changes without additional condensation events, so that water vapor above the cold point has already lost some of its temperature history. Therefore, the correlation between the the mixing ratio of water vapor and temperature is lost in the stratosphere, and the scatter of a plot versus temperature above tropopause level increases, and is further enhanced by mixing with stratospheric air [Zahn et al., 1998]. Since there is no correlation between ambient temperature and mixing ratio in the data for $\upsilon < 10ppm$, samples below $10ppm$ are from hereon classified as "stratospheric", whereby samples with mixing ratios above $10ppm$ are labeled "tropopause", i.e. to be strongly influenced by the tropopause temperature. More accurately, the "stratospheric" samples stem from the lowermost stratosphere. Only three samples of the first flight in August belong to the stratospheric dataset. These three samples all were taken at latitudes of 65 degrees south and higher, where the
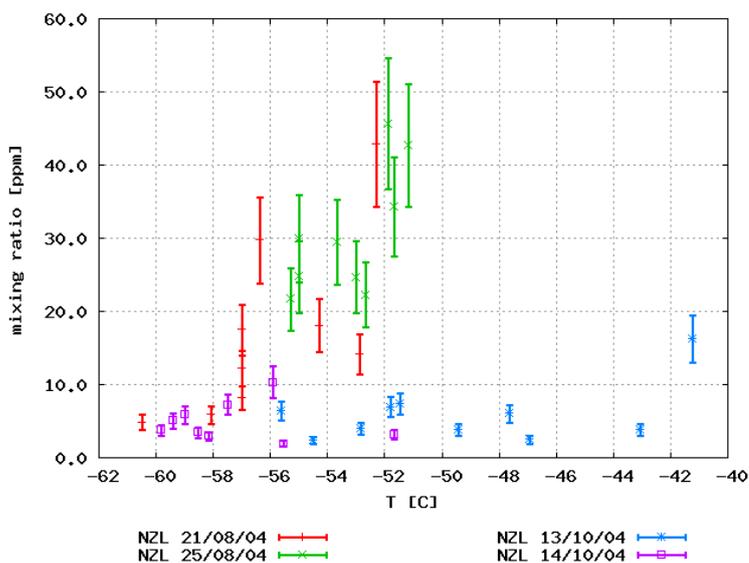
Figure 9.1 : H_2O-mixing ratio plotted versus ambient temperature. The samples can clearly be separated into stratospheric samples with $v < 10ppm$, and samples strongly influenced by the tropopause, which still show a temperature dependence.

tropopause is located at lower altitudes. No samples of the second flight in August are classified to belong to the stratospheric subset.

Figure 9.2 shows the measured H_2O mixing ratios plotted versus the distance to the tropopause. The tropopause samples show a scatter between $10...50ppm$, though no dependence on the distance to the tropopause is seen. The stratospheric samples show a decrease in mixing ratio with increasing distance to the tropopause, until pure stratospheric mixing ratios are encountered. Some of the datapoints actually reach mixing ratios below the typical stratospheric range of $\approx 4...6ppm$. Since the difference is statistically significant, the stratospheric air could have undergone partial dehydration, or could have mixed with the dehydrated polar vortex. Especially the samples taken in October are very dry, whereas the stratospheric samples taken in August all have $v \geq 5ppm$. Thus the October samples are likely to contain air from the dehydrated stratosphere, where such low mixing ratios have been observed (e.g. SAGE-II, Chiou et al. [1997], data for SON; HALOE, H_2O data at http://haloedata.larc.nasa.gov/).

To investigate the possibility of condensation leading to the decrease of water vapor mixing ratio, the relative humidity of the samples is plotted versus the distance to the tropopause in figure 9.3. For the calculation of relative humidity, the mixing ratio and the pressure at sample altitude have to be known. However,
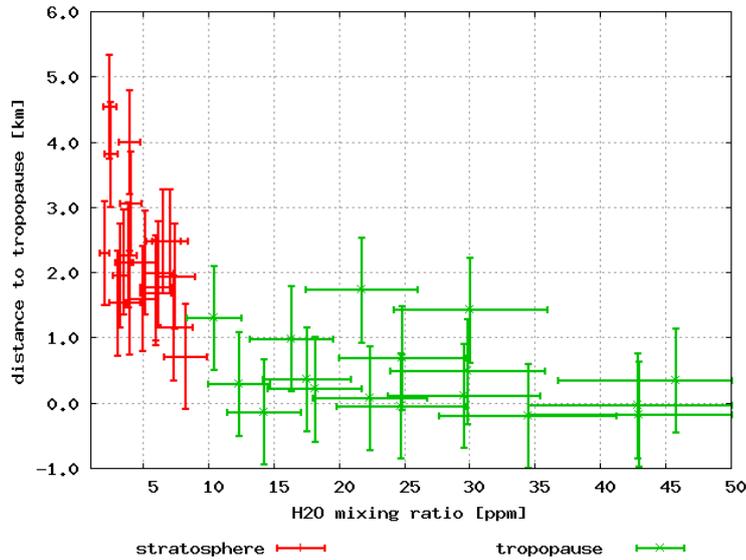
Figure 9.2 : *H_2O-mixing ratio plotted versus distance to the tropopause. A decrease in mixing ratio with increasing distance to the tropopause is visible, which can be explained by mixing of relative moist air from the tropopause cold point with drier stratospheric air from above.*

there is no pressure data available on the C-17 flights, as its navigation solely depends on the global positioning system (GPS). The pressure is calculated from the GPS-altitude, assuming a scale height of $H = 8.0 \pm 0.5km$. The relative humidity can be calculated from the altitude z, the mixing ratio v and the vapor pressure over ice E_s at the ambient temperature T:

$$f = \frac{v \cdot 1023hPa \cdot \exp(-z/H)}{E_s(T)} \cdot 100\% \tag{9.1}$$

The error of f stems from the error of the mixing ratio of 20%, and an assumed error of 7% from the estimation of H, so that $\Delta f/f$ has a total error of 21% by quadratic addition.

Relative humidity is below 60% for all samples. Furthermore, a decrease in relative humidity with increasing distance to the tropopause is evident, so that a condensation process can be ruled out. Therefore the decreasing mixing ratio of water vapor over the tropopause is due to mixing with dry stratospheric air.

In figure 9.4, $\delta^{18}O$ is plotted versus sampling altitude. $\delta^{18}O$ spans a range of $\approx -90... -25‰$, with a mean of $-56‰$ and standard deviation of $17‰$. A clear dependence on altitude is not seen in the plot, which implies that the mixing
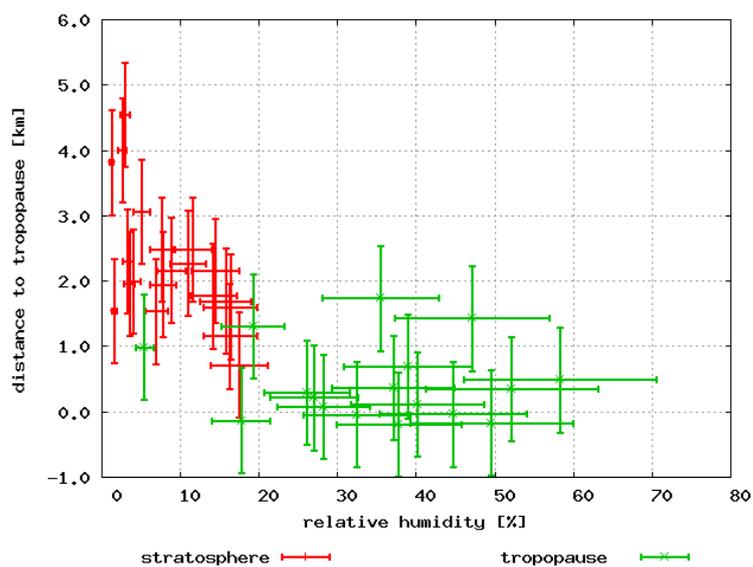
Figure 9.3 : *Relative Humidity plotted versus distance to the tropopause. As the relative humidity decreases with distance above the tropopause, the decreasing water vapor mixing ratio must be due to mixing of moist air from the tropopause level with dry stratospheric air. Mixing of dry stratospheric air and temperature increase above the tropopause lead to a decrease in relative humidity in the stratosphere.*
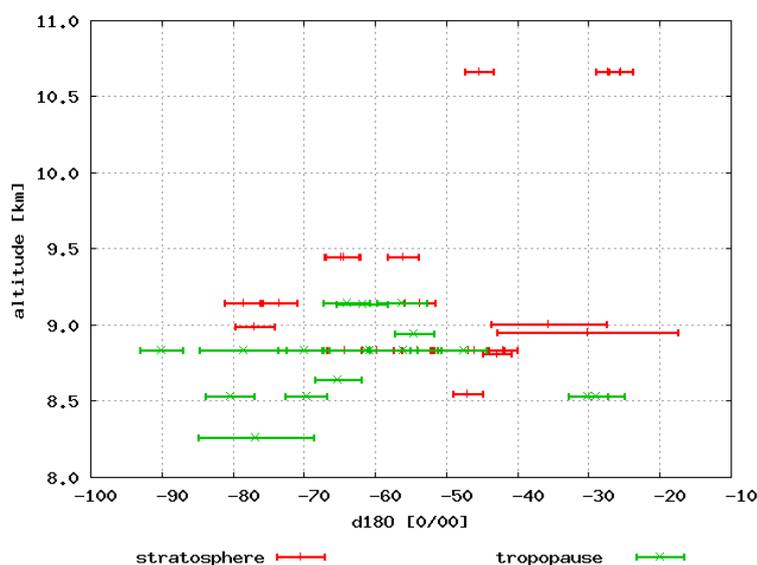
Figure 9.4 : $\delta^{18}O$ plotted versus altitude. Due to the variable tropopause height, no clear trend is visible.

process does not lead to a homogeneous mixing ratio decrease with altitude. But this is easy to understand since the sampling spans a rather wide latitude range, where also the altitude of the tropopause varies. To take this into account, a plot of $\delta^{18}O$ versus the distance to the tropopause is shown in figure 9.5. One might interpret a slight enrichment in the stratospheric dataset with increasing distance to the tropopause. However, the data is taken over a latitudinal range of ≈ 30 degrees, so that an overlap could lead to the scatter if the isotopic composition depends on latitude.

In order to investigate the dependence of $\delta^{18}O$ on both latitude and distance to the tropopause, a three-dimensional plot is shown in figure 9.6. An equally spaced grid with 15×15 gridpoints was created, and $\delta^{18}O$ of each gridpoint was calculated from the datapoints by weighing them according to their distance to the gridpoint, using the standard options of *dgrid3d* of the *gnuplot* software, resulting in the red mesh shown. Not too much trust should be given in the absolute values shown in the plot, as the *dgrid3d* routine smears out the datapoints, which has bigger effect on datapoints with high $\delta^{18}O$ than on those with low $\delta^{18}O$ (see the *gnuplot* manual for more details). Also, the data of August and October are mixed, so that only an average between the seasonal values can be shown. Therefore, the plot can only demonstrate the qualitative behavior of the isotopic composition of water vapor. A contour plot of lines of equal isotopic composition derived from the mesh shows that $\delta^{18}O$ generally increases with
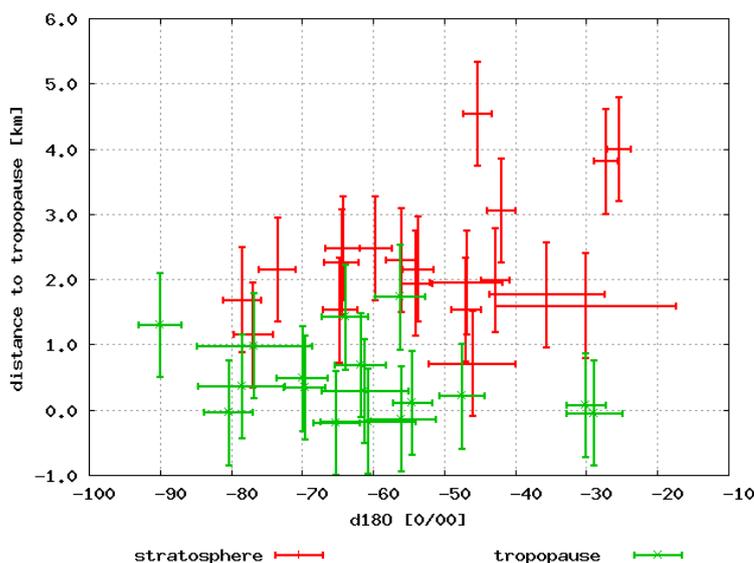
Figure 9.5 : $\delta^{18}O$ *plotted versus distance to the tropopause. A high variability is seen just above the tropopause. The stratospheric samples with higher distance from the tropopause show a slight enrichment in* $\delta^{18}O$, *which could be caused by mixing with air from the stratospheric overworld.*

distance to the tropopause.

Between latitudes of $-50... - 70$ degrees, $\delta^{18}O$ appears to have a minimum. The increase in $\delta^{18}O$ at high southern latitude could be due to increased mixing with stratospheric air, e.g. from the polar vortex. It is not quite clear why $\delta^{18}O$ sharply drops at ≈ -50 degrees south. Of course the data is much too sparse to draw statistically robust conclusions, but an interesting aspect might be that the southern tip of New Zealand is located at -46.5. Due to the high mountain ranges of the South Island, air from lower altitudes might have been lofted in order to flow over the mountains, thus carrying water vapor with higher $\delta^{18}O$-values to higher altitudes.

A similar graph for the water vapor mixing ratio is shown in figure 9.7. Here the relative moist conditions just above tropopause level can be seen, and the water vapor mixing ratio tends to decrease with increasing distance to the tropopause. Also a drier stratosphere at higher latitudes is evident, which could be explained by mixing with dry stratospheric air from the polar vortex.

Figure 9.8 shows a plot of $\delta^{18}O$ versus H_2O mixing ratio. For the tropopause samples with $v > 10ppm$, no correlation between mixing ratio and $\delta^{18}O$ can be found. The isotopic composition of water vapor here is $\delta^{18}O \approx -60‰$, with a
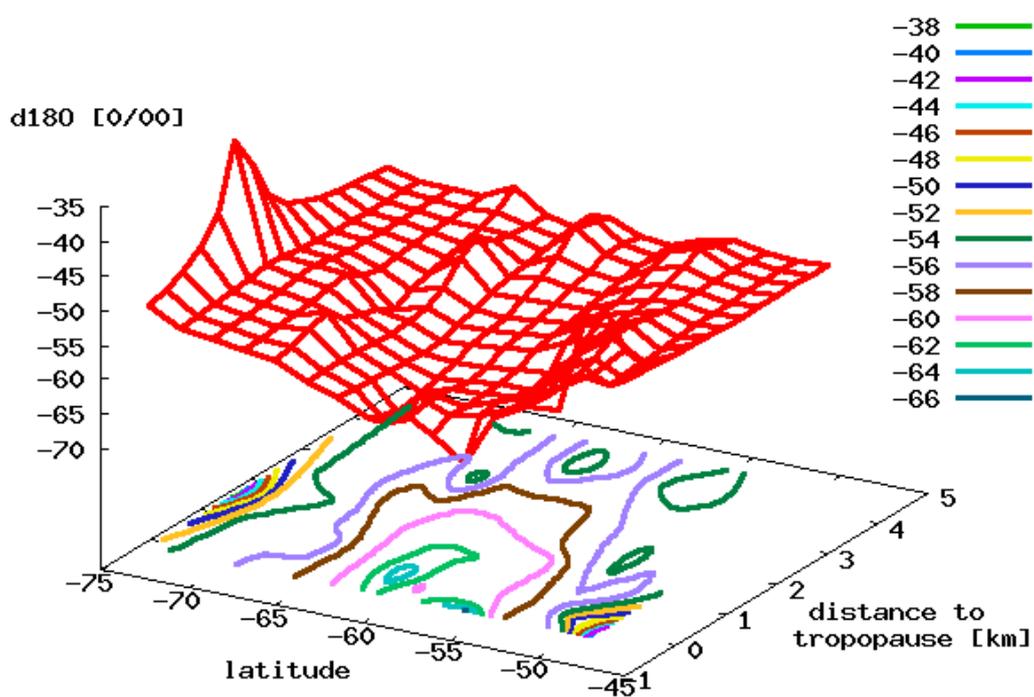
Figure 9.6 : *A three-dimensional plot of $\delta^{18}O$ versus latitude and distance to the tropopause. Shown is an equally spaced grid with 15×15 datapoints. $\delta^{18}O$ is calculated from the data by weighing each datapoint according to its distance to the gridpoint (red mesh). Also shown are contour lines of equal isotopic composition. It appears that $\delta^{18}O$ has a minimum between $-50... -70$ degrees. Generally, $\delta^{18}O$ increases with distance to the tropopause.*
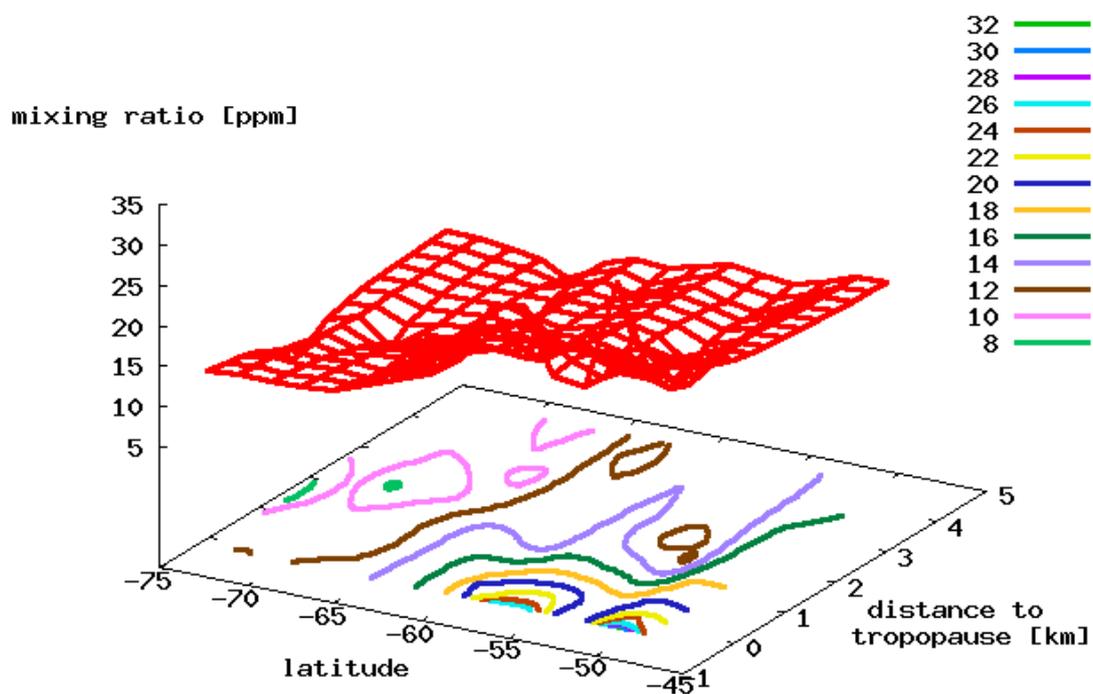
Figure 9.7 : *A three-dimensional plot of υ versus latitude and distance to the tropopause. Generally, the water vapor mixing ratio decreases above the tropopause. At higher latitudes, the stratosphere appears to be dryer due to mixing with the polar vortex.*
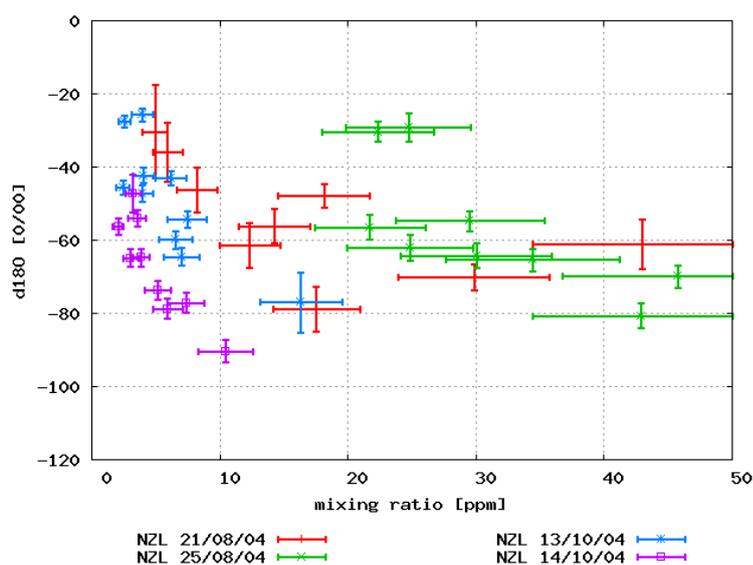
Figure 9.8 : $\delta^{18}O$ *plotted versus mixing ratio. The tropopause samples with $\upsilon >$ $10ppm$ show no tight correlation between mixing ratio and $\delta^{18}O$, whereas the individual stratospheric datasets seem to share a common slope.*

broad data range between $-90... - 30‰$.

However, an interesting effect is seen in the relationship between mixing ratio and isotopic composition for $\upsilon < 10ppm$. Figure 9.9 shows only the stratospheric datapoints. A linear regression line is fit to the data of each individual flight. Though there is an offset between the lines, the slope is remarkably constant with $-4.8‰/ppm$, $-5.0‰/ppm$ and $-5.4‰/ppm$ for the first flight in August and the two flights in October, respectively.

Interestingly, the linear fits for the three flights with stratospheric samples do not intersect at a common point. At minimum stratospheric mixing ratios of $\approx 3ppm$, $\delta^{18}O$ varies between $-60... - 20‰$ for the three different flights. Therefore the behavior observed is not due to mixing of a constant purely stratospheric reservoir with air with variable isotopic water vapor composition from the tropopause. Thus the variability of stratospheric air close to the tropopause needs to be further analyzed.

As has been shown for the mixing ratios, it appears that relative moist air from the tropopause with $\upsilon \approx 10ppm$ mixes with dry stratospheric air. The isotopic composition of water vapor at the tropopause shows a high variability due to meteorology , which is also shown by data from lower latitudes [Webster and Heymsfield, 2003]. Mixing with stratospheric air alone can not explain the iso-
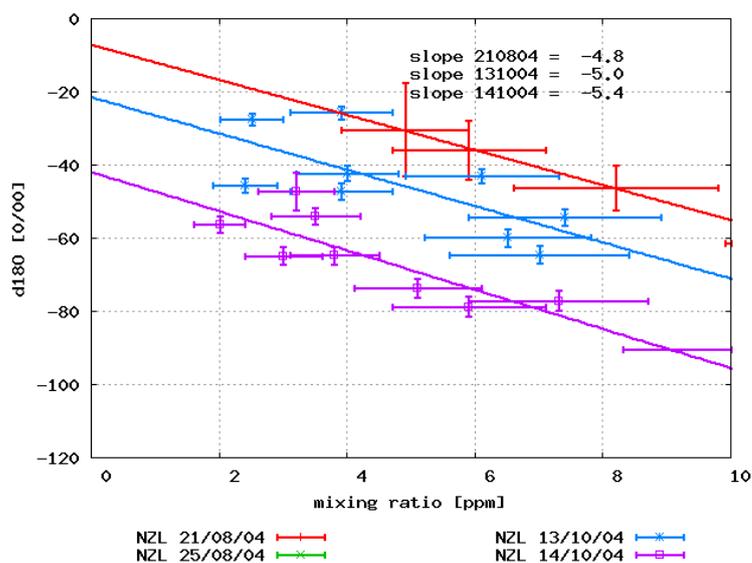
Figure 9.9 : $\delta^{18}O$ *of the stratospheric samples plotted versus mixing ratio. A tight relationship between mixing ratio and isotopic composition is evident; the individual datasets even share the same slope.*

topic behavior of water vapor above the tropopause, since this would require the regression lines in figure 9.9 to intersect at a common point. Another possibility is that the dominant effect could be photochemical alteration of water vapor due to cycling through HO_x.

To investigate this effect, sensitivity studies were performed with the one dimensional model from chapter 4. In the model, an increase in $\delta^{18}O$ with altitude can be seen, which can in principle come from water produced in situ from CH_4 oxidation, or HO_x chemistry. A model run with zero methane was performed, which did not strongly alter the $\delta^{18}O$ profile. This shows that the oxygen isotopic composition is mainly changed by the photochemical cycling. Although the model is not representative for the sampling region, this strongly indicates that this is the effect observed in the samples.

To test the influence of photochemistry at elevated water vapor mixing ratios and variable isotopic input from the tropopause, the mixing ratio at tropopause level in the photochemical model was set to $10ppm$. Three runs were made with $\delta^{18}O$ in the lowermost box $-128‰$ (the same value as in the base model), $-90‰$ and $-60‰$ similar to the stratospheric data. As seen in figure 9.10, $\delta^{18}O$ increases nearly linearly above the tropopause with rates of $5‰/km$, $4‰/km$ and $3‰/km$, respectively.
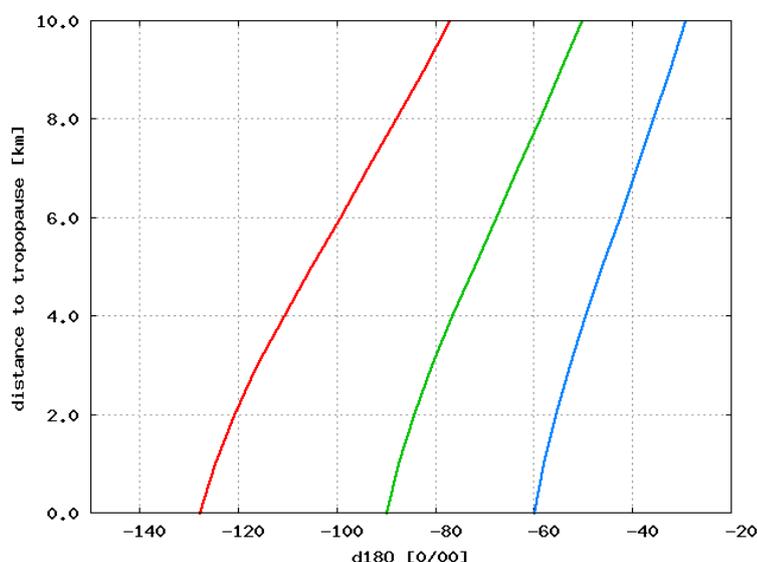
Figure 9.10 : *Modeled $\delta^{18}O$ with increased input of water vapor of $10ppm$ at the tropopause, and variable isotopic composition in the lowermost box. $\delta^{18}O$ increases nearly linearly with rates of $5‰/km$, $4‰/km$ and $3‰/km$, respectively.*

The isotopic composition of the stratospheric samples increases by $\approx 40‰$ between 10 and $3ppm$. Using the $90‰$ and $60‰$ input from the model, this $40‰$ change can be explained by an ascend of $10km$ and $13km$, respectively. This is only two to three times higher than the altitude range sampled of $\approx 4km$ above tropopause level.

Mixing with older stratospheric air is likely to intensify the increase in $\delta^{18}O$ with altitude due to photochemistry. As argued above, the mixing process results in lower water vapor mixing ratios. Simultaneously, this effects the photochemical increase in $\delta^{18}O$ since the water vapor mixing ratio decreases and the influence of freshly produced water vapor from CH_4 oxidation and HO_x therefore becomes stronger. As shown in the model, older stratospheric air is thought to contain $\delta^{18}O$ of $\approx -10‰$, which additionally increases the gradient in $\delta^{18}O$.

A more detailed analysis of the $\delta^{18}O$-data obtained in this thesis requires analysis using the condensation history of the sampled air parcels, e.g. by using computer based trajectories. Such analysis will become available in the near future, as recent results by *A. Gettelman and C. Webster* demonstrate [1]. An ideal model would combine both transport across the tropopause and photochemistry.

As has been discussed in section 7.4.8, the high correlation between $\delta^{17}O$ and

---

[1]poster by NASA, NCAR, CRYSTAL-FACE
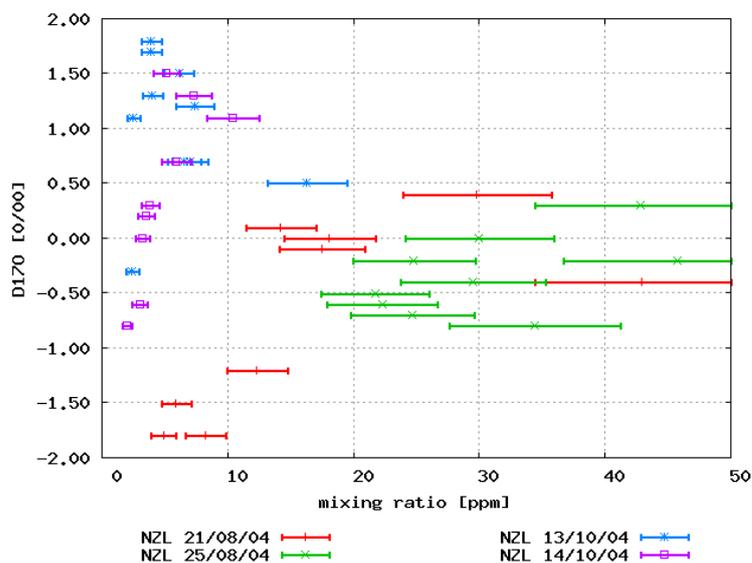
Figure 9.11 : Δ^{17} *plotted versus water vapor mixing ratio. No clear dependence of the anomaly is visible. The error of Δ^{17} is ≈ 0.35 for the larger samples with $v \approx 50 ppm$, and increases with lower mixing ratios. Therefore, a significant deviation from zero is not expected.*

$\delta^{18}O$ allows a very precise analysis of the ^{17}O-anomaly of atmospheric water vapor. In figure 9.11, the anomaly is plotted versus the water vapor mixing ratio.

The analytical precision in Δ^{17} is around $0.35‰$ at $50 ppm$ mixing ratio. However, most of the sample amounts are smaller (see figure 9.2). This results in the higher scatter seen in figure 9.11. The Δ^{17}-data has a mean of $0.13‰$, and standard deviation of $0.95‰$, and a standard error of $0.16‰$. A deviation from zero can therefore not be concluded at a statistically significant level. It is of interest to note that Δ^{17} shows no dependence on either mixing ratio, distance to the tropopause or altitude. Therefore, the limit for stratospheric Δ^{17} from the measurements is that close to the tropopause it must be $\leq 2‰$. This has important consequences.

As seen in figure 4.19, the photochemical model suggests an anomaly of roughly $\Delta^{17} = 1.7‰$ at $4km$ above the tropopause. If oxygen isotope exchange (reactions $HO_2 + O_2$ (R38), $OH + O_2$ (R37)) proceeds with the upper estimated limit, the anomaly slightly decreases to $-0.6‰$. On the other hand, isotopic exchange via the unknown reaction rate of $NO_2 + H_2O$ (R55) drastically increases the anomaly to $\approx 19‰$. If the assumption that the water vapor isotopic composition above the sampling region is comparable to the $4km$ above the

tropopause of the model holds true, this has important implications for these unknown reaction rates.

Reaction R55 can at most be $\approx 1/10$ of its assumed upper limit. So the atmospheric observation can be used to put a new upper limit on this exchange rate. Importantly, this is the critical order of magnitude, since this means that the exchange can not affect the isotopic composition of H_2O in the stratosphere significantly.

On the other hand, the reactions R37 and R38 can proceed even at their estimated upper limit without contradicting the measurements. Thus the atmospheric measurements do not pose additional limits to these rates.

9.1.2   Comparison with other Measurements

Only two datasets of the oxygen isotopic composition of water vapor can be chosen for comparison with the observed values. Webster and Heymsfield [2003] have measured $\delta^{17}O = -6 \pm 30\text{\textperthousand}$, $\delta^{18}O = -179 \pm 72$ in water vapor near the tropical tropopause level. As the tropical tropopause is located much higher than the polar tropopause, smaller depletions are expected at mid and high latitudes. This is true for $\delta^{18}O$ measured in this work, which has a minium of $-90\text{\textperthousand}$. The $\delta^{17}O$ measured here is with $-48\text{\textperthousand}$ significantly lower than the mean observed by Webster and Heymsfield [2003]. However, their measured values would lead to an extreme Δ^{17} anomaly, so that at least their mean $\delta^{17}O$ has to be critically reviewed.

The data of Webster and Heymsfield [2003] indicates an isotope anomaly of $\Delta^{17} = 98\text{\textperthousand}$. This value is higher than any model predicts so far. As the region in which this data was obtained is a zone of convective updraft, the isotopic composition should mainly be controlled by condensation and mixing processes, which are both not believed to generate an anomaly. In the supplementary material to the published paper, Webster and Heymsfield [2003] claim that their 1σ errors are about $100\text{\textperthousand}$ and $83\text{\textperthousand}$ for $\delta^{17}O$, $\delta^{18}O$, respectively. The data published in this work with $|\Delta^{17}| < 2\text{\textperthousand}$ is much more precise than any other data published before. Only with this precision the existence and magnitude of an isotope anomaly can be meaningfully investigated. As has been shown in chapter 7, the error in Δ^{17} for the measurements with the new analytical system is smaller than the quadratic error of the individual $\delta^{17}O$, $\delta^{18}O$ measurements. This is due since the errors imposed upon the measurements by handling of the sample in the analytical system can not lead to mass independently fractionated oxygen. However, measurements with optical methods like the one used by Webster and Heymsfield [2003] calculate the isotope ratio from optical spectra.
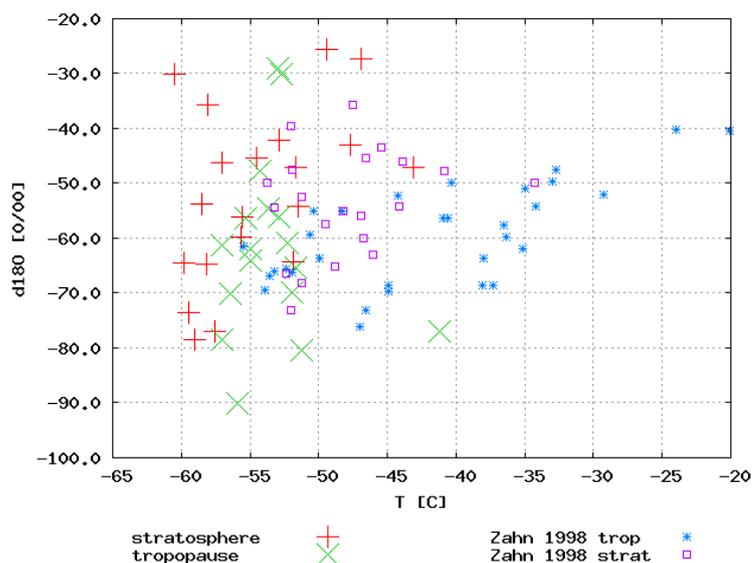
Figure 9.12 : *Comparison of $\delta^{18}O$ with measurements by Zahn et al. [1998]. As the measurements in this work were mostly taken at or above tropopause level, the correlation with temperature is stronger in the tropospheric samples of Zahn et al. [1998] than for this work. Above the tropopause, the data from Zahn et al. [1998] show the same behavior as the data presented here: high variability and a trend towards higher δ-values.*

Hereby different errors may be imposed on the spectra of H_2O, $H_2^{17}O$ and $H_2^{18}O$, which are not necessarily correlated to each other. Therefore, the error of the anomaly measured by Webster and Heymsfield [2003] using the 1σ errors given above is of the order of $110‰$, and the anomaly does not statistically differ from zero.

The second appropriate dataset is the one given by Zahn et al. [1998] from measurements mainly below tropopause height at northern mid to high latitudes. The data is shown in figure 9.12 as plot versus sampling temperature. A depletion with decreasing temperature can be seen in the tropospheric samples down to $-55C$, which follows Rayleigh condensation. Zahn et al. [1998] also found some H_2O samples of stratospheric origin, as identified by the high stratospheric O_3 values which were measured simultaneously. The stratospheric data of Zahn et al. [1998] is enriched in heavy isotopologues versus the tropospheric measurements. This is interpreted as intrusions of stratospheric air by Zahn et al. [1998].

The data presented in this work covers and extends the isotopic range given by Zahn et al. [1998]. The high variability in the isotopic composition of water
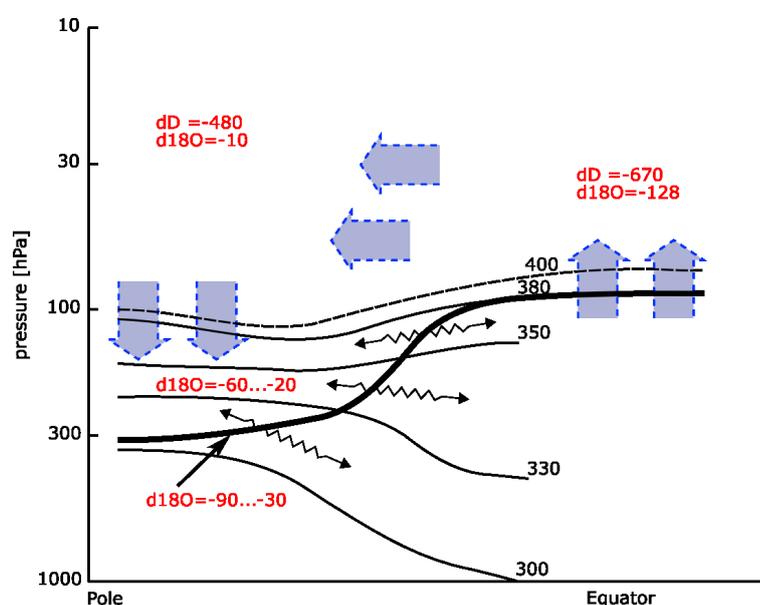
Figure 9.13 : *Schematic view on the isotopic composition of water vapor in the transport picture of Holton et al. [1995]. δ-values are approximations.*

vapor at tropopause height can be explained by temperature dependence. The stratospheric samples show a clear dependence of $\delta^{18}O$ on the mixing ratio, which can not be explained by mixing alone. It is therefore concluded that photochemistry is the dominant factor affecting the oxygen isotopic composition of water vapor above tropopause level.

9.1.3   Water Vapor Isotopes in STE

Figure 9.13 illustrates the present knowledge of the behavior of the stable water isotopologues in the stratosphere. Water vapor mainly enters the stratospheric overworld in convective updrafts in the tropics. Due to the very cold tropopause temperature, the water vapor mixing ratio here is only $\approx 4ppm$, and its isotopic composition is highly depleted in heavy isotopologues. The details of the tropical dehydration processes are currently under investigation, but the measurements of Webster and Heymsfield [2003] indicate that a mixture of gradual and convective dehydration occurs (see section 3.2.1). Due to the absorption of solar irradiation, air parcels ascend diabatically above the tropical tropopause and rise into the stratospheric overworld.

As shown in the one-dimensional model in chapter 4, water isotopologues in

the stratospheric overworld get enriched in both hydrogen and oxygen versus their stratospheric entry values. This is due to methane oxidation and cycling of H_2O through OH_x. Water vapor in the upper stratosphere reaches mixing ratios of $\approx 6ppm$ after $\approx 90\%$ of stratospheric methane is destroyed, whereby $\delta D \approx -480\permil$ and $\delta^{18}O \approx -10\permil$ are encountered.

Due to diabatic cooling at higher latitudes, air descends into the lowermost stratosphere. Here, the isentropes cross the surfaces of potential vorticity, and isentropic exchange with the tropospheric air reservoir is possible. As the tropopause level is located at lower altitudes than in the tropics, air crossing the tropopause is less dehydrated than air from the stratospheric overworld. In the first kilometers above the tropopause, both photochemistry and mixing are important for the isotopic composition of water vapor, which is demonstrated by the data obtained in this work. Water vapor that has mixed down to stratospheric mixing ratios of $3ppm$ has $\delta^{18}O = -60... - 20\permil$, while fresh water vapor from the tropopause varies between $-90... - 30\permil$.

9.2   Tritiated Water Vapor

Figure 9.14 shows the tritium ratios measured in August 2003 versus the distance to the tropopause. The latitudinal range makes the detection of PSC particle sedimentation unlikely, so that the data represent HTO background measurements. Only the southernmost measurements could be affected by PSC particles, which will be discussed later.

The tritium ratio rises from $\approx 1000TU$ at $2km$ below to about $10000TU$ at $3km$ above tropopause height. As mentioned in section 4.6.1, the simple HTO-model underestimates the tritium ratio in the troposphere and the first kilometers into the tropopause layer. Therefore, only the modeled values from $2km$ above tropopause level are shown.

There is a disagreement between the tritium ratios measured and modeled. As has been discussed in the section covering the stable isotopologues, the water vapor mixing ratio drops from about $\approx 50ppm$ at tropopause level to $\approx 6ppm$ in the free stratosphere. Therefore, in the measurement region there is much more water vapor abundant than the assumed $5ppm$ in the model. Thus the measured tritium ratio is accordingly smaller by a factor of ten than predicted by the model.

However, the HTO mixing ratio is not affected by this uncertainty, as it refers to the total number of tritium atoms per mg of air. Thus, the number of H_2O molecules do not effect the HTO mixing ratio.
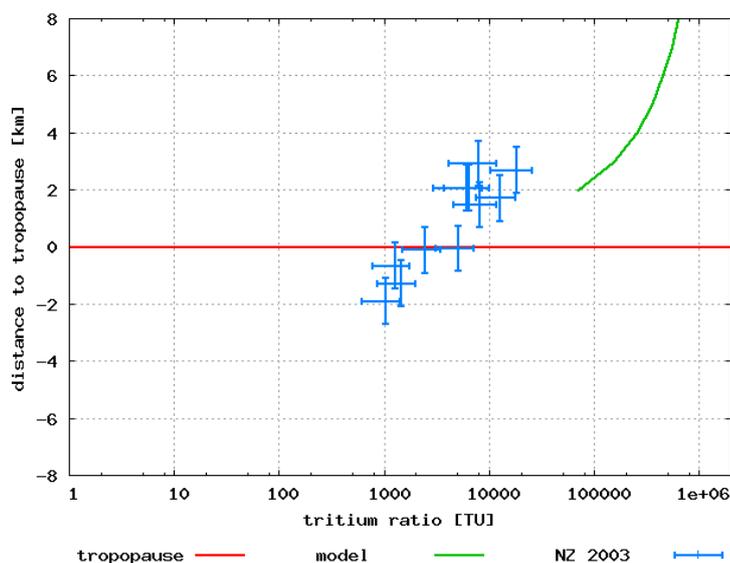
Figure 9.14 : *Tritium ratio plotted versus distance to the tropopause. There is a disagreement between the simple HTO model and the measurements. The model assumes a "dry" stratosphere of $\approx 5ppm$, whereas the actual conditions in the lowermost stratosphere have higher water vapor mixing ratios.*

The HTO mixing ratio versus distance to the tropopause is shown in figure 9.15. Here, the agreement with the simple HTO-model is reasonable at $2km$ above the tropopause upwards. For comparison, the approximations for ς near the tropopause (see section 4.9) of Zahn [1995], Mason [1977], Ehhalt [1971] are shown. The samples agree within errors with the data from Zahn [1995]. At $2km$ above tropopause level, the HTO-mixing ratio is only about $1/20$ of the values given by Mason [1977] and $1/40$ of the levels measured by Ehhalt [1971]. This demonstrates that the tritium level of stratospheric water vapor has indeed returned to an equilibrium with cosmic ray production, as by radioactive decay and stratosphere/troposphere exchange less than $1/100$ of the HTO of 1971 should remain in the stratosphere.

The objective for taking the HTO measurements was to establish a background HTO profile for later detection of traces of sedimented PSC particles, which should increase the HTO mixing ratio above its background profile. It is therefore of interest whether the measured data is already affected by PSC particle sedimentation.

The combined mean value and standard deviation of the measurements presented here is $16 \pm 11\,atoms/mg\,air$, which agrees with the $10 \pm 3\,atoms/mg\,air$ given
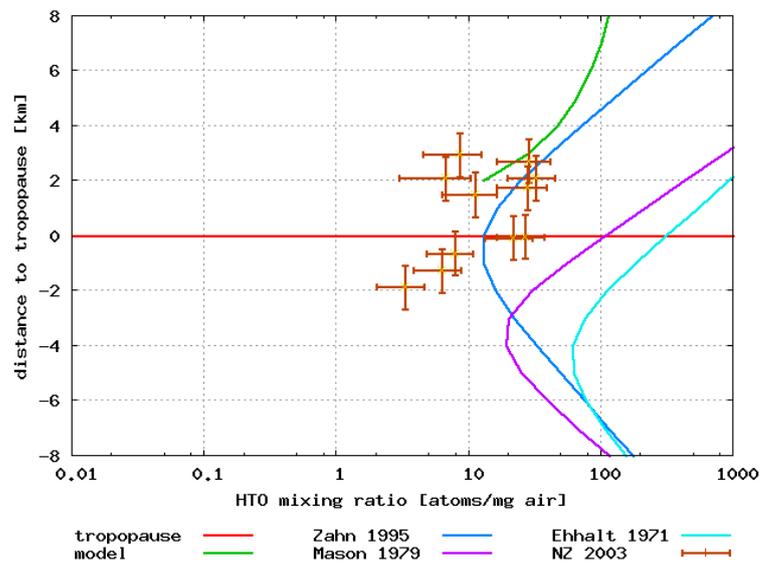
Figure 9.15 : *HTO-mixing ratio plotted versus distance to the tropopause. At present, HTO mixing ratios are much lower than in the 1960s and 70s, when there was atmospheric input due to nuclear bomb testing. The measured HTO mixing ratios agree well with the observations of Zahn [1995]. Also agreement with the simple HTO model described in this thesis is found from 2km above the tropopause upwards.*

by Zahn et al. [1998]. A PSC particle sedimentation can only be proved if the HTO mixing ratio at high latitudes is significantly higher than its background level. All datapoints below the tropopause level are $< 10\,atoms/mg\,air$. The datapoints above tropopause level are either below $10\,atoms/mg\,air$, or do not differ significantly from the modeled background profile. So only the two samples directly at the tropopause level (sample numbers 4 and 6, see appendix A) could be influenced by PSC particle sedimentation. Though they differ somewhat from the $10\,atoms/mg\,air$ assumed background level, this difference has to be rejected on the 2σ level. Also, these samples were taken at latitudes of 58.3 and 64.6 degrees south, so that they present samples from mid latitudes. Based on this, these two samples are also considered to belong to the tritium background profile. Therefore, no sample shows traces of PSC particle sedimentation.

Chapter 10

Summary

The presented project has aimed at the task to quantify the isotopic composition of water vapor in the upper troposphere and lower stratosphere. Both models and measurements have been presented to shine some light into this interesting matter, which is likely to gain scientific interest over the years to follow.

The one-dimensional model for the stable water isotopes in the stratosphere and mesosphere gives insight into the complicated photochemistry of water vapor and the trace gases which have an influence on its isotopic composition. Both hydrogen and oxygen isotopes are covered. Of the hydrogen bearing species, agreement between model and representative CH_4 and H_2O measurements is good. The existing datasets for HDO generally have errors $> 50\text{‰}$, so that the quality of the model can not be confirmed below this level. The model also underestimates the fraction of CH_4 oxidized by $O(^1D)$, though this likely caused by a meridional dependence of the methane oxidation pathways, that can not be resolved in a one dimensional model.

The modeled HD profile differs significantly from the extreme stratospheric enrichment presented by Rahn et al. [2003] and Röckmann et al. [2003]. It is likely that the disagreement in the base model stems from the assumption of statistical removal of deuterium from the methane oxidation chain. Qualitative agreement between model and data can be found if all deuterium is left in the chain before ending up in formaldehyde. Though this is not validated by experimental data so far, such a process is hinted by the fractionation factors in Gierczak et al. [1997].

The agreement between modeled and previously measured $\delta^{17}O$, $\delta^{18}O$ of water vapor is also good, though the measured datasets here also suffer from their huge errors. The Δ^{17} anomaly of water vapor in the middle atmosphere is modeled to have a maximum of 7‰ at $32km$. However, many fractionation factors and rate constants for chemical reactions and isotopic exchange rates have not been

measured so far, so that the model stands somewhat on a theoretical base. Hopefully, more rate coefficients will become available in the near future so that the connection of water vapor to the oxygen isotope reservoirs O_2, O_3, $O(^1D)$ and NO_x can be quantified.

The simple HTO model underestimates the tritium level in the troposphere due to overestimated precipitation. As accurate parameterization for precipitation is difficult to obtain, the model can only be valid from some kilometers above tropopause level.

Several instruments have been developed for the analysis of small samples of atmospheric water vapor. For the analysis of stable oxygen and hydrogen of H_2O, a continuous-flow isotope ratio mass spectrometric unit has been built that can analyze water samples of $120nl$ (liquid) with an accuracy of $0.7‰$, $1.3‰$ and $7‰$ for $\delta^{17}O$, $\delta^{18}O$ and δD, respectively. Unfortunately, the hydrogen isotope analysis did work not well with external sample containers, so that this issue has to be resolved in the future.

External sample containers can be connected to the analytical system, making the analysis of atmospheric water vapor possible. To obtain the desired $120nl$ of sample amount, less than $20l$ of stratospheric air are required. At present, the precision for the external samples is limited by the calibration to about $(0.9‰...1.4‰, 1.7‰...2.4‰)$ for $(\delta^{17}O, \delta^{18}O)$. This is better by roughly an order of magnitude than all other existing methods. Due to the high correlation between $\delta^{17}O$ and $\delta^{18}O$, the error of the Δ^{17} anomaly is only $0.35‰$, which enables the investigation of Δ^{17} of stratospheric water vapor. The source of the error in the calibration is not fully known, but is likely related to the scale contraction seen in the measurements. This contraction could be caused by chemical reactions inside the trap or the adjacent lines in the hot extraction oven. In the future, the source of this contraction should be investigated.

For the measurement of the radioactive tracer HTO, the apparatus developed by Franz [2002] has been improved to increase the number of samples to be taken on a measurement flight. Calibration of the system can be performed to obtain the amount of blank water and release efficiency of the molecular sieve traps. Due to the errors of these two numbers, the error in HTO measurements applying this methods is $\approx 30\%$. Due to these high errors, the application of this method for the measurement of HDO was not attempted.

The measurements of HTO taken on flights from New Zealand to Antarctica in August 2003 confirm the observations of Zahn et al. [1998]. The levels of stratospheric HTO seem to have reached an equilibrium with production from cosmic radiation; no influence of bomb tritium can be seen any longer. Values from $\approx 1000...12000 TU$ have been observed, corresponding to $4...20$ tritium atoms

per milligram of air. The simple HTO model agrees with the observations at $2km$ above the tropopause level, though measurements at both higher and lower altitudes would be desirable to map the HTO profile. No traces of sedimented PSC particles could be detected.

Measurements of water vapor in the same measurement region in August and October 2004 reveal a decrease of water vapor mixing ratio above the tropopause. The precision of the new analytical equipment allows for the first time to actually resolve the variability of $\delta^{18}O$ above the tropopause. Analysis of the data shows a variability in $\delta^{18}O$ at tropopause level within $-90...-30$‰. Above the tropopause, $\delta^{18}O$ of the individual datasets shows a clear increase with decreasing water vapor mixing ratio with a nearly constant slope of 5‰$/ppm$, a behavior which can not be explained by mixing with stratospheric air alone. Results from the model indicate that primarily photochemistry, i.e. the HO_x cycling, causes the oxygen isotope enrichments. To investigate these effects in more detail, at least two dimensional models which include water vapor transport across the tropopause are required.

The Δ^{17} anomaly in the lowermost stratosphere at mid to high latitudes has been shown to be less than ± 2‰, which is the most precise measurement of Δ^{17} so far. This is a very interesting result, since it puts important constraints to the unknown oxygen isotope exchange rates of $HO_2 + O_2$, $OH + O_2$ and $NO_2 + H_2O$. While the first two reactions can take place at their estimated upper limit without contradicting the measurements, the latter reaction could only take place at about $1/10$ of the estimated upper rate used in the model. Thus the Δ^{17} anomaly in stratospheric water vapor must be rather small, since only the exchange with NO_2 was believed to transfer a large anomaly from odd oxygen molecules to H_2O.

Appendix A

Atmospheric Data

The following pages contain navigational and isotopic data for the atmospheric samples discussed in this thesis. All times and dates are given in Z (Greenwich) time.

no	date [Z]	time [Z]	height [m]	longitude [degr]	latitude [degr]	T [C]	tropop. [m]
1	20/08/03	20:22:13	8297	171.5	-49.8	-46.4	8931
4	20/08/03	21:48:42	8839	170.5	-58.3	-50.4	8862
5	20/08/03	22:33:04	9076	170.1	-61.2	-55.5	7326
6	22/08/03	03:33:16	10668	169.4	-64.6	-68.4	10742
7	20/08/03	23:22:17	9899	169.5	-65.7	-66.9	6948
12	21/08/03	02:32:26	10668	167.0	-72.5	-70.1	8568
13	21/08/03	05:19:02	10668	171.1	-51.6	-56.4	9163
14	21/08/03	22:20:48	9449	169.5	-65.5	-59.0	10703
15	22/08/03	02:45:13	10663	167.7	-71.1	-49.8	8555
16	22/08/03	21:20:30	8992	170.4	-59.4	-54.8	10857
17	21/08/03	04:14:23	10668	170.2	-60.0	-56.4	7940

Table A.1 : *Navigational data for the HTO measurements. Tropopause levels are from the NASA Goddard Automailer*

145

no	^3R $[TU]$	$\Delta(^3R)$ $[TU]$	HTO $[1/mg\,air]$	ΔHTO $[1/mg\,air]$	δD $[\permil]$
1	1235	483	7.8	3.0	-175
4	4941	1936	26.8	10.5	-95
5	12353	5090	27.7	11.4	-106
6	2388	938	21.6	8.5	-345
7	7671	3616	8.5	4.0	-192
12	6324	3481	6.6	3.6	-197
13	7878	3410	11.2	4.9	-189
14	1398	552	6.3	2.5	-334
15	5919	2321	32.2	12.6	-488
16	998	396	3.3	1.3	-205
17	17600	7641	28.6	12.4	-124

Table A.2 : *Isotopic data of the HTO measurements. The δD measurements are not further discussed in this work, as their precision is thought to be too low to draw valid conclusions.*

no	date [Z]	time [Z]	height [m]	longitude [degr]	latitude [degr]	T [C]	tropop. [m]
1	21/08/04	19:04:24	8839	171.15	-51.05	-52.3	9000
2	21/08/04	19:24:00	8839	170.86	-53.92	-52.9	8962
3	21/08/04	19:43:43	8839	170.48	-56.62	-54.3	8615
4	21/08/04	20:03:19	8839	170.24	-59.11	-56.4	8346
5	21/08/04	20:22:50	8839	169.90	-61.77	-57.0	8462
6	21/08/04	20:42:21	8839	169.31	-64.49	-57.0	8538
7	21/08/04	21:02:02	8839	168.68	-67.15	-57.0	8115
8	21/08/04	21:21:58	9009	168.07	-69.74	-58.1	7231
9	21/08/04	21:42:09	9343	167.26	-72.28	-61.1	7115
10	21/08/04	22:01:35	8956	166.26	-74.52	-60.5	7346
11	25/08/04	19:05:25	8534	171.24	-49.33	-53.0	8570
12	25/08/04	19:24:52	8534	171.03	-50.95	-52.7	8453
13	25/08/04	19:44:13	8534	170.64	-54.10	-51.9	8181
14	25/08/04	20:03:49	8534	170.44	-56.50	-51.2	8563
15	25/08/04	20:23:27	8646	170.30	-58.46	-51.7	8830
16	25/08/04	20:43:10	8949	170.14	-60.37	-53.7	8828
17	25/08/04	21:02:36	9139	169.83	-62.32	-55.0	8442
18	25/08/04	21:21:50	9144	169.43	-64.33	-55.0	7709
19	25/08/04	21:41:41	9144	169.02	-66.35	-55.3	7400
20	13/10/04	02:22:44	8265	171.36	-50.62	-41.23	7269
21	13/10/04	02:45:45	8549	171.06	-53.32	-43.09	7000
22	13/10/04	03:09:21	8811	170.79	-56.13	-47.67	6808
23	13/10/04	03:34:32	8839	170.41	-59.27	-51.48	6885
24	13/10/04	03:59:24	8839	169.94	-62.42	-51.81	6346
25	13/10/04	04:24:40	8839	169.41	-65.38	-52.86	5769
26	13/10/04	04:52:31	8839	168.70	-68.43	-55.63	6346
27	13/10/04	10:23:15	10668	168.83	-67.66	-54.52	6115
28	13/10/04	11:14:55	10668	170.09	-61.44	-49.42	6654
29	13/10/04	12:02:30	10668	170.83	-55.61	-46.95	6846
30	14/10/04	20:13:10	8839	171.07	-53.26	-51.67	6875
31	14/10/04	21:15:20	8992	170.17	-60.88	-57.52	7828
32	14/10/04	20:44:26	8839	170.67	-57.09	-55.94	7524
33	14/10/04	21:46:19	9144	169.57	-64.55	-59.01	7440
34	14/10/04	22:17:33	9144	168.82	-67.83	-59.42	6975
35	14/10/04	22:47:57	9144	167.90	-71.13	-58.55	6972
36	15/10/04	03:39:46	9449	169.11	-66.28	-59.83	7169
37	15/10/04	04:25:11	9449	170.17	-60.54	-58.16	7905
38	15/10/04	05:10:43	9449	170.92	-54.60	-55.55	7142

Table A.3 : *Navigational data for the $\delta^{17}O$, $\delta^{18}O$ measurements. Tropopause levels are obtained from the NASA Goddard Automailer*

no	υ	$\delta^{17}O$	$\Delta(\delta^{17}O)$	$\delta^{18}O$	$\Delta(\delta^{18}O)$	Δ^{17}
	[ppm]	[‰]	[‰]	[‰]	[‰]	[‰]
1	42.9	-33.0	3.6	-60.9	6.7	-0.4
2	14.2	-30.0	2.6	-56.1	4.7	0.1
3	18.1	-25.4	1.8	-47.7	3.2	0.0
4	29.8	-37.2	2.3	-70.1	3.6	0.4
5	17.5	-42.3	3.4	-78.6	6.1	-0.1
6	12.3	-34.0	3.6	-61.3	6.1	-1.2
7	8.2	-26.4	3.9	-46.2	6.1	-1.8
8	5.9	-20.5	3.9	-35.7	8.1	-1.5
9	2.2	-11.1	45.4	-24.2	77.9	1.7
10	4.9	-17.8	6.1	-30.2	12.7	-1.8
11	24.7	-16.0	2.1	-29.0	3.9	-0.7
12	22.3	-16.7	1.5	-30.2	2.8	-0.6
13	45.7	-37.6	2.7	-69.8	3.0	-0.2
14	42.8	-43.1	2.0	-80.5	3.5	0.3
15	34.4	-35.8	1.9	-65.3	3.2	-0.8
16	29.5	-29.6	1.7	-54.6	2.8	-0.4
17	24.8	-33.3	2.0	-61.9	3.6	-0.2
18	30.0	-34.4	1.8	-64.1	3.3	0.0
19	21.7	-30.6	2.0	-56.3	3.5	-0.5
20	16.3	-40.9	4.3	-76.9	8.1	0.5
21	3.9	-23.5	2.1	-47.1	2.1	1.7
22	6.1	-21.5	1.1	-43.0	2.0	1.5
23	7.4	-27.8	1.3	-54.1	2.2	1.2
24	7.0	-33.8	1.4	-64.4	2.4	0.7
25	4.0	-21.2	1.6	-42.1	2.0	1.3
26	6.5	-31.4	1.6	-59.8	2.3	0.7
27	2.4	-24.5	1.3	-45.4	2.0	-0.3
28	3.9	-11.8	1.6	-25.6	1.7	1.8
29	2.5	-13.5	1.0	-27.4	1.7	1.1
30	3.2	-25.1	2.7	-47.0	5.1	0.0
31	7.3	-40.2	2.1	-77.0	2.7	1.3
32	10.4	-47.7	1.7	-90.2	3.0	1.1
33	5.9	-41.6	1.6	-78.6	2.7	0.7
34	5.1	-38.1	1.4	-73.6	2.6	1.5
35	3.5	-28.6	1.5	-53.8	2.2	0.2
36	3.8	-34.3	1.4	-64.6	2.4	0.3
37	3.0	-35.3	1.3	-64.8	2.4	-0.6
38	2.0	-30.8	1.3	-56.2	2.2	-0.8

Table A.4 : H_2O mixing ratios and isotopic data of the $\delta^{17}O$, $\delta^{18}O$ measurements. Errors are 1σ errors. The error of the mixing ratios is 20%.

Bibliography

M. Abbas, J. Guo, B. Carli, F. Mencaraglia, A. Bonetti, M. Carlotti, and I. Nolt.
Stratospheric O_3, H_2O and HDO distributions from balloon-based far-infrared observations.
J.Geophys.Res., 92(D7):8354–8364, 1987.

S. Anderson, F. Klein, and F. Kaufman.
Kinetics of the isotope exchange reaction of ^{18}O with NO and O_2 at $298K$.
J.Chem.Phys., 83:1648–1656, 1985.

S. Anderson, J. Morton, and K. Mauersberger.
Laboratory Measurements of Ozone Isotopomers by Tunable Diode Laser Absorption Spectroscopy.
Chem.Phys.Let., 156:175–180, 1989.

S. S. Assonov and C. A. M. Brenninkmeijer.
A new method to determine the ^{17}O isotopic abundance in CO_2 using oxygen isotope exchange with a solid oxide.
Rapid Communications in Mass Spectrometry, 15(24):2426–2437, 2001.

P. Baertschi.
Absolute ^{18}O Content of Standard Mean Ocean Water.
Earth and Planetary Science Letters, 31(3):341–344, 1976.

L. Baker, I. Franchi, J. Maynard, I. Writght, and C. Pillinger.
A technique for the determination of $^{18}O/^{16}O$ and $^{17}O/^{16}O$ isotopic ratios in water from small liquid and solid samples.
Analytical Chemistry, 74:1665–1673, 2002.

C. Bechtel.
Die isotopische Zusammensetzung von Wasser und Methan in der mittlerern Atmosphäre.
Universität Heidelberg, 1999.

C. Bechtel and A. Zahn.
  The isotope composition of water vapour: A powerful tool to study transport
  and chemistry of middle atmospheric water vapour.
  Atmos.Chem.Phy.Disc., 3:3991–4036, 2003.

I. S. Begley and C. M. Scrimgeour.
  High-precision $\delta^2 H$ and $\delta^{18} O$ measurement for water and volatile organic com-
  pounds by continuous-flow pyrolysis isotope ratio mass spectrometry.
  Analytical Chemistry, 69(8):1530–1535, 1997.

N. Bhandari, D. Lal, and Rama.
  Stratospheric circulation studies based on natural and artificial radioactive
  tracer elements.
  Tellus, 18:391–406, 1966.

J. Bigeleisen.
  The relative reaction velocities of isotopic molecules.
  J.Chem.Phys., 17(8):675–678, 1949.

J. Bigeleisen and M. G. Mayer.
  Calculation of equilibrium constants for isotopic exchange reactions.
  J.Chem.Phys., 15(5):261–267, 1947.

G. Brasseur and S. Solomon.
  Aeronomy of the middle atmosphere.
  D. Reidel Publishing Company, 1986.

C. A. M. Brenninkmeijer, P. Kraft, and W. Mook.
  Oxygen isotope fractionation between CO_2 and H_2O.
  Isotope Geoscience, 1:181–190, 1983.

A. Brewer.
  Evidence for a world circulation provided by the measurements of helium and
  water vapour distribution in the stratosphere.
  Q.J.R. Meteor.Soc., 75:351–363, 1949.

B. Carli and J. Park.
  Simultaneous measurement of minor stratospheric constituents with emission
  far-infrared spectroscopy.
  J.Geophys.Res., 93(D4):3851–3865, 1988.

E. Chiou, M. McCormick, and W. Chu.
  Global water vapor distribution in the stratosphere and upper troposphere
  derived from 5.5 years of sage ii observations (1986-1991).

J. Geophys. Res., 102(D15):19105–19118, 1997.

A. Dessler.
The effect of deep, tropical convection on the tropical tropopause layer.
J. Geophys. Res., 107(D3):ACH6–1 – ACH6–5, 2002.

A. Dessler and S. Sherwood.
A model of HDO in the tropical tropopause layer.
Atmos.Chem.Phys., 3:2173–2181, 2003.

A. Dessler, E. Weinstock, J. Anderson, and K. Chan.
Mechanisms controlling water vapor in the lower stratosphere: A tale of two stratospheres.
J. Geophys. Res., 100:23167–23172, 1996.

B. Dinelli, B. Carli, and M. Carlotti.
Measurement of Stratospheric Distributions of $H_2^{16}O$, $H_2^{18}O$, $H_2^{17}O$ and $HD^{16}O$ From Far Infrared Spectra.
J.Geophys.Res., 96(D4):7509–7514, 1991.

B. Dinelli, G. Lepri, M. Carlotti, B. Carli, F. Mencaraglia, M. Ridolfi, I. Nolt, and P. Ade.
Measurement of the isotopic ratio distribution of $HD^{16}O$ and $H_2^{16}O$ in the 20-38 km altitude range from far-infrared spectra.
Geophys. Res. Lett., 24:2003–2006, 1997.

E. Dlugokencky, L. Steele, P. Lang, and K. Masarie.
The growth rate and distribution of atmospheric methane.
J. Geophys. Res., 99(D8):17021–17043, 1994.

P. Dransfeld and H. H. Wagner.
Comparative Study of the Reactions of ^{16}OH and ^{18}OH with $H^{16}O_2$.
Z. Naturforsch., 42a:471–476, 1987.

K. Drdla and R. Turco.
Denitrification through psc formation: A 1-d model incorporating temperature oscillations.
Journal of Atmospheric Chemistry, 12:319–366, 1991.

M. K. Dubey, R. Mohrschladt, N. M. Donahue, and J. G. Anderson.
Isotope specific kinetics of hydroxyl radical (OH) with water (H_2O): Testing models of reactivity and atmospheric fractionation.
J. Phys. Chem. A, 101:1494–1500, 1997.

D. Ehhalt and K. Knott.
Kinetische Isotopentrennung bei der Verdampfung von Wasser.
Tellus, 17(3):389–397, 1965.

D. Ehhalt, F. Rohrer, S. Schauffler, and W. Pollock.
Tritiated water vapor in the stratosphere: Vertical profiles and residence times.
J.Geophys.Res., 107(D24):4757, doi:10.1029/2001JD001343, 2002.

D. H. Ehhalt.
Vertical profiles and transport of HTO in the troposphere.
J. Geophys. Res., 76(30):7351–7367, 1971.

K. L. Feinberg, M. S. Johnson, and C. J. Nielsen.
Relative Reaction Rates of $HCHO$, $HCDO$, $DCDO$, $H^{13}CHO$, and $HCH^{18}O$ with OH, Cl, Br, and NO_3 Radicals.
J. Phys. Chem., 108:7393–7398, 2004.

P. M. d. F. Forster and K. Shine.
Assessing the climate impact of trends in stratospheric water vapor.
Geophys.Res.Let., 29(6):10–1 − 10–4, 2002.

P. Franz.
Entwicklung und Test einer Flugzeugapparatur zur Messung der Isotopenverhältnisse von Wasserdampf in der Antarktischen Tropopausenregion.
PhD thesis, Institut für Umweltphysik, Universität Heidelberg, 2002.

P. Franz and T. Röckmann.
A new continous flow isotope ratio mass spectrometry system for the analysis of $\delta^2 H$, $\delta^{17}O$ and $\delta^{18}O$ of small $(120\mu g)$ water samples in atmospheric applications.
Rapid Communications in Mass Spectrometry, 18:1429–1435, 2004.

Y. Q. Gao and R. Marcus.
Strange and unconventional isotope effects in ozone formation.
Science, 293:259–263, 2001.

M. Gehre, R. Hoefling, and G. Strauch.
Sample preperation device for quantitative hydrogen isotope analysis using chromium metal.
Anal. Chem., 68:4414–4417, 1996.

S. Gerst and P. Quay.
Deuterium component of the global molecular hydrogen cycle.
J.Geophys.Res., 106(D5):5021–5031, 2001.

A. Gettelman, D. E. Kinnison, T. J. Dunkerton, and G. P. Brasseur.
Impact of monsoon circulations on the upper troposphere and lower strato-sphere.
J.Geophys.Res., 109:doi:10.1029/2004JD004878, 2004.

T. Gierczak, R. K. Talukdar, S. C. Herndon, G. L. Vagh, and A. Ravishankara.
Rate Coefficients for the Reactions of Hydroxyl Radicals with Methane and Deuterated Methanes.
J. Phys. Chem., 101(3125-3134), 1997.

G. D. Greenblatt and C. J. Howard.
Oxygen Atom Exchange in the Interaction of ^{18}OH with Several Small Molecules.
J.Phys.Chem., 93:1035–1042, 1989.

J. Guo, M. Abbas, and I. Nolt.
Stratospheric $H_2^{18}O$ distribution from far infrared observations.
Geophys.Res.Let., 16(11):1277–1280, 1989.

R. Hagemann, G. Nief, and E. Roth.
Absolute isotopic scale for deuterium analysis of natural waters. Absolute D/H raio for SMOW.
Tellus, 6(712-715), 1970.

Hobbs.
Ice Physics.
Clarendon Press, Oxford, 1974.

J. Holton, P. Haynes, M. McIntyre, A. Douglas, R. Rood, and L. Pfister.
Stratosphere-troposphere exchange.
Rev. Geophys., 33:403–439, 1995.

J. R. Holton and A. Gettelmann.
Horizontal transport and the dehydration of the stratosphere.
Geophys.Res.Let., 28(14):2799–2802, 2001.

D. Hurst, G. Dutton, P. Romashkin, P. Wamsley, F. Moore, J. Elkins, E. Hintsa, E. Weinstock, R. Herman, E. Moyer, D. Scott, R. May, and C. Webster.
Closure of the total hydrogen budget of the northern extratropical lower strato-sphere.
J. Geophys. Res., 104:8191–8200, 1999.

Jaenicke.
Atmosphäerische Spurenstoffe.

VCH Publishers, 1987.

S. Jaffe and F. S. Klein.
Isotopic Exchange Reactions of Atomic Oxygen produced by the Photolysis of NO_2 at $3660 A$.
Far.Soc.Trans., 62:3135–3141, 1966.

G. Jancso and W. A. van Hook.
Condensed phase isotope effects (especially vapor pressure isotope effects).
Chem.Rev.Washington D.C., 74:689–750, 1974.

C. Janssen, J. Guenther, D. Krankowsky, and K. Mauersberger.
Relative formation rates of $^{50}O_3$, and $^{52}O_3$ in $^{16}O - ^{18}O$ mixtures.
J.Chim.Phys., 111:7179–7182, 1999.

E. Jensen and L. Pfister.
Transport and freeze-drying in the tropical tropopause layer.
J.Geophys.Res., 109(D02207), 2004.

D. G. Johnson, K. W. Jucks, W. A. Traub, and K. V. Chance.
Isotopic composition of stratospheric water vapor: Implications for transport.
Journal of Geophysical Research-Atmospheres, 106(D11):12219–12226, 2001a.

D. G. Johnson, K. W. Jucks, W. A. Traub, and K. V. Chance.
Isotopic composition of stratospheric water vapor: Measurements and photo-chemistry.
Journal of Geophysical Research-Atmospheres, 106(D11):12211–12217, 2001b.

J. C. Johnston, T. Röckmann, and C. A. M. Brenninkmeijer.
$CO_2 + O(^1D)$ isotopic exchange: Laboratory and modeling studies.
J. Geophys. Res., 105(D12):15213–15229, 2000.

JPL, editor.
Chemical Kinetics and Photochemical Data for Use in Atmospheric Studies, 2003. JPL, JPL.

J. Kaiser.
Stable isotope investigations of atmospheric nitrous oxide.
PhD thesis, Johannes Gutenberg-Universität Mainz, 2003.

D. W. Keith.

Stratosphere-troposphere exchange: inferences from the isotopic composition of water vapor.
Journal of Geophysical Research, 105(D12):15167–73, 2000.

E. T. Kerstel, R. van Trigt, N. Dam, J. Reuss, and H. Meijer.
Simultaneous determination of the $^2H/^1H$, $^{17}O/^{16}O$, and $^{18}O/^{16}O$ isotope abundance ratios in water by means of laser spectrometry.
Anal. Chem., 71:5297–5303, 1999.

F. Klein.
Catalysis of isotopic exchange in nitric oxide.
J.Chim.Phys., 60(148-153), 1963.

D. Krankowsky, F. Bartecki, G. Klees, K. Mauersberger, K. Schellenbach, and J. Stehr.
Measurement of heavy isotope enrichment in tropospheric ozone.
Geophys.Res.Let., 22(13):1713–1716, 1995.

Z. Kuang, G. Toon, P. Wennberg, and Y. Yung.
Measured HDO/H_2O ratios across the tropical tropopause.
Geophys.Res.Let., 30(7):25–1–25–4, 2003.

D. Lal and B. Peters.
Handbuch der Physik 46/2.
Springer, 1967.

W. Li, B. Ni, D. Jin, and Q. Zhang.
Comparison of the oxygen-17 abundance in three international standard waters.
Huaxue Tongbao, 6:39–40, 1988a.

W. Li, B. Ni, D. Jin, Q. Zhang, and T. Chang.
Measurement of the absolute abundance of oxygen-17 in V-SMOW.
Kexue Tongbao, 33(19):1610–1613, 1988b.

D. R. Lide.
CRC Handbook of Chemistry and Physics.
CRC Press, 1996.

R. Lingenfelter.
Production of Carbon 14 by Cosmic-Ray Neutrons.
Reviews of Geophysics, 1(1):35–55, 1963.

M. Lopez-Valverde, M. Lopez-Puertas, J. Remedios, C. Rodgers, F. Taylor, E. Zipf, and P. Erdman.

Validation of measurements of carbon monoxide from the improved stratospheric and mesospheric sounder.
J.Geophys.Res., 101:9929–9955, 1996.

J. R. Lyons.
Transfer of mass-independent fractionation in ozone to other oxygen-containing radicals in the atmosphere.
Geophys. Res. Lett., 28(17):3231–3234, 2001.

M. Majoube.
Fractionnement en oxygene 18 et en deuterium entre l'eau et sa vapeur.
J.Chim.Phys.Physiochim.Biol., 68:1423–1436, 1968.

M. Majoube.
Fractionnement en ^{18}O entre la glace et la vapeur d'eau.
J.Chim.Phys.Physiochim.Biol., 68:625–636, 1971.

J. Masarik and J. Beer.
Simulation of particle fluxes and cosmogenic nuclide production in the Earth's atmosphere.
J. Geophys. Res., 104(D10):12099–12111, 1999.

A. S. Mason.
Atmospheric HT and HTO estimation of atmospheric hydrogen residence time from interhemipheric tritium gas transport.
J. Geophys. Res., 82:5913–5916, 1977.

A. S. Mason and G. Östlund.
Atmospheric HT and HTO, 3. vertical transport of water in the stratosphere.
J. Geophys. Res., 81(30):5349–5352, 1976.

S. Massie and D. Hunten.
Stratospheric Eddy Diffusion Coefficients From Tracer Data.
J.Geophys.Res., 86(C10):9859–9868, 1981.

K. Mauersberger.
Measurement of heavy ozone in the stratosphere.
Geophys.Res.Let., 8(8):935–937, 1981.

K. Mauersberger, B. Erbacher, D. Krankowsky, J. Günther, and R. Nickel.
Ozone isotope enrichment: Isotopomer-specific rate coefficients.
Science, 283:370–372, 1999.

K. Mauersberger, P. Lämmerzahl, and D. Krankowsky.
Stratospheric ozone isotope enrichment revisited.
Geophys.Res.Let., 28:3155–3158, 2001.

H. Meijer and W. Li.
The use of electrolysis for accurate $\delta^{17}O$ and $\delta^{18}O$ isotope measurements in water.
Isotopes Environ. Health Stud., 34:349–369, 1998.

L. Merlivat.
Molecular diffusivities of $H_2^{16}O$, $HD^{16}O$, and $H_2^{18}O$ in gases.
Chemic.Physics, 69:2864–2871, 1978.

L. Merlivat and G. Nief.
Fractionnement isotopique lors des changements d'etat solide-vapeur et liquide-vapeur de l'eu a des temperatures inferieures a 0°c.
Tellus, 19(1):122–126, 1967.

H. Michelsen, G. Manney, F. Irion, G. Toon, M. Gunson, C. Rinsland, R. Zander, E. Mahieu, M. Newchurch, P. Purcell, E. Remsberg, J. R. III, H. Pumphrey, J. Waters, R. Bevilacqua, K. Kelly, E. Hintsa, E. Weinstock, E. Chiou, W. Chu, M. McCormick, and C. Webster.
ATMOS version 3 water vapor measurements: Comparisons with observations from two ER-2 lyman-a hygrometers, MkIV, HALOE, SAGE II, MAS, and MLS.
Journal of Geophysical Research, 107(D3), 2002.

M. F. Miller.
Isotopic fractionation and the quantification of ^{17}O anomalies in the oxygen three-isotope system: an appraisal and geochemical significance.
Geochimica et Cosmochimica Acta, 66(11):1881–1889, 2002.

P. W. Mote, K. H. Rosenlof, M. E. McIntyre, E. S. Carr, J. C. Gille, J. R. Holton, J. S. Kinnersley, H. C. Pumphrey, J. M. R. III, and J. W. Waters.
An atmospheric tape recorder: The imprint of tropical tropopause temperatures on stratospheric water vapor.
J.Geophys.Res., 101(D2):3989–4006, 1996.

E. Moyer, F. Irion, Y.L.Yung, and M. Gunson.
ATMOS stratospheric deuterated water and implications for troposphere-stratosphere transport.
Geophys. Res. Lett., 23:2385–2388, 1996.

R. E. Newell and S. Gould-Stewart.
  A stratospheric fountain?
  J.Atmos.Sci., 38:2789–2796, 1981.

J. Notholt, D. Weisenstein, B. Luo, S. Fueglistaler, M. Lawrence, R. von
  Kuhlmann, T. Warneke, H. Bingemer, and T. Peter.
  Influence of Tropospheric SO_2 on Particle Formation and Stratospheric Hu-
  midity.
  In *Geophysical Research Abstracts*, volume 6, 2004.

T. Okai and Y. Takashima.
  Tritium Concentrations in Atmospheric Water Vapor, Hydrogen and Hydro-
  carbons in Fukuoka.
  Appl. Radiat. Isot., 42(4):389–393, 1991.

S. Oltmans, H. Vömel, D. Hofmann, K. Rosenlof, and D. Kley.
  The increase in stratospheric water vapor from balloonborne, frostpoint hy-
  grometer measurements at washington, d.c., and boulder, colorado.
  Geophysical Research Letters, 27(21):3453–3456, 2000.

W. Pollock, L. E. Heidt, R. Lueb, and D. H. Ehhalt.
  Measurement of stratospheric water vapor by cryogenic collection.
  J. Geophys. Res., 85:5555–5568, 1980.

P. Quay, J. Stutsman, D. Wilbur, A. Snover, E. Dlugokencky, and T. Brown.
  The isotopic composition of atmospheric methane.
  Global Biochemical Cycles, 13(2):445–461, 1999.

T. Rahn, J. M. Eiler, K. A. Boering, P. O. Wennberg, M. C. McCarthy, S. Tyler,
  S. Schauffler, S. Donnelly, and E. Atlas.
  Extreme deuterium enrichment in stratospheric hydrogen and the global at-
  mospheric budget of H_2.
  Nature, 424:918–921, 2003.

T. S. Rhee, J. Mak, T. Roeckmann, and C. A. Brenninkmeijer.
  Continuous-flow isotope analysis of the deuterium/hydrogen ratio in atmo-
  spheric hydrogen.
  Rapid Communications in Mass Spectrometry, 18:299–306, 2004.

A. Rice, S. Tyler, M. McCarthy, K. Boering, and E. Atlas.
  Carbon and hydrogen isotopic compositions of stratospheric methane: 1. High-
  precision observations from the NASA ER-2 aircraft.
  J. Geophys. Res., 108(D15):4460, doi:10.1029/2002JD003042, 2003.

M. Ridal.
Numerical Simulations of the Isotopic Composition of Stratospheric Water Vapour and Methane.
PhD thesis, Stockholm University, 2001.

M. Ridal and D. E. Siskind.
A two-dimensional simulation of the isotopic composition of water vapor and methane in the upper atmosphere.
J.Geophys.Res., 103(D24):ACH24–1–8, 2002.

C. Rinsland, M. Gunson, J. Foster, R. Toth, C. Farmer, and R. Zander.
Stratospheric profiles of heavy water vapor isotopes and $CH3D$ from analysis of the ATMOS spacelab 3 infrared solar spectra.
J. Geophys. Res., 96:1057–1068, 1991.

T. Röckmann.
Measurement and Interpretation of ^{13}C, ^{14}C, ^{17}O and ^{18}O Variations in Atmospheric Carbon Monoxide.
PhD thesis, University of Heidelberg, Germany, 1998.

T. Röckmann, J. Kaiser, J. N. Crowley, C. A. Brenninkmeijer, and P. J. Crutzen.
The origin of the anomalous or "mass-independent" oxygen isotope fractionation in tropospheric N_2O.
Geophys.Res.Let., 28(3):503–506, 2001.

T. Röckmann, T. Rhee, and A. Engel.
Heavy hydrogen in the stratosphere.
Atmos.Chem.Phys.Disc., 3:3745–3768, 2003.

W. Roedel.
Physik unserer Umwelt: Die Atmosphäre.
Springer-Verlag, 2000.

K. Rosenlof, S. Oltmans, D. Kley, J. R. III, E. Chiou, W. Chu, D. Johnson, K. Kelly, H. Michelsen, G. Nedoluha, E. Remsberg, G. Toon, and M. McCormick.
Stratospheric water vapor increases over the past half-century.
Geophys. Res. Lett., 28(7):1195–1198, 2001.

K. Rozanski, R. Gonfiantini, and L. Araguas-Araguas.
Tritium in the Global Atmosphere: Distribution Patterns and Recent Trends.
J.Phys.G: Nucl. Part. Phys., 17:S523–S536, 1991.

G. Saueressig, P. Bergamaschi, J. Crowley, H. Fischer, and G. Harris.
D/H kinetic isotope effect in the reaction $CH_4 + Cl$.
Geophys.Res.Let., 23(24):3619–3622, 1996.

G. Saueressig, J. N. Crowley, P. Bergamaschi, C. Brühl, C. A. Brenninkmeijer, and H. Fischer.
Carbon 13 and D kinetic isotope effects in the reactions of CH_4 with $O(^1D)$ and OH: New laboratory measurements and their implications for the isotopic composition of stratospheric methane.
J.Geophys.Res., 106(D19):23127–23138, 2001.

B. Schueler, J. Morton, and K. Mauersberger.
Measurement of isotopic abundances in collected stratospheric ozone samples.
Geophys.Res.Let., 17(9):1295–1298, 1990.

J. H. Seinfeld and S. N. Pandis.
Atmospheric Chemistry and Physics.
Wiley-Interscience, 1998.

M. Shapiro.
Turbulent Mixing within Tropopause Folds as a Mechanism for the Exchange of Chemical Constituents between the Stratosphere and Troposphere.
J.Atmos.Sci., 37:994–1004, 1980.

S. C. Sherwood and A. E. Dessler.
On the control of stratospheric humidity.
Geophys.Res.Let., 27(16):2513–2516, 2000.

S. C. Sherwood and A. E. Dessler.
A model for transport across the tropical tropopause.
J. Atmos. Sciences, 58:765–779, 2001.

A. Sinha, E. R. Lovejoy, and C. J. Howard.
Kinetic study of the reaction of HO_2 with ozone.
J. Chem. Phys., 87:2122–2128, 1987.

E. Soyez.
Entwicklung einer neuen Sammelmethode von atmosphärischem Wasserdampf für Isotopenmessungen.
PhD thesis, Universität Heidelberg, 1999.

A. Stenke and V. Grewe.
Simulation of stratospheric wate vapor trends: impact on stratospheric ozone chemistry.

Atmos.Chem.Phys.Discuss., 4:6559–6602, 2004.

M. Stowasser, H. Oelhaf, G. Wetzel, F. Friedl-Vallon, G. Maucher, M. Seefeldner, O. Trieschmann, T. Clarmann, and H. Fischer.
Simultaneous measurements of HDO, H_2O, and CH_4 with MIPAS-B: Hydrogen budget and indication of dehydration inside the polar vortex.
J.Geophys.Res., 104(d16):19213–19225, 1999.

M. Thiemens and J. Heidenreich.
The mass-independent fractionation of oxygen - a novel isotope effect and its cosmological implications.
Science, 219:1073–1075, 1983.

O. B. Toon and R. P. Turco.
Polare stratosphärenwolken und ozonloch.
Spektrum der Wissenschaft, pages 42–49, 1991.

H. Urey.
The thermodynamic properties of isotopic substances.
J.Chem.Soc., pages 562–581, 1947.

W. van Hook.
Vapor pressures of the isotopic waters and ices.
J. Phys. Chem., 72:1234–1244, 1968.

C. R. Webster and A. J. Heymsfield.
Water isotope ratios D/H, $^{18}O/^{16}O$, $^{17}O/^{16}O$ in and out of clouds map dehydration pathways.
Science, 302:1742–1745, 2003.

WMO.
SPARC assessment of upper tropospheric and stratospheric water vapour.
Technical report, World Meteorological Organisation, 2000.

E. D. Young, A. Galy, and H. Nagahara.
Kinetic and equilibrium mass-dependent isotope fractionation laws in nature and their geochemical and cosmochemical significance.
Geochimica et Cosmochimica Acta, 66(6):1095–1104, 2002.

Y. L. Yung, W. DeMore, and J. P. Pinto.
Isotopic exchange between carbon dioxide and ozone via $O(^1D)$ in the stratosphere.
Geophys.Res.Let., 18(1):13–16, 1991.

A. Zahn.
  Der Tracertransport in der Tropopausenregion.
  PhD thesis, Universität Heidelberg, 1995.

A. Zahn, V. Barth, K. Pfeilsticker, and U. Platt.
  Deuterium, oxygen-18, and tritium as tracers for water vapour transport in the
  lower stratosphere and tropopause region.
  J. Atmos. Chem., 30:25–47, 1998.

M. Zoeger, A. Engel, D. McKenna, C. Schiller, U. Schmidt, and T. Woyke.
  Balloonborne in situ measurements of stratospheric H_2O, CH_4 and H_2 in
  midlatitudes.
  J.Geophys.Res., 104:1817–1825, 1999.

Acknowledgements

Nicole, Tina, Kai, Axel, Gerd, Maren, Stefan, Jutta, and all others that are now furious about not being mentioned - I hope we will spend many an hour in the future together!

Last but not least, I wish to thank the persons dearest to my heart: My parents, Erika and Hans-Werner, my sister Anna and my brother Klaus-Dieter - my family has always been there for me during my studies, and there is no way I could ever repay this huge debt! And this to Sonia, the Spanish rose who has stolen my heart:

Of all the money ere I had, I spent it in good company,
and all the harm I've ever done, alas was done to none but me!
And all I've done for want of wit, to memory now I can't recall,
so fill to me the parting glass, goodnight and joy be with you all!

Of all the comrades ere I had, they're sorry for my going away,
and all the sweethearts ere I had , they wish me one more day to stay!
But since it falls unto my lot that I should go and you should not,
I'll gently rise and softly call, goodnight and joy be with you all!

If I had money enough to spend and leisure time to sit awhile,
there is a fair maid in this town who sorely has my heart beguiled!
Her rosy cheeks and ruby lips, I alone she has my heart in thrall,
so fill to me the parting glass, goodnight and joy be with you all!